

JPRS-CST-90-026

31 OCTOBER 1990



**FOREIGN
BROADCAST
INFORMATION
SERVICE**

JPRS Report

Science & Technology

China

FY-1 METEOROLOGICAL SATELLITE

19980506 054

DISTRIBUTION STATEMENT A

Approved for public release;
Distribution Unlimited

REPRODUCED BY
U.S. DEPARTMENT OF COMMERCE
NATIONAL TECHNICAL INFORMATION SERVICE
SPRINGFIELD, VA. 22161

DTIC QUALITY INSPECTED 3

JPRS-CST-90-026
31 OCTOBER 1990

SCIENCE & TECHNOLOGY

CHINA

FY-1 METEOROLOGICAL SATELLITE

90FE0171 Shanghai HONGWAI YANJIU [CHINESE JOURNAL OF INFRARED RESEARCH] in
Chinese Vol 9 No 2, Apr 90

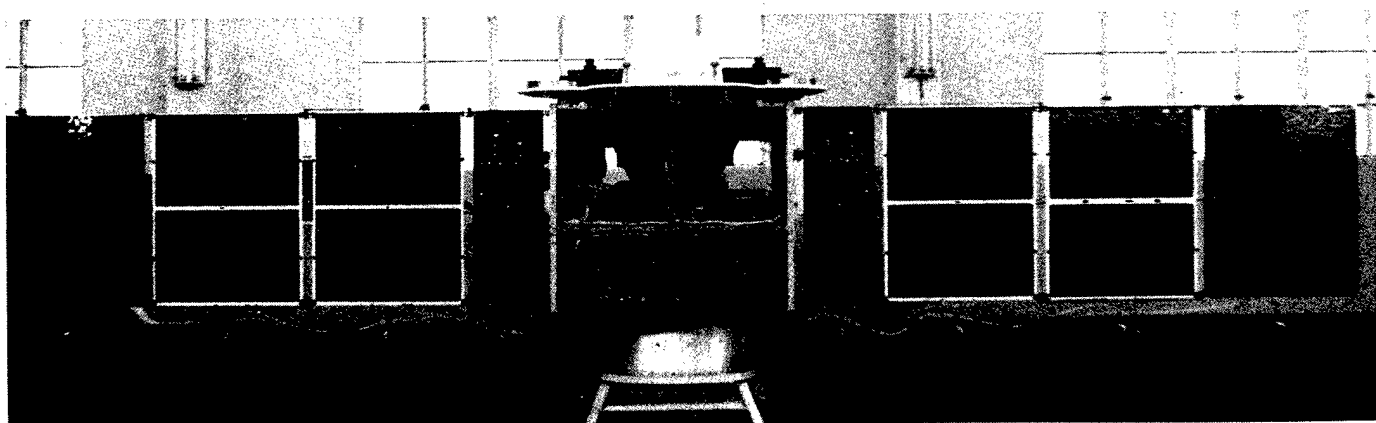
CONTENTS

Photo of FY-1 Meteorological Satellite.....	1
Onboard Ocean-Color Remote Sensing Experiment [Lin Shouren].....	2
Technical Development of Visible-Infrared Scanning Radiometer [Gong Huixing].....	10
Optical Coatings [Xu Buyun, Zhu Cuiyuan, et al.].....	22
Onboard Preprocessing of Remote-Sensor Signal [Weng Chuijun, Li Zhengchang, et al.].....	30
Optical Design of Very-High-Resolution Scanning Radiometer [Zheng Qinbo, Xu Xuerong].....	41
Satellite-Borne High-Accuracy Scanner [Zhang Baolong, Guo Huilin].....	52
Three-Element Linear Silicon Detector [Liang Pingzhi, Zhang Zhongtang, et al.].....	62
Onboard Long-Wave HgCdTe Detector [Fang Jiaxiong, Xu Guosen, et al.].....	71
Applications in Meteorological, Agricultural Remote Sensing [Fang Zongyi, Jiang Jixi].....	79

Photo of FY-1 Meteorological Satellite

90FE0171 Beijing LIAOWANG [OUTLOOK WEEKLY, Overseas Edition] in Chinese No 17,
23 Apr 90 p 20a

[Text] FY-1 experimental meteorological satellite with solar panels extended.



Onboard Ocean-Color Remote Sensing Experiment

90FE0171A Shanghai HONGWAI YANJIU [CHINESE JOURNAL OF INFRARED RESEARCH] in Chinese Vol 9 No 2, Apr 90 pp 162-167 (Ms received 20 Jul 89)

[Article by Lin Shouren [2651 1108 0088] of the Second Institute of Oceanography, State Oceanic Administration, Hangzhou, Zhejiang, 310012, China: "Ocean-Color Remote Sensing Experiment on FY-1 Meteorological Satellite"]

[Text] Abstract

This paper introduces the band selection and data processing method of the two experimental channels used for ocean-color remote sensing, as well as preliminary results in applying the first flight data gathered by the Fengyun-1 (FY-1) meteorological satellite to the survey of ocean color along the coast of China, the boundary between coastal-zone sea water and continental shelf sea water, and the uprising water in the Bohai Wan [Bohai Bay].

Key words: Ocean color, remote sensing, meteorological satellite.

1. Introduction

Ocean color plays an important role in oceanic research, especially in ocean dynamics, marine ecology, and interaction between atmosphere and ocean. Many countries are rushing to develop second-generation ocean-color remote sensing devices, including the OCI (Ocean Color Imager) and SEAWIFS (Sea Observation Wide-Field Remote Sensor) which are scheduled to be deployed on the NOAA and EOSAT satellites in the 1990's, respectively, for global monitoring of ocean color.

In October 1978, the United States launched the Raincloud-7 satellite and for the first time a dedicated sensor, CZCS (coastal zone ocean scanner), was used to perform remote sensing of ocean color. Experimental results indicated that it is capable of detecting surface chlorophyll content, surface suspended sediment content and the diffusive scattering attenuation coefficient of light in seawater.

In addition to monitoring the weather around the globe, the FY-1 meteorological satellite is equipped with ocean-color remote sensing bands to obtain HFPT

(high-resolution picture transmission) images along the coast of China. In this paper, these pictures are used to analyze and study the ocean color.

2. Principle of Ocean Color Remote Sensing

The intrinsic relation between the surface radiance L_w and the physical, biological, and chemical parameters in seawater X_i , i.e.,

$$L_w = F(X_i) \quad (1)$$

is the basis for remote sensing of ocean color. Ocean-color remote sensing involves the measurement of total radiance from space and the derivation of certain factors in the water. Figure 1 shows the optical process involved in remote sensing of ocean color. The radiance measured by the onboard sensor in orbit L_s is the sum of the radiance from sea surface L_w , reflection of sunlight from the ocean surface L_g and reflection of sunlight from gas molecules and aerosol particles in the atmosphere L_p , i.e.,

$$L_s = (L_w + L_g)T_a + L_p \quad (2)$$

where T_a is the transmittance of the atmosphere. In addition to ocean surface radiance L_2 which is dependent upon physical, biological, and chemical parameters in the water, the two remaining components in the radiant energy detected by the remote sensor are interference factors. Thus, in order to determine L_w and to quantitatively derive factors associated with seawater, it is necessary to determine or eliminate these interference factors.

The primary scope of ocean-color remote sensing includes the calculation of the radiance of the body of water beneath the surface L_{ss} from the total radiance L_s measured on the satellite by remote sensing in order to determine parameters X_i that affect the ocean color based on empirical or semi-empirical equations.

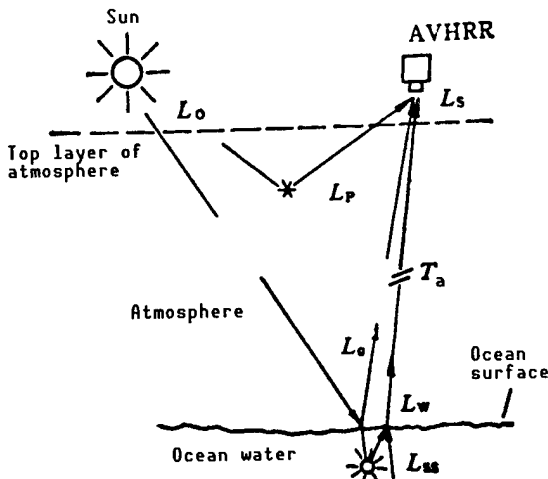


Figure 1. Schematic Diagram of Optical Process in Ocean-Color Remote Sensing

3. Layout of Experimental Ocean-Color Sensing Bands on Board FY-1 Meteorological Satellite

3.1 Analysis of the Three VHRSR Channels

The main mission of the FY-1 meteorological satellite is to gather the weather pictures around the world and to measure cloud top temperatures. Three of the VHRSR [very-high-resolution scanning radiometer] channels, 058, 068, and $0.725-1.1 \mu\text{m}$, can measure cloud distribution patterns and land-ocean boundaries. Another band, $10.5-12.5 \mu\text{m}$, is used to plot a global surface temperature profile. The band layout of FY-1 is similar to that for the AVHRR [advanced very-high-resolution radiometer] on board the TIROS-N satellite. It can meet the needs in gathering all the weather patterns around the world for forecasting the weather in China. In addition, some data is also used to study the turbidity of water along the coast, as well as in other ocean-related applications. However, these are not wavelengths specifically for ocean color sensing because the color of seawater is greenish blue.

3.2 Selection of Two Wave Bands for Ocean Observation

Figure 2 shows a series of spectral radiance curves corresponding to different levels of chlorophyll content α . Curves 1-4 correspond to surface chlorophyll contents of 0.029, 0.240, 0.628, and 0.960 (mg/m^3), respectively. Curves 1, 2, and 3 are characteristic of clean water in open ocean, while curve 4 is typical of turbid coastal water. From Figure 2, we can see that surface radiance is not significantly affected by chlorophyll content at near $0.52 \mu\text{m}$, where the curves show an inflection point. Figure 3 shows another series of absorption-coefficient curves at different phytoplankton concentrations measured in the laboratory. There is significant chlorophyll absorption near $0.44 \mu\text{m}$; however, there is strong reflection at $0.55 \mu\text{m}$. Therefore, CZCS, the first-generation ocean color sensor developed by the United States, chose three bands centered at 0.443 , 0.52 , and $0.55 \mu\text{m}$. As a result of numerous studies conducted by scientists in open oceans and coastal waters around the world, the ratio of the 0.443 to $0.55 \mu\text{m}$ channel, after calibrating for the atmosphere, can effectively estimate the chlorophyll α content in open ocean and a combination of the 0.52 and $0.55 \mu\text{m}$ channels can more effectively determine the chlorophyll content along the coast.

After taking into account these factors and the fact that the primary purpose of the ocean color experiment of FY-1 is to measure the chlorophyll content and turbidity along the coast, we selected $0.48-0.53 \mu\text{m}$ and $0.53-0.58 \mu\text{m}$ as the two experimental channels.

4. Treatment and Applications of Ocean Color Images From the FY-1 Satellite

The quantitative treatment of the FY-1 ocean color patterns is to determine the surface suspension content and chlorophyll level α from the total radiance L_s measured by the VHRSR. From equation (2), it is necessary to carefully handle surface reflective radiance L_g and atmospheric scanning radiance L_p .

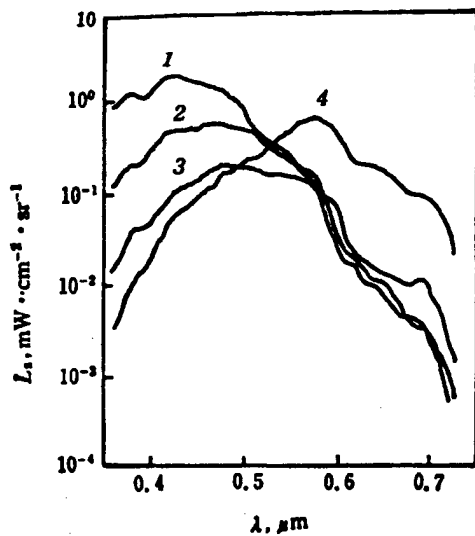


Figure 2. Sea Surface Spectral Radiance Curves at Different Chlorophyll Levels N_c
 1: 0.029 mg/m^3 ; 2: 0.240 mg/m^3
 3: 0.628 mg/m^3 ; 4: 8.900 mg/m^3

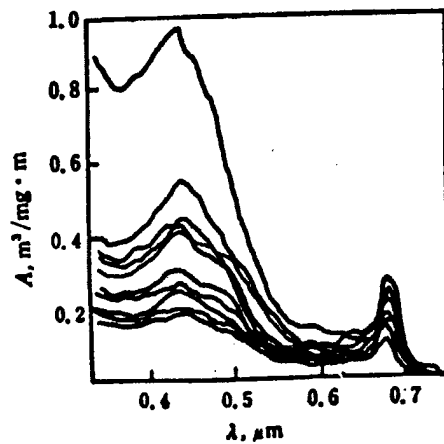


Figure 3. Spectral Specific Absorption Coefficients for Different Phytoplankton Concentrations

4.1 Radiance Due to Surface Reflection L_g

Half of the pictures taken by a wide-angle scanning radiometer, such as the VHRSR, have no reflected sunlight. For this half of the picture, L_g is zero.

4.2 Radiance Due to Atmospheric Scattering L_p

Atmospheric scattering radiance L_p consists of L_R , scattering from gas molecules, and L_A , scattering from aerosol particles. Molecular scattering L_R can be precisely calculated based on Rayleigh molecular scattering theory. Scattering from aerosol particles, however, is more complicated and difficult to process because the aerosol particle concentration in the atmosphere varies with season and location. This is especially true over land and along the coast. To this end, a "clean water subtraction technique" is used most of the time to treat the AVHRR data. It is believed that the upward radiance of "clean water" is negligibly small. Thus, the total radiance detected by the remote sensor is purely caused by atmospheric scattering, i.e.,

$$L_s = L_p^{[c]} = L_R^{[c]} + L_A^{[c]}; \quad (3)$$

Hence, it is easy to calculate total atmospheric scattering over a "clean water" area, $L_p^{[c]}$, and then calculate the Raleigh scattering radiance due to gas molecules $L_R^{[c]}$, and finally derive the amount due to scattering of aerosol particles, $L_A^{[c]}$. The "clean water subtraction technique" treats aerosol scattering as a uniform phenomenon at the instant the image is taken. However,

because the scanner works over a fixed imaging angle, the optical path in the atmosphere increases with the angle of vision. Therefore, atmospheric scattering varies with the viewing angle as well. Hence, it is necessary to calibrate it with respect to the origin of the picture. The correction equation is

$$L_A(i) = L_A^{[c]} \cdot \sec\theta_v(i) / \sec\theta_v(ic); \quad (4)$$

where $\theta_v(i)$ is the nadir angle of the origin of the picture and $\theta_v(ic)$ is the nadir angle at the picture origin where the clean water is.

4.3 Estimation of Ocean Parameters

The total upward radiance from beneath the ocean L_{ss} and the total upward radiance from the surface of the ocean L_w have the following relationship:

$$L_w = \frac{1-\rho}{n^2} L_{ss}; \quad (5)$$

where n is the index of refraction of seawater and ρ is the Fresnel's reflectivity at the seawater interface, which varies slightly with wavelength. Because the upward radiance from beneath the ocean is affected by suspended particles and plankton and dissolved inorganics in a complicated manner, it cannot be accurately calculated theoretically. Therefore, an empirical or semi-empirical equation is frequently used in ocean-color remote sensing.

When estimating the suspended mass at a river mouth or in coastal water with the AVHRR data from the NOAA meteorological satellite, a logarithmic algorithm is often used. When analyzing the VHRSR data obtained in flight over the East China Sea in May 1986, this logarithmic algorithm was also found to apply in the 0.58~0.68 μm channel. In this channel, the relation between surface reflectivity R and suspended sand N_s is

$$R = A_0 + A_1 \log (N_s); \quad (6)$$

where A_0 and A_1 are indexes obtained by the least-square method.

The data obtained from the two channels was treated by the (Lambert) ratio process. It was also satisfactorily used to estimate chlorophyll concentration α . Figure 4 shows some data gathered east of Xiangshan Harbor in Zhejiang. The ratio of the two channels is $R_4/R_3 = L_w(0.53\sim0.58)/L_w(0.48\sim0.53)$. It has a good linear relationship with the chlorophyll α concentration N_c , which is

$$R_{4,3} = B_0 + B_1 N_c; \quad (7)$$

where B_0 and B_1 are proportionality constants obtained experimentally.

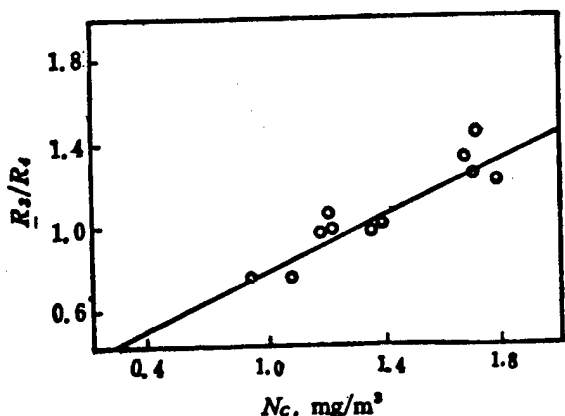


Figure 4. Blue/Green Ratio (R_3/R_4) Vs. the Surface Chlorophyll Concentration (N_c) Measured East of Xiangshan Harbor in Zhejiang

4.4 Investigation of Coastal Turbidity and Uprising Current

Right after FY-1 was launched into orbit, even during the test period, high-resolution "ocean color" pictures along the coast of China were obtained. A picture of the mouth of the Changjiang [i.e., the Yangtze] in the East China Sea taken on 20 September is shown in Figure k of the color inserts [see special color section later in this special issue]. It clearly shows fine details of the mixing and turbulence between coastal water and continental shelf water. The turbidity distribution after image processing is shown in Figure 5. Outside the dotted lines are cloud covered areas. This region is located approximately near 124°E. Based on density distribution, the concentration of suspended matter is higher near the coast and gradually decreases outward. The water boundary is essentially parallel to the coast. A picture of the "ocean color" of the Bohai Wan taken on 21 September is shown in Figure 1 of the color inserts [see color section below]. Figure 6 shows the turbidity distribution in the Bohai Wan plotted according to the data contained in the picture. From these data we can see that there are two uprising currents south of the mouth of the Liao He [Liao River]. This uprising current moves from the bottom to the surface and usually contains a great deal of nutrients to accelerate the breeding of marine animals to create a large fishing ground. Furthermore, the origin of an uprising current is an important subject in modern ocean dynamics. Therefore, the data gathered by the FY-1 satellite would provide valuable information on marine biology and coastal dynamics in the East China Sea.

5. Conclusions

The ocean color experiment performed on the FY-1 meteorological satellite was limited by the number of VHRSR channels and time. It was only a preliminary attempt. The main objective was to obtain various basic data to set specifications for sensors used in the future and to gain some experience in ocean-color remote sensing.

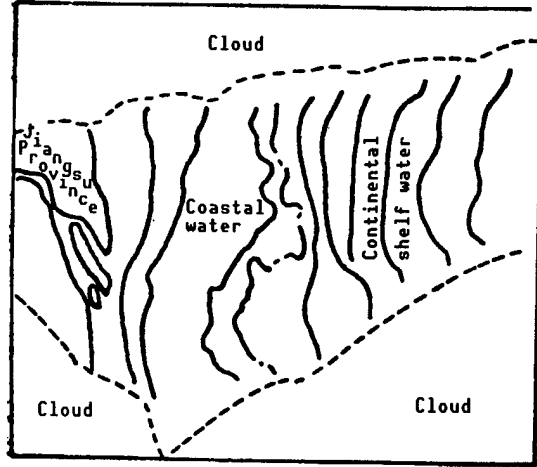


Figure 5. Turbidity Distribution in
East China Sea

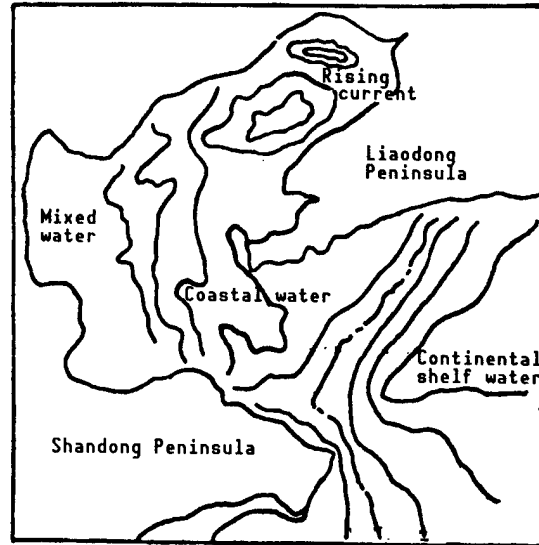


Figure 6. Uprising Current and
Turbidity Distribution in
Bohai Wan

Based on the analysis of ocean color data gathered by FY-1 along China's coast, especially pictures of the East China Sea and Bohai Wan, this information provided on-site data for the study of coastal water systems and uprising currents. As we dig deeper into ocean surface temperature sensing and other applications, we can see very bright prospects for quantitative treatment and applications of the data gathered by FY-1.

Acknowledgement

The authors wish to thank the Satellite Meteorology Center of the State Meteorological Administration for providing the original data and pictures for this work.

References

1. Stumpf, R.P., "NOAA Technical Memorandum NESDIS AISC 7, U.S. Department of Commerce, Washington, D.C., 1987, pp 1-50.
2. Austin, R., "Optical Aspects of Oceanography," Academic Press, New York, 1974, pp 317-345.
3. Clark, D.K., MARINE SCIENCE, Vol 13, 1981, pp 227-238.
4. Gordon, H.R. and Clark, D.K., APPLIED OPTICS, Vol 20, 1981, pp 4175-4180.
5. Gower, J.F.R., "Remote Sensing of Shelf Sea Hydrodynamics," Elsevier, Amsterdam, Oxford, 1984, pp 1-24.

6. Sturm, B., "Remote Sensing Applications in Marine Science and Technology," NATO ASI series, 1983, Dordrecht, pp 137-168.
7. Sathyendranath, S. and Morel, A., "Remote Sensing of Shelf Sea Hydrodynamics," Elsevier, Amsterdam, Oxford, 1984, pp 323-359.
8. Sturm, B., "Oceanography From Space," Plenum Press, New York, 1981.

Technical Development of Visible-Infrared Scanning Radiometer

90FE0171B Shanghai HONGWAI YANJIU [CHINESE JOURNAL OF INFRARED RESEARCH] in Chinese Vol 9 No 2, Apr 90 pp 81-90 (Ms received 16 Aug 89)

[Article by Gong Huixing [7895 1920 5281] of Shanghai Institute of Technical Physics, Chinese Academy of Sciences, Shanghai, 200083, China: "Technical Development of Visible-Infrared Scanning Radiometer on Board FY-1 Meteorological Satellite"]

[Text] Abstract

This paper reviews the technical development process—consisting of medium-, high-, and very-high resolution development stages—of the visible and infrared scanning radiometer on the FY-1 meteorological satellite. In addition, it systematically summarizes the major technical hurdles encountered in every stage, the solutions and the technical specifications reached.

Key words: Meteorological satellite, scanning radiometer.

1. Introduction

On 7 September 1988 China launched its first polar-orbit meteorological satellite (see Figure a of color inserts) [see color section below]. It was delivered by a three-stage Long March 4 launch vehicle to sun-synchronous orbit with an altitude of 901 km at an inclination angle of 99.1°. Its period is 102.86' [minutes].

The main remote sensor on board this satellite is a very-high-resolution scanning radiometer [VHRSR] which is used to obtain visible and infrared pictures of the Earth to determine the ocean color. Based on the amplitude of the output signal, it can quantitatively measure the radiance of the target. It was developed in three stages—i.e., a 48-rpm medium-resolution scanning radiometer, a 120-rpm high-resolution scanning radiometer, and a 360-rpm very-high-resolution scanning radiometer—over a period of 15 years.

This VHRSR is China's first onboard visible and infrared remote sensor. As a remote sensor in space, its technical development was limited by three factors: technical completeness of the meteorological satellite engineering system (including satellite, launch vehicle, launch site construction,

tracking and control network, receiving and application systems), compatibility with existing polar-orbit cloud-pattern ground receiving stations, and performance of the remote sensor itself. Since this was the first sun-synchronous satellite, it took time and money to construct a launch site and to develop a launch vehicle. During this period, the meteorological satellite in the United States developed from ITOS to TIROS-N. The detection limit was increased by three-fold and the transmission of cloud patterns went from analog to digital. Our ground stations were also modified accordingly. This is why we changed the design and detection performance of the scanning radiometer three times.

2. Medium-Resolution 48-rpm Visible-Infrared Scanning Radiometer

The design of the medium-resolution 48-rpm visible-infrared scanning radiometer began in 1974. This was the first-generation prototype developed. It did not employ the TV-camera-based cloud picture system onboard the TIROS and ESSA weather satellites developed in the United States in the 1960's and adopted a mechanical optical scanning method to obtain visible and infrared cloud pictures simultaneously. Thus, it realized the goal for a polar orbit to cover the entire globe in 12 hours.

The scanning radiometer employs a 45° plane reflector for scanning. The axis of rotation coincides with the direction of flight. Figure 1 [photograph not reproduced] shows the external appearance of the medium-resolution scanning radiometer (MRSR) and Figure 2 shows its optical path. It has two detection bands, i.e., 0.55~0.83 μm and 10.5~12.5 μm. The optical aperture is 120 mm. The visible channel has a 500-mm focal length and its IFOV [instantaneous field of view] = 4 mrad. The detector is a Si photodiode, 3 x 3 mm² in size and 0.3 A/W in responsivity, with a dark current of 1 x 10⁻⁸ A. The infrared detector is an immersion-type thermistor. Its light-sensitive surface is 0.2 x 0.2 mm, time constant $\tau_0 = 2$ ms, $D^* = 1 \times 10^8 \text{ cm Hz}^{1/2} \text{W}^{-1}$. The infrared channel was designed to use a pupil imaging scheme and IFOV was restricted by a mechanical diaphragm. Originally, the specification was IFOV = 8 mrad. However, because of the total reflection of focused light at the germanium super hemispherical mirror, the actual IFOV was only 5.8 mrad. The use of a thermistor as an infrared detector presented another problem. Its time constant $\tau_D = 2$ ms, which is equivalent to 80 Hz. It cannot satisfy the 315-Hz picture signal response bandwidth requirement. Thus, it requires differential correction. The signal to noise ratio (SNR) of the infrared channel decreases in multiples of τ_D/τ_A = 4 (where τ_A is the time constant at 315 Hz).

It was determined that the detection sensitivity of the infrared channel is $NEAT = 1.0 \text{ K}$ (target at 300 K). The detection sensitivity of the visible channel $NEI = 5 \times 10^{-11} \text{ W/cm}^2$, equivalent to that of the scanning radiometer (SR) onboard the ITOS meteorological satellite. Figures 3 and 4 [photograph not reproduced] show ground pictures taken by the visible and infrared channel, respectively. They are very clear.

The visible channel has very high detection sensitivity and the infrared channel can distinguish the clouds from the surface underneath. The design

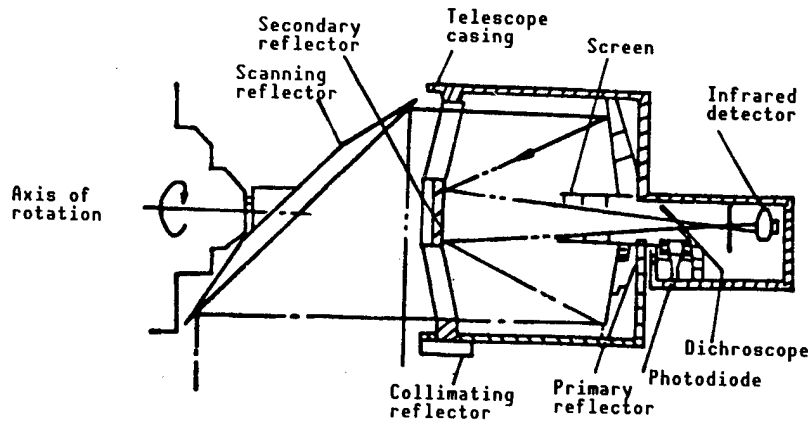


Figure 2. Optical Configuration of 48 rpm Medium-Resolution Scanning Radiometer

targets were met. The performance characteristics of the 48-rpm medium-resolution visible-infrared scanning radiometer are compared to those of the SR on board the ITOS satellite (see Table 1).

Table 1. Performance Comparison of 48-rpm MRSR With SR on ITOS Satellite

Item		48 rpm MRSR	ITOS SR
Spatial resolution (mrad)	Visible	4	2.7
	Infrared	5.8	5.4
Detection band (μm)	Visible	0.55~0.83	0.52~0.73
	Infrared	10.5~12.5	10.5~12.5
Detector	Visible	Si photodiode	Si photodiode
	Infrared	Immersion-type thermistor	Immersion-type thermistor
Detector sensitivity	Visible	$\text{NEI} \leq 5 \times 10^{11} \text{W/cm}^2$	$\text{NEI} \leq 1.7 \times 10^{11} \text{W/cm}^2$
	Infrared	$\text{NEAT} \leq 1.0 \text{ K}$	$\text{NEAT} \leq 1.0 \text{ K}$
Optical aperture (mm)		120	120
Scanning rate (rpm)		48	48
Output signal		Analog picture	Analog picture
Power consumption (W)		20	6.6
Weight (kg)		20	5.9

3. 120-rpm High-Resolution Visible-Infrared Scanning Radiometer

The United States launched the third-generation meteorological satellite TIROS-N in 1978. It has a five-channel advanced very-high-resolution radiometer (AVHRR). After onboard real-time information processing, it simultaneously transmits expanded digital HRPT (high-resolution picture transmission) cloud pictures at six lines/s and geometric-distortion-corrected automatic-picture-transmission (APT) analog cloud pictures at two lines/s. To accommodate these features, a 1700-MHz HRPT digital cloud picture receiving station was constructed. The facsimile machine in the APT station was modified to receive APT cloud pictures at two lines/s. Therefore, it was decided to develop a 120-rpm visible-infrared scanning radiometer in 1977 as an engineering prototype for China's weather satellite.

In a 900-km-high sun-synchronous orbit, sub-satellite point speed is 6.49 km/s. At a scanning rate of 120 rpm, in order to make neighboring scanning lines link, the instantaneous field of view should be 3.6 mrad and the electronic character bandwidth is 1.75 kHz. Users require that detection sensitivity of the infrared channel be $NE\Delta T \leq 0.8$ K. Obviously, the D^* and the response time of the thermistor infrared detector cannot meet this requirement. Thus, a HgCdTe infrared detector was used; its operating temperature is 105 K and it was cooled passively by a radiation refrigerator.

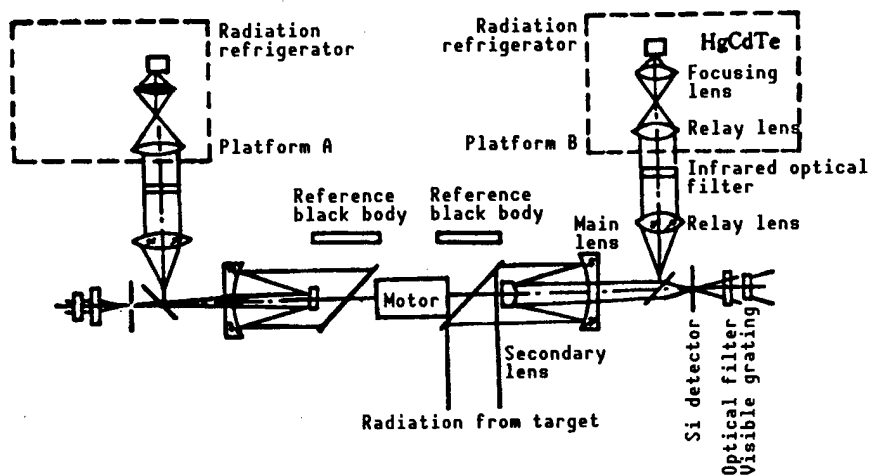


Figure 5. Optical Configuration of 120-rpm Scanning Radiometer

At 900 km, the earth field angle is 122.4° . In order to simultaneously transmit visible and infrared pictures in every scan line, just as with the APT of the TIROS-N satellite, an optical configuration as shown in Figure 5 was adopted. It consists of two independent optical systems of identical optical parameters. One has a driver which allows two 45° scanning mirrors, 180° different in phase, to receive earth radiation alternately. One channel on each side is used, via time-division parallel linking, to create a two-channel signal output for every scan line. The infrared channels of both optical systems are $10.5\text{--}12.5 \mu\text{m}$. The visible channels are $0.55\text{--}0.75 \mu\text{m}$ and $0.52\text{--}1.1 \mu\text{m}$, respectively, in order to differentiate clouds from snow. Upon

command, the output may be in the following three combinations: visible 1-visible 2, visible 1-infrared, and visible 2-infrared.

The main optical system consists of a double-spherical-lens collapsible telescope with an aperture of 124 mm and focal length of 668 mm. The instantaneous field of view (IFOV) of the visible channel, determined by a mechanical diaphragm which is $2.4 \times 2.4 \text{ mm}^2$, is 3.6 mrad. Because the radiation refrigerator is too bulky, it was separately installed from the optical scanner and coupled through a collimated light beam in order to minimize the effect of installation error on image quality and viewing field alignment. The effective focal length of the infrared channel is 123 mm and the detector size is $0.36 \times 0.36 \text{ mm}^2$ and the IFOV is $2.9 \times 2.9 \text{ mrad}$.

The visible channel is a Si photodiode with a photosensitive surface of $3 \times 3 \text{ mm}^2$. The responsivity is 0.4 A/W , the dark current is $1 \times 10^{-8} \text{ A}$, and the junction capacitance is 50 PF. Due to improved amplifier noise, visible-channel detection sensitivity $\text{NEI} \leq 1.6 \times 10^{-11} \text{ W/cm}^2$. The infrared detector is an optical waveguide $\text{Hg}_{0.8}\text{Cd}_{0.2}\text{Te}$ detector which operates at 105 K. Initial design requirement was $D^* \geq 5 \times 10^8 \text{ cm Hz}^{1/2} \text{ W}^{-1}$. In 1981, it actually reached $6 \times 10^9 \text{ cm Hz}^{1/2} \text{ W}^{-1}$. There was substantial improvement in detector performance.

The performance of the radiation refrigerator must be tested in a vacuum container with a 30 K background; cooling down to 105 K is a prerequisite condition to test the performance of the infrared channel. Three tests were done between 1980 and 1982 and it was found that the secondary block of the radiation refrigerator could reach 100 K and could be heated to maintain at 105 K. The detection limit of the infrared channel is $\text{NEAT} \leq 0.2 \text{ K}$. The degree of uncertainty of the infrared channel is 2 K. A large-aperture-cavity surface black body is used as a standard radiation source.

The stability of the rotation rate of the scanner directly affects picture quality. Usually, the scanning flutter amplitude has to be less than 1 pixel. The 48-rpm scanning radiometer uses a 1500-rpm magnetic hysteresis synchronous motor and is driven by a two-stage gear at a 31.25 reduction ratio. In order to improve scanning accuracy and simplify lubrication in space, the 120-rpm scanning radiometer is directly driven by a TDB-500 permanent magnetic synchronous motor. It operates in electromagnetic deceleration principle and the deceleration ratio is 50. The specific synchronizing moment of force is $\frac{dM}{d\alpha} = 45000 \text{ gcm/rad}$. The scanning flutter is $\leq 1.1 \text{ mrad}$, which satisfies the image quality requirement.

Quantitative measurement of target temperature requires that the optical opening of the scanning radiometer not be blocked. To this end, it is necessary to investigate the long-term lubrication problem in the ultrahigh vacuum ($1.33 \times 10^{-8} \text{--} 10^{-9} \text{ Pa}$) in orbit. We selected an oiled-bearing support and labyrinth-packing scheme for the rotating cut axis. The molecular weight of the lubricant is $M = 8047$. At $T = 327 \text{ K}$, the saturated vapor pressure is $P = 1.33 \times 10^{-5} \text{ Pa}$. The annual loss of oil vapor through two sealing rings is Q , given by:

$$Q = 1.02 \times 10^4 P \sqrt{MT} \frac{(r_2^2 - r_1^2)(r_2 - r_1)}{l} \text{ g/yr} = 1 \text{ mg/yr}$$

where r_2 , r_1 , and l are the inner diameter of the axial opening, outer diameter of the rotating axis and length of the labyrinth, structure. From October 1980 to April 1981, the scanner was tested in a KM-0.5 oil-free vacuum container at 1.33×10^{-5} Pa; it operated normally, with 3 mg of lubricant lost. The actual amount of oil stored inside is 100 mg, which can meet the need in orbit for over 1 year. Figure 6 [photograph not reproduced] shows a picture taken at the experimental site where scanner life was tested in vacuum.

In order to perform in-flight calibration of the infrared radiometer, it is equipped with internal reference black bodies. Their temperature is remotely sensed by a precision platinum resistance. Since the system response is linear, a two-point calibration is adequate for response rate. The other radiation reference point is the cold space. Its effective black-body temperature is 4 K. In order to eliminate dc voltage drift, the infrared channel amplifier is ac coupled. A dc voltage restoration technique is used when measuring the cold space (see Figure 7) in order to establish the baseline dc voltage corresponding to zero radiation. $RC = T/A$, where T is the scanning period and A is the percentage of signal level drop allowed.

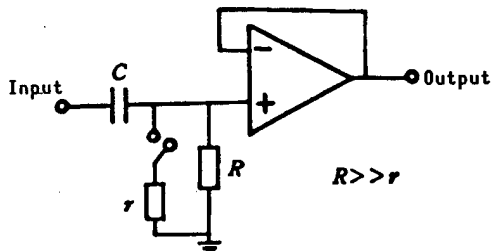


Figure 7. DC-Restoration Amplifier

Figure 8 [photograph not reproduced] shows a picture of the 120-rpm scanning radiometer with a LN₂ Dewar. Figure 9 [photograph not reproduced] shows an aerial photo taken by the scanning radiometer at 400 rpm. The wavelength is 10.5-11.2 μm , IFOV = 3.6 mrad, flight altitude = 3000 m, and NEΔT ≤ 0.2 K.

The performance of the 120-rpm scanning radiometer has been measured. All design specifications have been met. In addition, through a mechanical environmental test, vacuum heating-cooling test, space particle radiation test and half a year of operation of the scanner in an ultrahigh vacuum, an engineering prototype was developed. A comparison of the performance characteristics between the 120-rpm visible-IR scanning radiometer and the APT on board a TIROS-N satellite is given below (see Table 2).

4. 360-rpm Very-High-Resolution Scanning Radiometer (VHRSR)

When satellite orbit altitude and global coverage period remain unchanged, the detection sensitivity of the scanning radiometer is inversely proportional to the cube of the viewing field. The D^* of the HgCdTe infrared detector improved

Figure 2. Performance Comparison Between 120-rpm Scanning Radiometer and TIROS-N APT

Item	120-rpm Scanner	TIROS-N APT
Spatial resolution (mrad)	3.6	3.9 (flight direction)
Detection band (μm)	0.55~0.75 0.52~1.11 10.5~12.5	0.58~0.68 0.725~1.1 3.55~3.93 10.5~11.5 11.5~12.5
Detector	Si photodiode HgCdTe	Si photodiode InSb HgCdTe
Detector temperature (K)	105	105
Cooling method	Radiation	Radiation
Detector sensitivity	Visible: $\text{NEI} \leq 1.6 \times 10^{11} (\text{W/cm}^2)$ Infrared: $\text{NEAT} \leq 0.2 (\text{K})$	Infrared: $\text{NEAT} \leq 0.18 (\text{K})$
Optical aperture (mm)	124	200
Scanning rate	120 (rpm)	2 (lines/s)
Output signal	Uncorrected analog picture similar in format to TIROS-N	Analog cloud picture corrected for distortion
Power consumption (W)	28 (2 units)	
Weight (kg)	58 (2 units)	

by an order of magnitude in 1978-1981. If the optical aperture is increased from 124 mm to 200 mm, the sensitivity of the system can be raised by 26 fold. By doing so, spatial resolution can be increased by three fold while satisfying the prerequisite that the sensitivity of the infrared channel $\text{NEAT} \leq 0.8 \text{ K}$. Thus, it was feasible to develop a 360-rpm VHRSR similar to the AVHRR on the TIROS-N satellite. However, more work is needed to be done on the optical system, beryllium mirror, scanner, three-element Si detector, and real-time image [photograph not reproduced] technique.

The users require that the 360-rpm VHRSR be able to simultaneously transmit processed signals from five digital HRPT channels at 6 lines/s and distortion-corrected pictures from two APT analog channels at 2 lines/s in the same format as TIROS-N for reception by our existing stations in a compatible manner, as well as by the rest of the world.

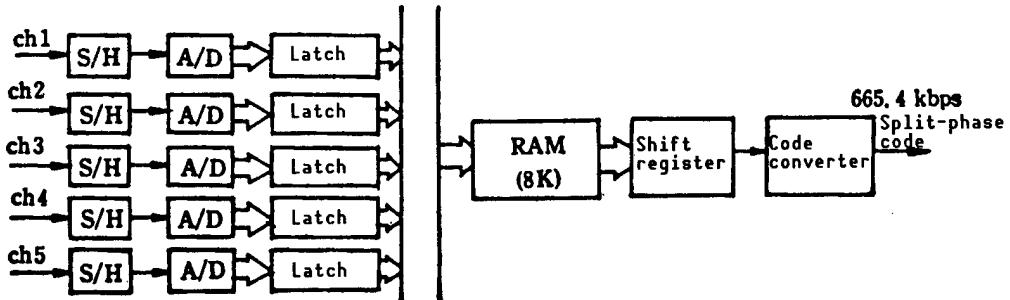


Figure 10. HRPT Real-Time Information Buffering Processor

Figure 10 shows the flowchart of HRPT information processing. It was designed based on a 5-channel analog signal mode. The signal bandwidth is 15.7 kHz. In order to lower power consumption and improve system reliability, it uses five 8-bit A/D [analog-to-digital] converters and operates in parallel. The conversion frequency is 39.924 kHz. Earth view signals are collected within $\pm 55.4^\circ$. Each channel has 2048 words and each scan line has 10240 characters of data. In order to raise conversion accuracy, lower conversion rate and take full advantage of the high-speed load feature of the RAM, converted data is stored in registers and written into the RAM in the next conversion period. The load speed is 199.62 kbyte/s. Under the control of the logic circuit, it writes and reads at the same time. The picture data is buffered by writing three times and reading once. After a series of conversions, the last digit has two added zeroes, similar to the HRPT or TIROS-N. Thus, we created a 10 bit/word, 665.4 kbps 5-channel time-division-multiplexed digital cloud-picture signal which realized a 332.4° expansion of a $\pm 55.4^\circ$ picture of the Earth about the time axis.

Due to the Earth's curvature and the dependence of the distance between the satellite and the point of observation upon the scanning nadir angle α , ground image resolution along the scanning direction Δl is:

$$\Delta l = 1.2 \times 10^{-3} \left[\frac{(R+H) \cos \alpha}{\sqrt{1 - \left(\frac{R+H}{R} \right)^2 \sin^2 \alpha}} - R \right];$$

where R is the radius of the Earth and H is the altitude of the orbit. In Figure 11, the dotted line shows ground resolution as a function of scanning nadir angle α . In order to correct for geometric distortion, picture signals are divided into 10 zones based on the nadir angle α and sampling is done at a different frequency in each zone (see Table 3). The data is stored into the RAM after A/D conversion and then read out linearly in order to correct for scanning geometric distortion in zones. The average ground resolution is approximately 4 km (see Figure 11). Picture correction is done by the APT

information processor, which has two channels of command-controlled analog picture signal input. Each channel has its own independent A/D and 1 k of RAM with a total sampling size of 909 characters. The two channels work alternately to operate serially in time. After D/A conversion, remote sensing data is inserted to form a 2 lines/s analog picture similar to that of the APT of the TIROS-N.

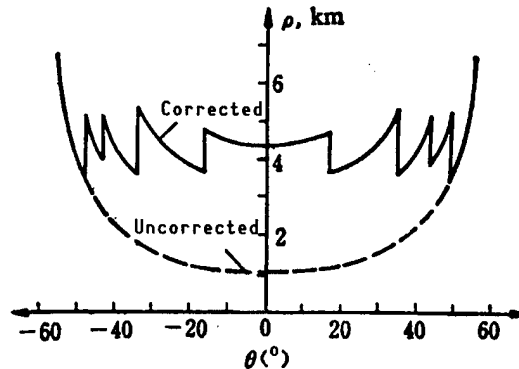


Figure 11. Ground Resolution of APT Image Along the Scanning Direction

Table 3. Information Characteristics of APT Image After Zone-Linearization

Scanning nadir angle α (°)	Sampling frequency (kHz)	Ground resolution to scanning direction (km)
$\pm 0\text{--}16.8$	9.931	4.32~4.81
$\pm 16.8\text{--}34.7$	13.308	3.61~5.37
$\pm 34.7\text{--}43.6$	19.962	3.58~5.19
$\pm 43.6\text{--}48.6$	26.616	3.89~5.27
$\pm 48.6\text{--}55.4$	39.924	3.52~6.80

The VHRSR was originally designed to have two visible and one infrared channel. In 1985, in order to expand its capability, two ocean-color observation channels were added. All total, there are five channels, i.e., 0.48~0.53 μm , 0.53~0.58 μm , 0.58~0.68 μm , 0.725~1.1 μm , and 10.5~12.5 μm . The optical configuration of the scanner is shown in Figure 1 on page 92 of this journal [see "Optical Design of VHRSR," later in this special issue]. The optical aperture is 200 mm. The main optical system is formed by coaxial and confocal parabolic surfaces. Since the light output is parallel, two infrared collimating lenses in the coupling optical path of the radiation of refrigerator can be saved. Infrared/visible beam splitters with an index of refraction of greater than 0.9 in the infrared are used to improve the optical efficiency of the infrared channels. The HgCdTe detector is $0.21 \times 0.21 \text{ mm}^2$ in size. The focal length is 174 mm and its IFOV is 1.2 mrad. The $0.725\text{-}\mu\text{m}$ cutoff optical filter can also be used as a visible/infrared color splitter. In conjunction with the response cutoff wavelength of the Si detector, it forms the $0.725\text{--}1.1\text{-}\mu\text{m}$ band. The radiation reflected by the visible/near-infrared

splitter is refocused to pass through a microtricolor optical filter to the assigned bands. It was received by a three-element Si detector to form three visible channels.

The 45° scanning beryllium reflector was machined, polished and coated. Its dimensions are 205 x 290 mm². It was driven by a magnetic hysteresis synchronous motor with 30 pairs of poles. The synchronous torque is 350 g·cm and the rotational period stability is 1.5×10^{-4} . In order to reduce weight, the main structures of the optical scanner and electronic lines are made of cast magnesium. A picture of the optical scanner of the 360-rpm VHRSR and information processor is shown in Figure b of the color insert in this issue [see special color section below].

The radiation opening of the radiation refrigerator is 360 x 262 mm². At 105 K, the chilling reserve capacity is 10 mW. Ground environmental protection of the radiation refrigerator plays an important role in its performance in orbit. To this end, a command-controlled heater is installed on the primary cooling block and its power is 20 W. The cooling block temperature is controlled at 32°C by a relay in order to bake off gases in the early stage of orbiting and to decontaminate the cooling block during operation. The opening of the radiation refrigerator is also equipped with an anti-contamination mask (see Figure 3 of the color inserts in this issue) in order to maintain the cleanliness of the optical mirrors and to raise the temperature of the secondary cooling block during degassing. The radiation refrigerator is stored in a vacuum nitrogen-filled vessel. The decontamination mask uses an electromagnetic double lock and measures were taken to avoid cold-soldered joints. It could be unlocked reliably at -90°C upon ground command.

The scanning radiometer was calibrated prior to launch. Solar radiation was used as the standard to calibrate the visible and near-infrared channels. After correcting the atmosphere transmittance and background radiation of the sky, the calibration accuracy is 5 percent. The detection sensitivity for each channel is $NE\Delta\rho \leq 0.15$ percent. The infrared channels were evaluated and calibrated in a KM-2 vacuum vessel (see Figure 12). The cold background was cooled down to 15~20 K with helium and the standard radiation source was a double-cavity surface black body. The accuracy of the black body is 0.34 K and the calibration is good up to 1.0 K. The detection sensitivity of the infrared channel was measured to be $NEAT \leq 0.20$ K. The visible and infrared channels have a viewing field alignment accuracy of better than one-fifth pixel. The infrared channels have $MTF \geq 0.25$ and visible channels have $MTF \geq 0.4$.

The performance characteristics of the VHRSR are compared to those of the AVHRR of the TIROS-N satellite and the results are shown in Table 4.

5. Operation in Orbit

The VHRSR was launched into orbit on 7 September 1988. The four visible and near-infrared channels immediately began to function and sent clear pictures to earth (see Figure i of the color inserts in this issue). Both ground resolution and detection sensitivity were found to meet design specifications. The scanner is capable of distinguishing clouds, crops, water/land boundaries

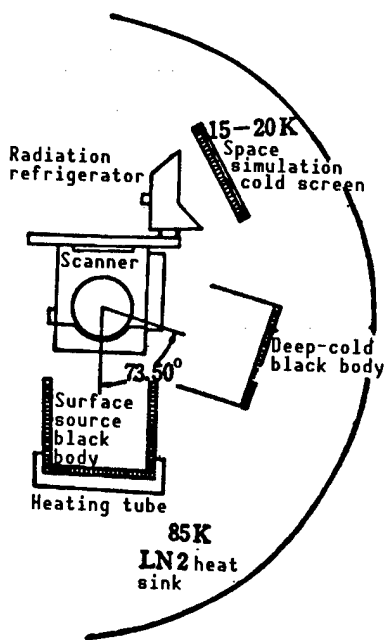


Figure 12. Geometric Layout of Scanning Radiometer, Standard Surface Source Black Body, and Deep-Low-Temperature Black Body in the Vacuum Vessel

Table 4. Performance Comparison Between FY-1 VHRSR and TIROS-N AVHRR

Item	VHRSR	AVHRR of TIROS-N
Detection bands (μm)	0.48~0.53; 0.53~0.58; 0.58~0.68; 0.725~1.1; 10.5~12.5	0.58~0.68; 0.725~1.1; 3.55~3.93; 10.5~11.5; 11.5~12.5
Spatial resolution (mrad)	1.2	1.3
Ground resolution (km)	1.1	1.1
Detectors	Si and HgCdTe	Si, InSb, and HgCdTe
Cooling mode	Radiation refrigerator	Radiation refrigerator
Detection sensitivity	Visible and near IR, $\text{NE}\Delta\rho \leq 0.15\%$; thermal IR, $\text{NE}\Delta T \leq 0.20\text{K}$	Visible and near IR, $\text{NE}\Delta\rho \leq 0.10\%$; thermal IR, $\text{NE}\Delta T \leq 0.15\text{K}$
Dynamic detection range	$\text{Ch}_1, \text{Ch}_2 0\sim 20\%$ $\text{Ch}_3, \text{Ch}_4 0\sim 85\%$ $\text{Ch}_5 200\sim 320\text{ K}$	$\text{Ch}_1, \text{Ch}_2 0\sim 105\%$ $\text{Ch}_3, \text{Ch}_4, \text{Ch}_5 180\sim 330\text{K}$
Optical aperture (mm)	200	200
Scanning rate (rpm)	360	360
Output format	Similar to TIROS-N	5 digital, 2 analog cloud-picture channels
Onboard processing	Similar to TIROS-N	High-speed digital data buffering, scanning, geometric- distortion correction
Weight (kg), power (W)	47, 27	Approximately 32, ≥ 35

and color. The infrared channel began to operate on 20 September after the radiation refrigerator reached 105 K. Initial infrared pictures are very clear (see Figure h of the color insert in this issue). The spatial resolution is 1.2 mrad and detection sensitivity is NEΔM = 0.5 K.

Water-vapor condensation on the optical components inside the cold radiation refrigerator caused the infrared channel signal to rapidly deteriorate. This is primarily because the launch environment was too humid and the sensing apparatus was not properly protected. In spite of heating and degassing in orbit, there was still a great deal of water vapor left. This problem still requires further investigation.

References

1. Lauritson, L., et al., "Data Extraction and Calibration of TIROS-N/NOAA Radiometers NESS-107," 1977, pp 44-46.
2. NASA-CR-156682.
3. Karoli, A.R., et al., APPLIED OPTICS, Vol 6, 1967, p 1183.
4. Gong Huixing and Zheng Qinbo, "Infrared Radiation Calibration of a Space Borne Scanning Radiometer," Proceedings of the Beijing International Symposium on Remote Sensing, November 1986, pp 18-22.

Optical Coatings

90FE0171C Shanghai HONGWAI YANJIU [CHINESE JOURNAL OF INFRARED RESEARCH] in Chinese Vol 9 No 2, Apr 90 pp 129-134 (Ms received 03 Jul 89)

[Article by Xu Buyun [6079 2975 0061], Zhu Cuiyuan [2612 5050 1254], and Zhu Bingsheng [2612 3521 3932] of Shanghai Institute of Technical Physics, Chinese Academy of Sciences, Shanghai, 200083, China: "Optical Coatings for Meteorological Satellite"]

[Text] Abstract

This paper presents the basic design principles, structures, and applications of several optical thin-film devices used in meteorological satellites. The paper also lists coating types, coating materials, and measured spectral curves. These devices have already been successfully used in the field.

Key words: Color splitter, combined optical filter, band-pass optical filter.

1. Introduction

In general, a meteorological satellite relies on a multichannel scanning radiometer to obtain various kinds of data on the earth's surface and the atmosphere. The main remote-sensing apparatus on the meteorological satellite launched by China is a five-channel optical scanning radiometer. A variety of optical thin film devices comprised of different coatings are used to realize the five channels. In the optical system of the scanner, in addition to high-efficiency reflective coatings and antireflective coatings, there are a number of special optical thin film devices, such as broadband color splitters, visible channel optical filters, and infrared channel optical filters. Not only good optical characteristics but also high reliability must be ensured in the design and manufacture of these thin film optical devices. The following is a brief introduction of some optical thin film devices already successfully used on meteorological satellites.

2. Broadband Color Splitter

A broadband color splitter splits optical radiation from the earth into several bands, such as a splitter that transmits visible light and reflects infrared or a splitter that reflects the visible and transmits near-infrared.

A broadband color splitter can be designed as a metal-dielectric film combination or an all-dielectric film structure.

2.1 Broadband Color Splitter That Transmits Visible and Reflects Infrared

Figure 1 shows a visible-transmissive and infrared-reflective broadband color splitter that is actually used on a meteorological satellite. It is made of a metal-dielectric combined structure. It was designed based on the potential transmittance concept described in reference [1]. In Figure 1, the ratio of the optical energy T transmitted across interface b to the optical energy $1-R$ transmitted across interface a is defined as the potential transmissivity ψ , i.e.,

$$\psi = \frac{T}{1-R};$$

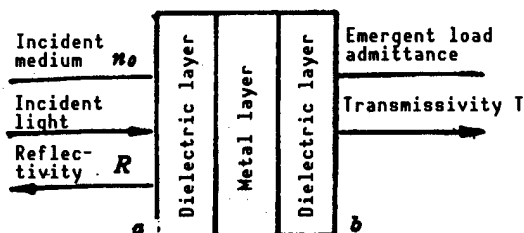


Figure 1. Structure of Color Splitter
With Metal-Dielectric Layers

With regard to the transmitted beam, in order to raise T , it is necessary to increase ψ and lower R . The potential transmissivity is determined by the optical constants of the metal thin film and the emergent load admittance and is independent of the incident medium. In order to raise ψ , it is necessary to design the optical emergent load admittance. The actual transmissivity T of the coatings is not only dependent upon the potential transmissivity but also related to the incident medium. By combining the metal layer and the emergent load admittance into one new substrate, an antireflective coating was designed to match the incident medium with this new substrate in order to lower R and thus raise transmissivity T . The infrared part, because it deviates significantly from the optical matching condition, shows high metal reflection characteristics. Calculation shows that the coating assembly is

$$n_s | 13-30\text{nmZnS} | 11-18\text{nmAg} | 25-40\text{nmZnS} | n_0.$$

Satisfactory visible-transmitting, infrared-reflecting broadband color splitting effects can be achieved. n and n_0 are the indices of refraction of the substrate and the incident medium, respectively. Here, $n_s = 1.47$ (quartz) and $n_0 = 1.0$ (air). In actual fabrication, each different layer has a different substrate temperature. This not only results in ideal color-splitting curves but also tighter films for better reliability. Figure 2 shows a measured curve of transmitting in visible and reflecting in infrared.

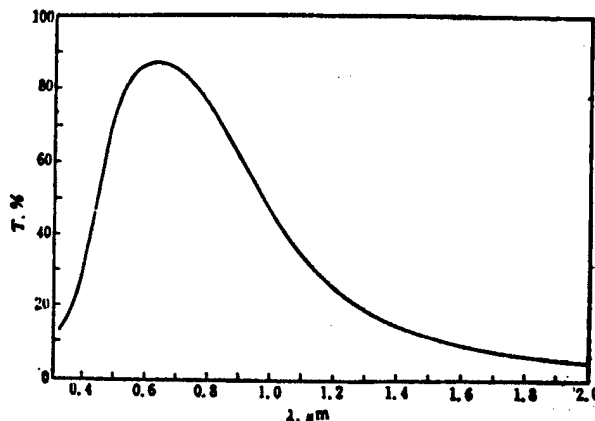


Figure 2. Measured Curve of Color Splitter Transmitting in Visible and Reflecting in Infrared

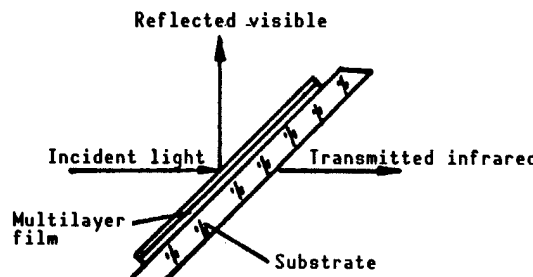


Figure 3. Color Splitter That Reflects in Visible and Transmits in Near-Infrared

2.2 Broadband Color Splitter Reflecting Visible and Transmitting Near-Infrared

Figure 3 shows a color splitter which reflects visible and transmits near-infrared and is fabricated with multiple dielectric layers on a flat piece of glass. Because an optical coating used on a satellite must be very reliable, soft films (e.g., ZnS, MgF₂) usually used in the visible region are no longer suitable. Since high reflectivity over the entire visible region is required, a considerable number of layers are involved. The integrity and long-term reliability of such a multilayer assembly is poor. Hence, hard films (e.g., ZrO₂, TiO₂, and SiO₂) are more appropriate. In actual practice, ZrO₂ is a high-refractivity material and SiO₂ is a low-refractivity material. A multilayer structure is fabricated from these two materials. The coating system was designed based on the long-wave-pass design method.²

In the visible region, the basic long-wave-pass coating system is:

$$n_s | (0.5H0.5L)^3 | n_0;$$

where n_s and n_0 are the indexes of refraction of the substrate and incident medium, respectively, H is the one-fourth-wavelength high-refractivity layer, L is the one-fourth-wavelength low-refractivity layer, and S is the basic number of periods. The reflection band of the above coating system is fairly narrow. In order to ensure high refractivity in the visible, it is necessary to have several such coating systems. Based on calculation, the following coating system can meet such a requirement.

$$n_s | 0.77(0.5H0.5L)^{11} 0.84(0.5H0.5L)^{10} (0.5H0.5L) |^{11} n_0$$

where $n_s = 1.47$ (quartz), $n_H = 1.9$ (ZrO₂), $n_L = 1.44$ (SiO₂), and $n_0 = 1.0$ (air). The design wavelength is $\lambda = 0.96 \mu\text{m}$. The multilayer hard films are prepared with an electron gun device. The three coatings are deposited at three control wavelengths and each coating system is coated in three steps. The measured curve of the above coating system is shown in Figure 4.

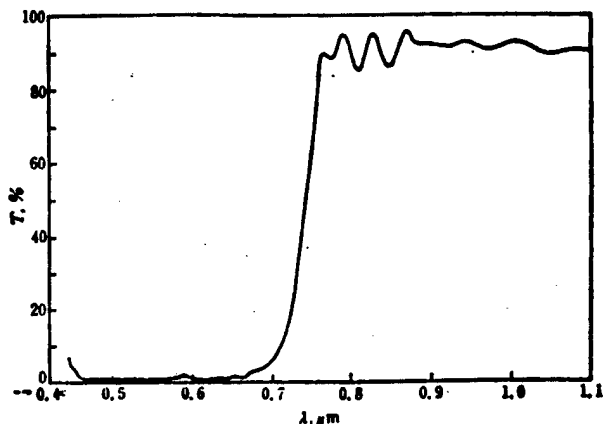


Figure 4. Measured Curve of Visible Light Reflected by and Near-Infrared Transmitted by Color Splitter

3. Three-Channel Visible Combined Filter

This is a vital optical thin film device used on board the FY-1 meteorological satellite. It is placed at the window of the three-element Si detector. The sensing element of the detector is 1 mm^2 and the sensing elements are 0.57 mm apart. To this end, the filters for these three visible channels were combined into one by design. The structure of the combination is shown in Figure 5.

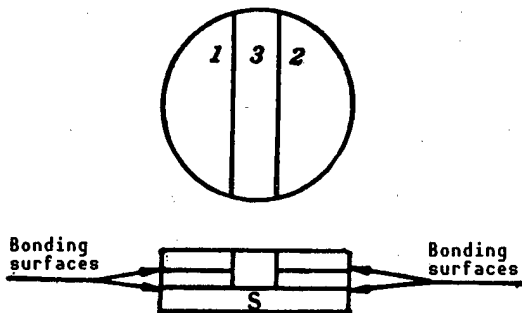


Figure 5. Structure of Combined Visible Three-Channel Filter

3.1 Design of the Visible Three-Channel Filter

The design of channels 1 and 2 in Figure 5 uses a band-pass coating glued to a glass color filter. In order to make the visible channel curve more rectangular-like, the multilayer coating system has three half-wavelength structures:

quartz structure|HLH(HLHLHLH)²HLH|air

where H and L are as described earlier. Based on the bandwidth equation given in reference [2],

$$\frac{2\Delta\lambda}{\lambda_0} = \frac{2}{\pi} \sin^{-1} \left[\frac{2\left(\frac{n_H}{n_L}-1\right)}{\left(\frac{n_H}{n_L}\right)^4} \right]$$

Let $n_H = 2.38$ (ZnS), $n_L = 1.38$ (MgF_2), and λ_0 be the center wavelength for channels 1 and 2, the relative bandwidth of the above coating system is then 10.7 percent, which is slightly larger than needed. By gluing suitable filters to it, the required bandwidths for channels 1 and 2 can be obtained. The color filter can also cut off the secondary pass band on the short-wavelength side. Channel 3 can be made by gluing the short-wave-pass coating on the substrate S to a suitable filter. The long-wave-pass coating on S also cuts off the long-wave-side secondary pass band of channels 1 and 2.

3.2 Design of Short-Wave-Pass Coating System

The design requirements of the short-wave-pass coating system on substrate S in Figure 5 include that the $0.48\text{--}0.68\text{-}\mu m$ channel should be a low-ripple, high transmissivity channel and that the $0.7\text{--}1.05\text{-}\mu m$ channel should have good secondary-peak cutoff characteristics. After taking reliability into account, the bonding surface on the substrate S was coated with a series of slightly modified short-wave-pass soft films:

quartz substrate|1.2H1.1L(HL)⁶H1.1L1.2H|air,

where n_H is 2.35 (ZnS) and $n_L = 1.38$ (MgF_2). The purpose of modification is to reduce the ripple in the $0.48\text{--}0.68\text{-}\mu m$ transmission band. On the nonbonding surface of S, the following hard short-wave-pass coating was applied:

quartz substrate|(0.5LH0.5L)⁵|air,

where $n_H = 1.9$ (ZrO_2) and $n_L = 1.44$ (SiO_2). This coating connects its cutoff band to the cutoff band of the soft coating to achieve a cutoff within the range of $0.7\text{--}1.05\text{ }\mu m$. Figure 6 shows the experimental curves of the three-visible-channel combination of optical filter. The filters were glued with an optical epoxy. The spectral characteristics of this epoxy would not change after repeated temperature cycling ($+40^\circ$ to -40°).

4. $10.5\text{--}12.5\text{-}\mu m$ Infrared Channel Filter

This infrared channel is designed to obtain infrared weather data from the scanning radiometer. There are two ways to form the $10.5\text{--}12.5\text{-}\mu m$ channel. One is to use the transmission characteristics of a $10.5\text{-}\mu m$ long-wave-pass filter in conjunction with the long-wavelength drop-off property of the HgCdTe detector to form a $10.5\text{--}12.5\text{-}\mu m$ channel. The second way is to combine a $10.5\text{-}\mu m$ long-wave-pass filter with a broad band-pass optical filter having a long-wave edge of $12.5\text{ }\mu m$. It is used where the long-wavelength response of the HgCdTe detector is high.

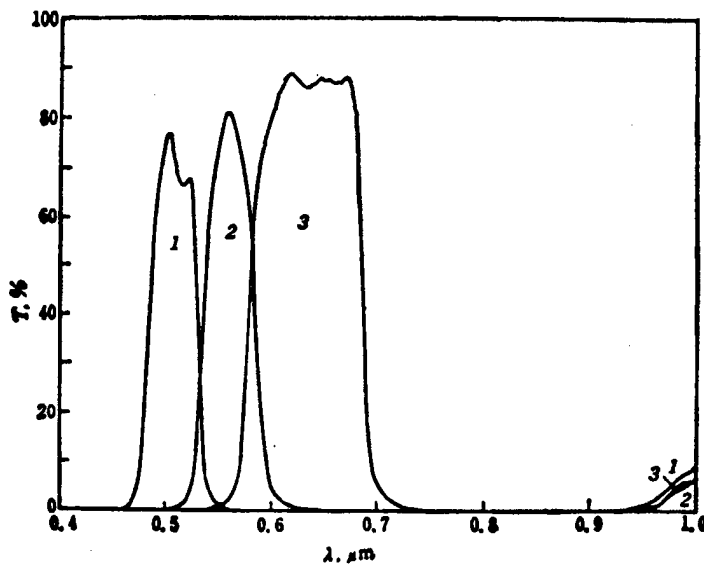


Figure 6. Measured Curves of Combined Filter With Three Visible Channels

4.1 10.5- μm Long-Wave-Pass Filter

Ge is usually used as the substrate for a long-wavelength infrared filter. It is coated with a variety of films of high and low refractivity, such as PbTe, ZnSe or ZnS. Based on references [2] and [3], the basic coating system for a long-wave-pass filter is:

$$(0.5LH0.5L)^3;$$

Several basic coatings of different center wavelengths on top of one another can form an infrared long-wave-pass filter with a wide cutoff region. Based on calculation, the following coating system

$$\begin{aligned} \text{Air} | & 1.5L | 0.32\left(\frac{L}{2}H\frac{L}{2}\right)^3 | 0.56\left(\frac{L}{2}H\frac{L}{2}\right)^5 | \text{Ge} | 0.88\left(\frac{L}{2}H\frac{L}{2}\right)^2 \\ & \left(\frac{L}{2}H\frac{L}{2}\right) | ^7 1.5L | \text{Air} \end{aligned}$$

can result in an ideal 10.5- μm long-wave-pass filter. In the above equation, the indices of refraction of the high and low refractive layers are 5.5 (PbTe) and 2.2 (ZnS), respectively. The design wavelength is 7.2 μm . Figure 7 shows the curve of the actual filter.

4.2 Infrared Broad-Band-Pass Filter (12.5 μm on Long-Wavelength Side of Transmission Band)

A basic coating structure such as (HLH) or (LHL)³ can achieve the widest broadband filter. The higher the order S is, the steeper the transmission band edge becomes. A practical coating system is:

$$\text{Air} | \text{Ge} | L(LHL)^4 | \text{Air}$$

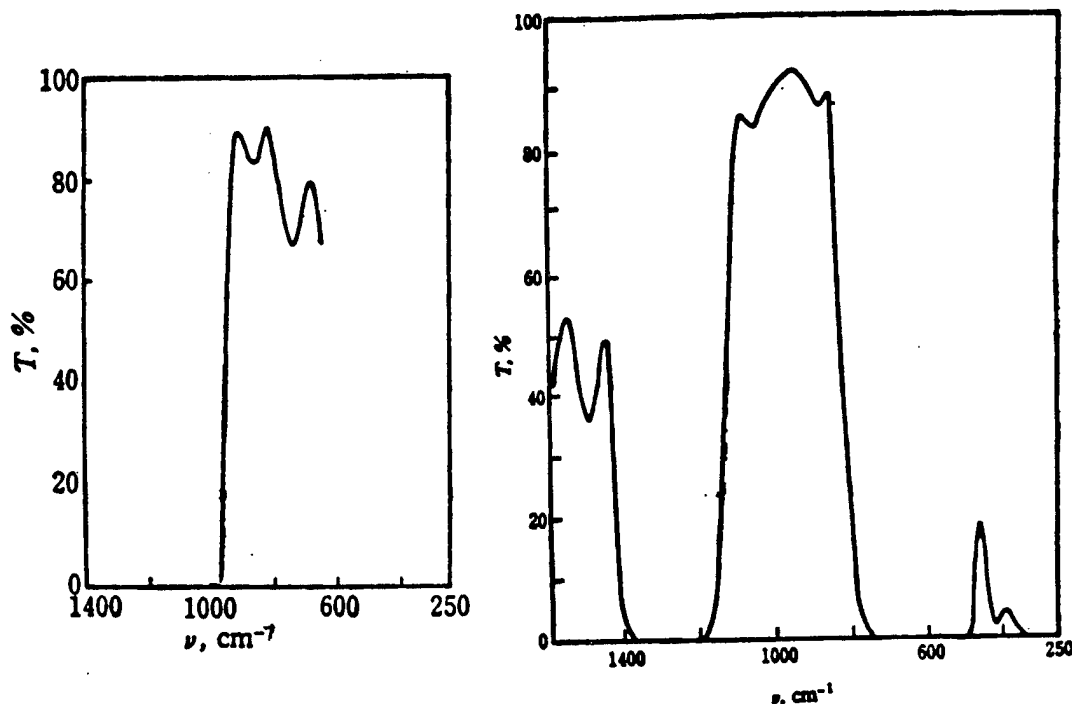


Figure 7. Measured Curve of 10.5- μm Long-Wave-Pass Filter

Figure 8. Measured Curve of Infrared Broadband-Pass Filter (Long-Wave Edge at 12.5 μm)

The coating materials used are PbTe and ZnS, as well. Figure 8 shows the measured curve of the infrared broadband filter.

All infrared long-wave-pass filters and infrared broadband-pass filters mentioned in this paper use PbTe as the semiconductor because of its high index of refraction, which facilitates the design work. However, special caution must be taken in fabricating PbTe films. In particular, substrate temperature and rate of evaporation must be rigorously controlled. Absorption of PbTe film can only be minimized under optimal conditions. The infrared filters prepared in house used a "soft" PbTe coating material,⁴ which is essential for obtaining high-quality infrared filters.

5. Conclusion

In addition to meeting all the spectral characteristics, reliability must be taken in consideration in the selection, design, and fabrication of optical coatings used on a meteorological satellite. All thin film devices must be rigorously tested in simulated environments before they are placed in operation. The devices introduced in this paper have been successfully used on board. Data obtained show that these optical thin film devices can meet the requirements for a meteorological satellite.

References

1. Baumeister, P.W., APPLIED OPTICS, Vol 8, 1969, p 2:423.
2. Macleod, H.A., "Thin-Film Optical Filters," London:Adam, Ltd., 1969, pp 246-251.
3. Yan Yixun [0917 5030 1053], HONGWAI WULI YU JISHU [INFRARED PHYSICS AND TECHNOLOGY], 1973, p 6:61.
4. Yen Yihsun, et al., APPLIED OPTICS, Vol 23, 1984, p 20:3597.

Onboard Preprocessing of Remote-Sensor Signal

90FE0171D Shanghai HONGWAI YANJIU [CHINESE JOURNAL OF INFRARED RESEARCH] in Chinese Vol 9 No 2, Apr 90 pp 99-107 (Ms received 09 Jun 89)

[Article by Weng Chuijun [5040 0987 7486], Li Zhengchang [2621 2973 1603], and Zhou Yanmu [0719 6056 2606] of Shanghai Institute of Technical Physics, Chinese Academy of Sciences, Shanghai, 200083, China: "Onboard Preprocessing of Remote-Sensor Signal"]

[Text] Abstract

This paper describes a real-time preprocessing method for the signals detected by the five-channel scanning radiometer on the FY-1 meteorological satellite. The final output is in the form of HRPT (high-resolution picture transmission) data and APT (automatic picture transmission) data with geometric distortion correction.

1. Introduction

The VHRSR (very-high-resolution scanning radiometer) on board the FY-1 meteorological satellite has five detection channels in the visible and infrared capable of gathering information such as cloud distribution, geomorphology, ocean-surface scenes, and temperature. The purpose of this work is to perform real-time digital picture processing on board and to incorporate parameters such as reference-black-body signal, temperature, and correction factors which are necessary for further derivation. Finally, HRPT data and APT data with geometric distortion correction are sent in the required format.

The processor must meet three requirements for transmission service on a satellite. It has to be able to perform real-time processing; each scanning frame must be continuously transmitted. Since the data is shared around the world, the signal must be in a format that is compatible with all the ground receiving stations around the world. Finally, it must be low power and highly reliable.

2. Signal Reception

The reflective scanning mirror of the radiometer, which has a 45° angle of circumference, brings the radiation from the target into the optical imaging

system, which focuses it onto the detector. It is converted into an electrical signal photoelectrically. The system has a spatial resolution of 1.2×10^{-3} rad. When it scans at a fixed rate of 360 rpm, the IFOV (instantaneous viewing field) corresponds to a target stationary time of

$$\tau_d = \frac{1.2 \times 10^{-3} \text{ rad}}{2\pi} \cdot \frac{1}{6} = 31.83 \mu\text{s};$$

Let the channel amplifier bandwidth be

$$f_H = \frac{1}{2\tau_d} = 15.7 \text{ kHz},$$

Signals are transmitted simultaneously from five channels. In order to eliminate the radiation of the radiometer itself and to avoid dc drift of the circuit, an ac coupled amplification method is used. The radiometer scans the part of the earth that is behind the sun. It takes the cold space as the constant radiation (reflection) baseline prior to scanning the earth. A 3-ms recovery command is generated in cold space which clamps the signal to zero volts. It also establishes a voltage $-V_0$ across the clamping capacitor C. The absolute radiation (reflection) signal of the target is obtained by subtracting this voltage from the analog signal. The clamping voltage is 99.7 percent accurate and the signal from earth is maintained at 99.47 percent accuracy. In order to ensure the accuracy of voltage clamping, after taking the altitude and attitude deviation of the satellite into consideration, the dc recovery command is issued at $1.31\text{--}7.80^\circ$ after phase zero in order to ensure that it ends 2.4° before earth observation begins.

Figure 1 shows the geometry of the scanning radiometer and the all-scenery signals. The altitude of the satellite is $H = 900 \text{ km}$. The radiometer has a 122.4° field angle with respect to the earth.

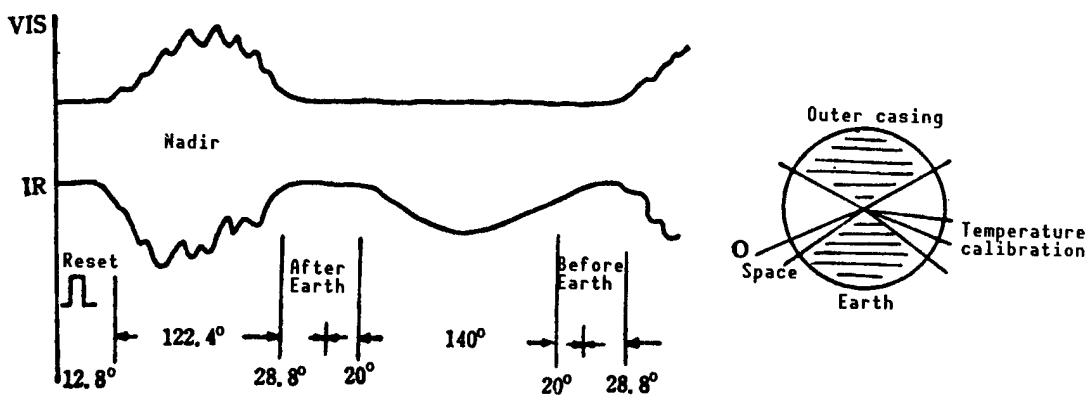


Figure 1. Radiometer Scanning Geometry and All-Scenery Signals

3. Phase Baseline and Sampling Command

The baseline pulse is generated by the magnetic-induction pulse generator on the rotation axis of the scanner. It is processed by a comparator for amplitude discrimination and then by a pulse counter for width discrimination in order to eliminate interference due to external induction. The timing sequence is set to generate a 5- μ s-wide high-accuracy zero-phase baseline pip* [pulse input] at a nadir angle of 74.02°. A five-stage synchronous counter with CP = 199.62 kHz forms a scan timing sequence circuit. The length of the timing sequence is determined by pip*. When the original magnetic pulse flutters beyond the 5- μ s scanning period, the counter automatically resets and pip* is no longer in synchronization in order to maintain the timing stability of the command. Every sampling command is decoder generated.

4. VHRSR/HRPT Processing

4.1 Parallel A/D Technique

After eliminating highly distorted edges, the information gathered within a $\pm 55.4^\circ$ range on each side of the subsatellite point includes 1612 pixels. The sampling frequency is 40 kHz and each channel has 2048 elements. If sampling is transmitted with time-division multiplexing (TDM), and A/D [analog-to-digital] conversion time for each channel is only 5 μ s. Thus, the coding rate would have to be over 2 MHz. Furthermore, if one A/D chip fails, all five channels are out of service. To this end, a five-channel parallel A/D conversion scheme is used (see Figure 2). The CP [clock pulse] comes from an external 500-kHz synchronous clock and the conversion time is 15 μ s. Hence, the coding rate is reduced by a factor of four and the reliability is improved. The converted 8-bit data is sent out in parallel and stored in a latch register [i.e., a flip-flop]. The output is in z mode. Upon the start of the load command, the data transmission generator begins to work. It generates five TDM data-transmission pulses which sequentially act on the output control end of the five-line latch register. The data gathered in sampling period N is entered sequentially from channel 1 to channel 5 into the static RAM (M_1) during sampling period N+1. The data-transmission pulse also serves as the CP for the RAM address counter. In the meantime, A/D conversion proceeds for the (N+1)th time. The data will be sent to M_1 during sampling period N+2. The 10 K memory for the five channels is handled by five 2K x 8 ($M_{1.1} \sim M_{1.5}$) chips and the TDM data is loaded serially.

4.2 Data Rate Conversion, Image Broadening, and Real-Time Write-While-Read Technique

Because the radiometer scans the earth in only one-third of a scanning cycle, data-rate conversion is done by the RAM when it is transmitted so that the length of an HRPT frame is equal to a scanning cycle, in order to lower the requirements on transmission bit rate and carrier bandpass, as well as to facilitate image broadening.

The transmission bit rate is equal to frame length (11090 words) x word length (10 bits) x scanning rate (6/s) = 665.4 kb/s.

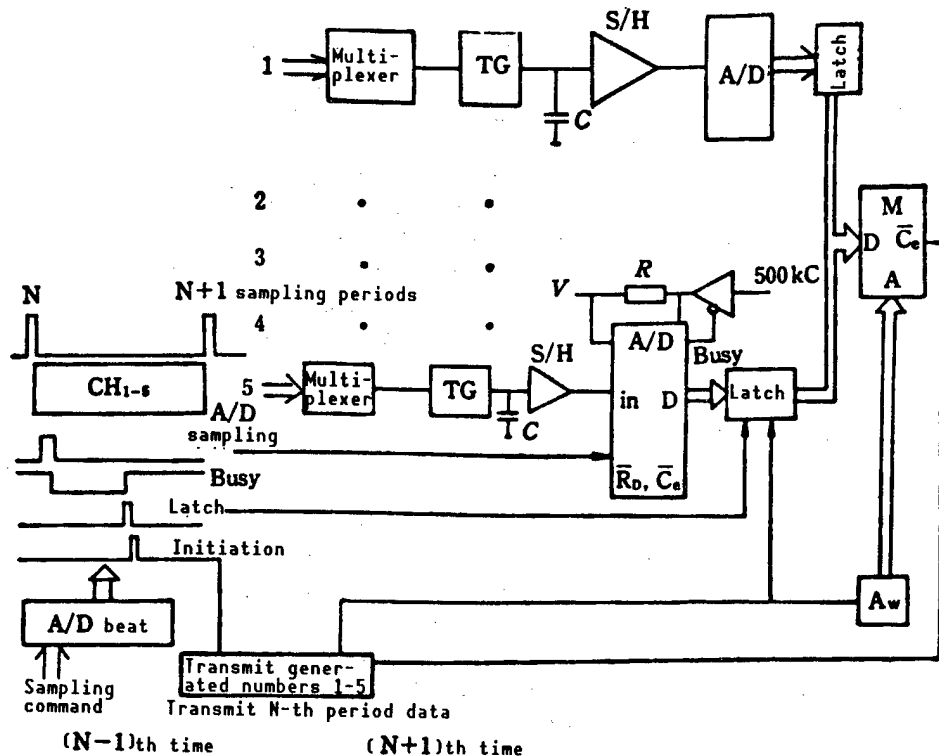


Figure 2. Operation of HRPT-A/D and Its Block Diagram

To establish the HRPT output format, we must first establish the correct read/write versus time relation for the RAM. Starting from zero phase pip*, the system begins to gather earth data at $t_1 = 8.62 \text{ ms}$. After A/D conversion, the data is stored in the RAM under \bar{W}_n control. In principle, after the first 2K memory ($M_{1.1}$) is full (at $t_2 = 10.24 \text{ ms}$), it is switched to read control \bar{R}_n . However, HRPT is programmed to read earth data at the 751st character, i.e., $t_3 = 11.27 \text{ ms}$. Therefore, a start-to-read pulse is generated with a digital time delay τ after the pip* pulse to trigger and synchronize the read-control circuit. This determines the starting point of the HRPT format. The time delay is $\tau = (t_1+t_2)-t_3 = 7.95 \text{ ms}$ (9.5 ms in practice). The read operation speed is 66.54 k words/s, which is three times less than the write speed. When $M_{1.1}$ is reading, earth data is being loaded into $M_{1.2} \sim M_{1.4}$ at the same time. After $M_{1.1}$ is finished reading, the circuit reads $M_{1.2}$ while $M_{1.5}$ is loaded and then continues with reading $M_{1.3}$, etc. As for which one to read, it is determined by $\bar{C}_e = R_n + W_n$. The function of the RAM is determined by R_n/W_n ($n=1 \sim 5$). W_n/R_n is generated by the high-order decoding of the address counter. Access is controlled by the bidirectional data link and the direction of data flow is determined by W/R . Furthermore, since the read speed is different from the write speed, two sets of address counters are installed. The read or write address on the RAM address bus is controlled by the R/W signal. With respect to each RAM, the W/R time does not overlap in order to permit the write-while-read operation. It takes 153.888 ms to read the entire earth data which spans over 332.4°. Thus, data-rate conversion and image broadening can be realized.

In the remaining 12.779 ms, i.e., 27.6°, a total of 11090 words of code for synchronization, telemetry, timing, and attitude parameters are transmitted in real-time without any delay.

After entering the normal phase, the read-contact circuit is separated from the start-to-read pulse. It operates at a constant speed for 11090 words synchronous to the clock. This can eliminate the effect of scanner baseline pulse fluctuation on the output code speed. If the read/write timing is seriously affected by some interference, the read timing-sequence circuit can self-adjust. A negative pulse and read-initiation pulse may be generated between words 00102 and 10991 to be sent together to the AND gate circuit in order to generate another start pulse to enter the correct phase, as shown in Figure 3. The two pulses mentioned above can adjust timing difference within a ±1.5 ms range.

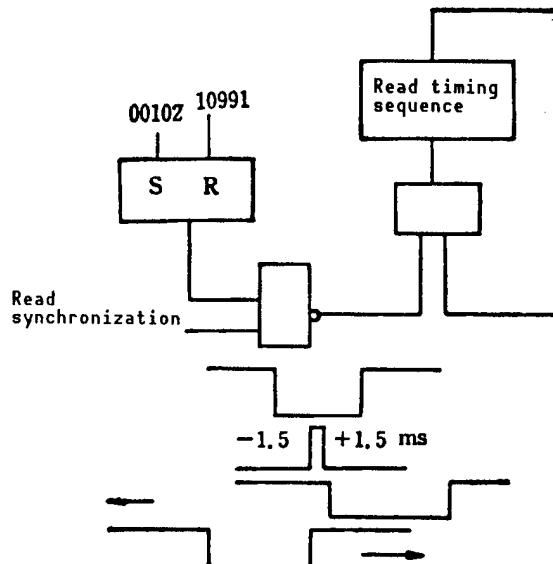


Figure 3. Differentiation and Adjustment of Read Sequence

4.3 Auxiliary Memory M₂ for Target Inversion Data

Based on theory, inversion of target radiation requires the collection of important factors such as the detector temperature and signal and temperature of the reference black body and space, and the incorporation of a 256-step calibrating voltage to verify the linearity of the processor. These data are sent in through a multiplexer, stored in the auxiliary memory M₂ after A/D conversion and transmitted together with the picture data.

The read/write sequence and storage elements of the data gathered above in M₁ and M₂ are shown in Figure 4 and Table 1. The space data obtained on the Nth scan are loaded into cells 41~90. Then, the read control generates an M₂R command to edit the data and then read the calibration data, temperature, reference-black-body signal and then the space data of the (N-1)th scan. It continues to write the calibration, h, and black-body data for the Nth scan. M₂ was designed to be a cyclic address counter up to 90. It is reset to zero

before writing the calibration data. M_1 and M_2 operate independently. An earth sampling command with an extra sampling cycle is used to isolate the data transmission direction after A/D conversion. M_2 is not allowed to change address in the earth zone. The R/W control sequence of M_2 ensures its coordination with the R/W sequence of M_1 . When M_1 reads, M_2 writes, and vice versa, sharing the data bus. The calibration signal is obtained from the 8-stage binary counter driven by the baseline scanning pulse after D/A conversion. The calibrating voltage goes up by one level after each scanning frame. There are 256 levels in all.

Table 1. M_2 Write-Read Sequence

Scan frame	Content	Address	R/M	Time (ms)
N	Space	41~90	W	3.36~3.61
N-1	Calibration	1~5	R	9.698~9.774
N-1	Temperature	6~10	R	9.774~9.849
N-1	Black body	11~40	R	9.849~10.299
N-1	Space	41~90	R	10.299~11.051
N	Calibration	1~5	W	64.60~64.625 ms
N	Temperature	6~10	W	65.80~65.825
N	Black body	11~40	W	117.82~117.970

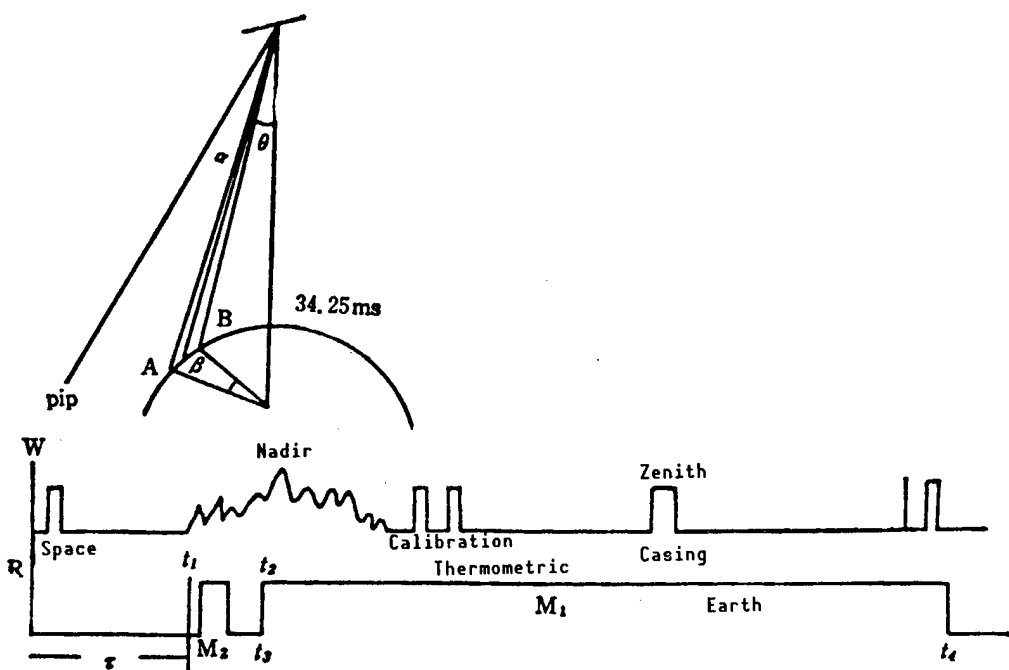


Figure 4. M_1 and M_2 Write-Read Relative Relation in Time

4.4 Formation of HRPT Format

Table 2 shows the HRPT format parameters.

Table 2. HRPT Format Parameters

Frame speed Words/frame Word rate	6 subframes/s 11090 66.54 k words/s	bits per word bit rate code type	10, bit1=MSB, bit10=LSB 665.4 kb/s split-phase code]1, [0
---	---	--	--

The subframe is arranged as follows:

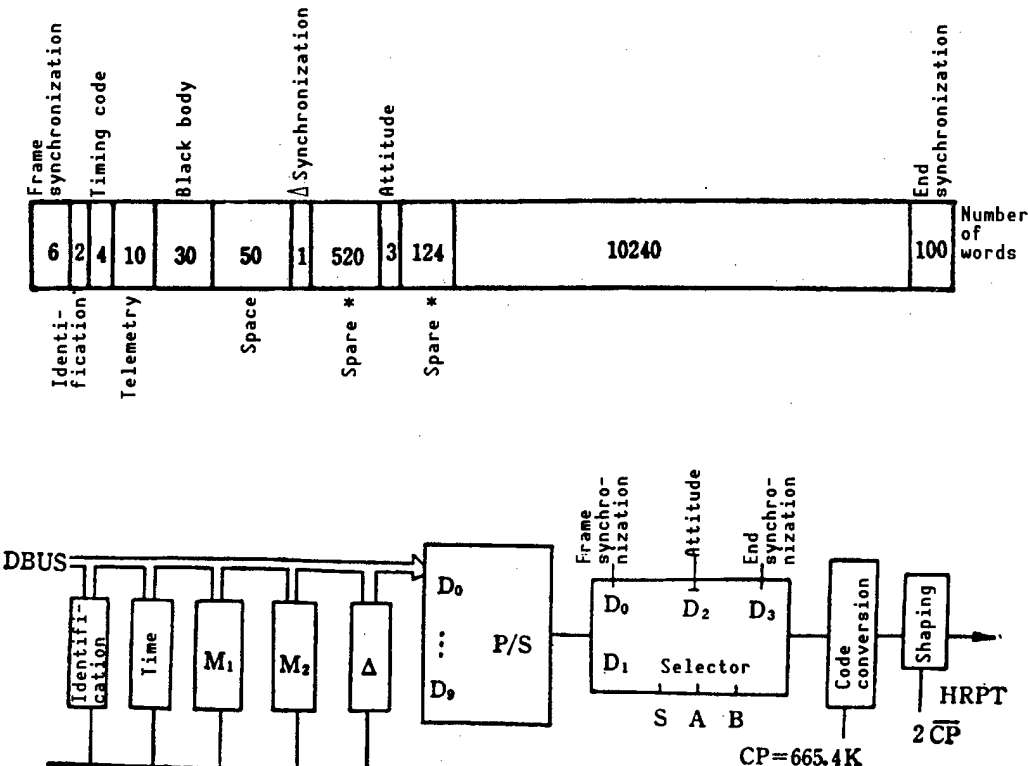


Figure 5. HRPT Frame Format Shape-Taking and Connecting Diagram

Figure 5 shows how all signals in the HRPT format are connected. A 54LS153 multiplexer/selector is used for editing. The read controller is used to generate SAB [select A/B] logic for [data] section.

The 0 frame synchronization at the entrance is done by a six-stage shift register and a serial feedback half-adder. Under the frame synchronization command, the generator is first set all to 1. A cyclic pseudo-random code sequence z^{n-1} ($n=6$) is then generated based on the polynomial $x^6+x^5+x^2+x+1$. The first 60 bits are chosen as the synchronization for each frame of HRPT data.

Entrance 1 transmits data output from the serial/parallel conversion shift register, including earth data, telemetry data, time, identification, black body, space, and Δ synchronization data which are attached to the data bus. Output is done by the read-controller issuing a shift command. When reading M1 and M2, bits 9 and 10 of the data bus are grounded to make up 10 bits. Otherwise, it is in the z mode.

Entrance 2 transmits the attitude code. A request is sent by the radiometer to the satellite signal converter to transmit a 30-bit serial attitude code in real time.

Entrance 3 transmits the end-of-synchronization code. It consists of a 10-stage shift register and a serial feedback half-adder. Upon command, it is set all to 1. A pseudo-random code cyclic sequence 2^{n-1} ($n=10$) is then generated based on the polynomial $x^{10}+x^5+x^2+x+1$. The first 1000 bits are used for code error detection at ground stations and as identification to allow data to be entered in a computer.

Based on the geographic location requirement, a 2^{27} -bits-per-day timing code, accurate to 1 ms, is added. Signals A and B are generated to control entrances C_0-C_3 of 10 "four-to-one" devices. A 10-bit timing value is transmitted via TDM to the DBUS [data bus] as shown in Figure 6. If required, it is zeroed at zero hundred hours GMT by a ground command. The HRPT transmission time is 24.56 ms ahead of the earth signal time in that frame.

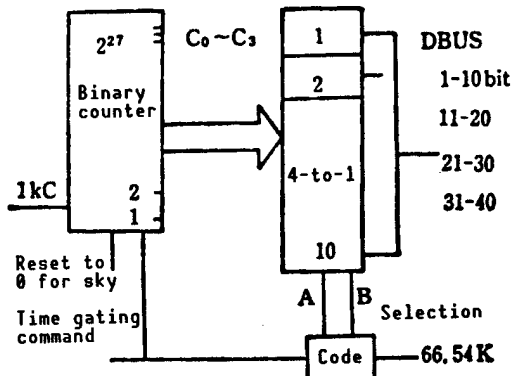


Figure 6. Time Code Editing Diagram

The output from the multiplex/data selector is an NRZ-L [non-return-to-zero L] voltage code. Through the "exclusive NOR" gate $y = \overline{A} \oplus B$, it becomes a split-phase code $B\phi$ -L ($B=665.4$ kC). The 1.3308 MC, which is 90° out of phase with B, is used as the CP. The split-phase code is first reshaped by a D flip-flop and then sent out by a driver.

5. VHRSR/APT Processing

5.1 120 rpm Information

Three frequency divisions of the basic scanning pulse are used for counting to generate three-state subframe pulses to control the time-division switch. Raw scenery data is transmitted by a "three-to-one" TDM method to form a 120-rpm information flow. The decoding circuit outputs the voltage state by remote control. It, in conjunction with the time-division subframe state voltage, controls the transmission switch. The APT channel configuration is shown in Figure 7. It is capable of choosing any two out of five channels. Only channels 1, 2, and 5 are programmed.

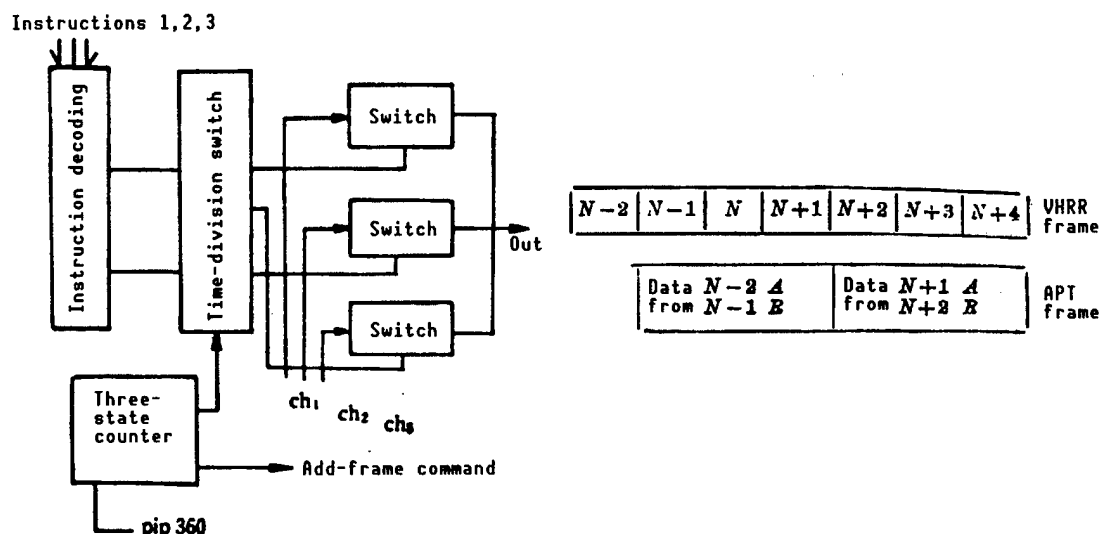


Figure 7. APT Channel Configuration
Selecting Method

Figure 8. Processor Output/Input
Relative Phase

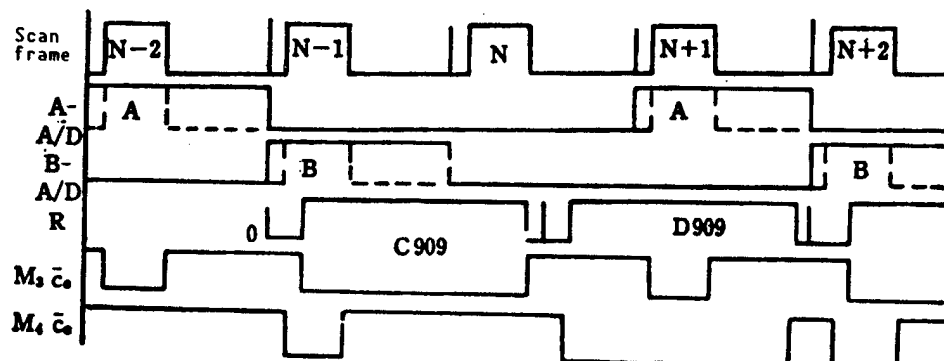


Figure 9. Operating Sequence of Channel A/D-RAM

Figure 8 shows the relative phase between a VHRSR frame and an APT frame. Figure 9 shows the APT processor operating timing sequence.

Channel A earth data gathered during the (N-2)th scan first undergoes A/D conversion and is stored in RAM3. Then, channel B earth data gathered during the (N-1)th scan undergoes A/D conversion and is stored in RAM4. The APT read-control circuit is turned on in synchronization with the (N-1)th scan to read M_3 for 909 words from word 87 according to the preset format. After reading word 1126, it continues to read M_4 for another 909 words. At this time, it is in the (N+1)th scan and channel A data is undergoing A/D conversion and so on. The information in the Nth scan is being omitted. All registers have their own address counters which operate in the read/write period. The address counter rate entrance is controlled by the write command W and read-out command R. A/D data-transmission pulses are used in loading and the read-out rate is at 4160 Hz. Analog cloud picture data is obtained by D/A conversion of the read-out data. The read circuit puts everything together in the preset format (see Figure 10). The state counter sends out weighted functions A, B, and C to control the 8-line switcher 1 in order to transmit via TDM the contents of A, B forecast, space, earth, and telemetry at different times. An 8-line-into-1 four-state signal controls the 8-line switcher 2 to transmit the 32 telemetered parameters one by one.

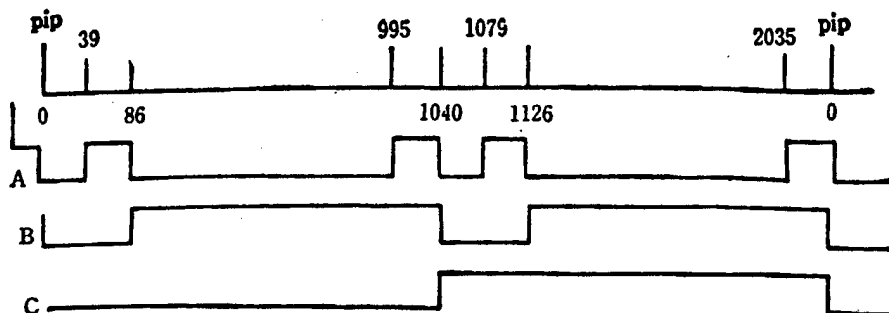


Figure 10. APT Format Shape-Taking Process for Time Sequence

5.2 Geometric Distortion Correction

When the IFOV α scans across the earth at a constant speed, due to the curvature of the earth, the ground resolution (AB) varies with the scanning angle θ per the following formula:

$$AB = R \cdot \frac{\pi}{180} \left\{ \arcsin \left[\frac{H+R}{R} \sin \left(\theta + \frac{\alpha}{2} \right) \right] - \arcsin \left[\frac{H+R}{R} \sin \left(\theta - \frac{\alpha}{2} \right) \right] - \alpha \right\}$$

Hence, there is geometric distortion in the facsimile machine image. The correction involves the use of different ground-resolution-distortion coefficients in different sections depending on the scanning angle over the entire earth field angle of $\pm 55.4^\circ$. A nonlinear sampling method is used to gradually increase the sampling rate in five zones on either side of the nadir. The zoning angle and sampling frequency are balanced by the degree of fluctuation of the ground resolution curve obtained. An entire zone consists of 909 words.

The sampling rate ratio is 4:3:2:1.5:1. The maximum sampling frequency is 40.0 kHz. A/D conversion is in a wait mode and the conversion line is 25 μ s. After data is stored in the RAM, it is read linearly at 4160 Hz to realize a rate change for picture broadening. In addition, correction is also made when a sample element on the time axis is transformed. The result of this correction is shown in Figure 11 on page 88 [see 2nd article in this special issue]. The average resolution of the viewing field is 4.5 km. This method requires a small amount of memory. The picture has the same pixel line density. The picture is uniform and has a mean error of correction of ± 5 percent.

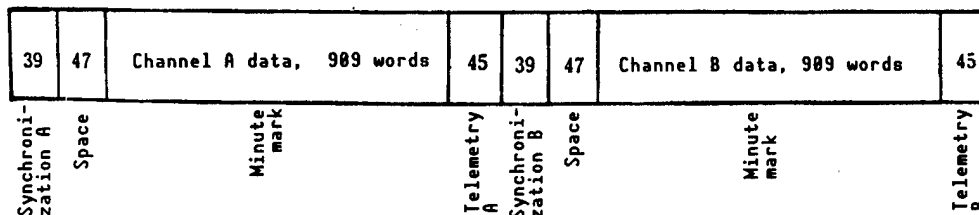
5.3 Shaping of APT Format

The APT format parameters are shown in Table 3.

Table 3. APT Format Parameters

Line speed	2 lines/s	Frame length	128 lines
Frame speed	64 s/frame	Words/line	2080 words
Word speed	4160 Hz	Number of telemetry points	16 for A, B (8 lines/point)

The line format is edited as follows:



5. Results and Applications

The multilevel parallel design improves the reliability of the system. The lower limit of reliability is assessed at $R_L(\text{annual}) = 0.9537$. The processor takes 6.5 W of power. After passing various environmental tests, it has been successfully used on board the FY-1 meteorological satellite.

Acknowledgement

The authors wish to thank all the people in the group for their support. In addition, Ding Daosheng [0002 6670 3932], Li Liangxin [2621 5328 2450], Yang Wu [2799 2976], and Liu Songhe [0491 2646 5440] also contributed to the work.

References

1. NASA-CR-160059.
2. The TIROS-N/NOAAA-G Satellite series, PB-283-859/AS.

Optical Design of Very-High-Resolution Scanning Radiometer

90FE0171E Shanghai HONGWAI YANJIU [CHINESE JOURNAL OF INFRARED RESEARCH] in Chinese Vol 9 No 2, Apr 90 pp 91-98 (Ms received 07 Jun 89)

[Article by Zheng Qinbo [6774 6024 3134] and Xu Xuerong [5171 1331 2837] of Shanghai Institute of Technical Physics, Chinese Academy of Sciences, Shanghai, 200083, China: "Optical Design of Very-High-Resolution Scanning Radiometer On Board FY-1 Meteorological Satellite"]

[Text] Abstract

This paper describes the design of the optical system of the very-high-resolution scanning radiometer (VHRSR) on the FY-1 meteorological satellite, including selection of optical structure, evaluation of image quality, determination of optical bands, regulation of field of view (FOV), and suppression of veiling glare due to stray radiation. Problems associated with machining, installation, and thermal adaptation are also considered. The instrument imaging quality is better than one-tenth IFOV (instantaneous field of view) and the MTF (modulated transfer function) is greater than 0.3 for all channels.

Key words: Scanning radiometer, optical design.

1. Introduction

The scanning radiometer on the FY-1 meteorological satellite is the first photoelectric scanner that is capable of capturing information over a broad band from visible to far-infrared via remote sensing. In order to capture a clear picture of the target on earth, the optical system must have high imaging quality. In order to achieve high sensitivity, the optical system must have high optical efficiency. The authors developed a comprehensive method to design and test the optical system when the scanner was being developed. From the data obtained by the FY-1, the design is feasible. It is also valuable as a reference for the development of other photoelectric scanners for space applications.

2. Optical System Design

2.1 Structure and Requirements of the Optical System

Figure 1 shows the optical configuration of the scanner. Target radiation enters the main optical system, which consists of a main and a secondary lens and is shared by all five channels, from the scan mirror which is at a 45° angle with respect to the optical axis and leaves it in the form of parallel light. The infrared portion is reflected by a visible/infrared splitter and then enters the germanium infrared converging system inside the radiation cooler through a deflecting mirror and a filter. The visible portion of the beam passes through the color splitter and then is split into two parallel beams by a visible/near-infrared splitter. The near infrared is transmitted and focused on the FOV diaphragm and then projected on the silicon single-element detector. The reflected visible light is focused on a three-element detector array by another lens. A set of microcombination optical filters is placed near the detector array to create three independent detection bands.

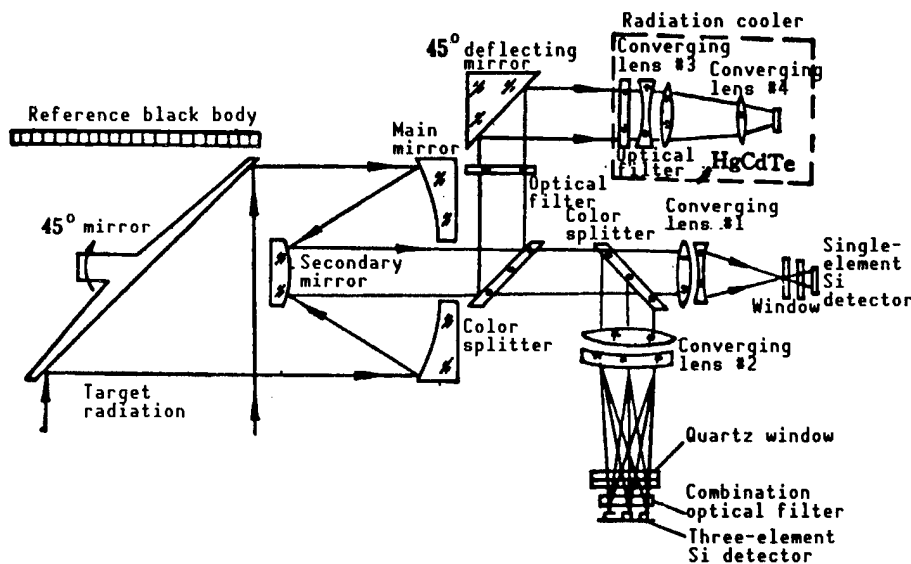


Figure 1. Optical Configuration of 360 rpm Scanning Radiometer

Based on the ground-resolution and detection-sensitivity requirements, as well as on the characteristics of a remote sensing apparatus in space, the optical system must

- 1) receive and converge radiation from a target on earth,
- 2) form the five channels and limit their optical bands by color splitting,
- 3) determine the IFOV simultaneously with the detector and align all relevant FOV,
- 4) have high image quality,

- 5) have high optical efficiency, and
- 6) image quality must not deteriorate after launching and orbiting once it is installed and calibrated.

The design requirements of the optical system are shown in Table 1.

Table 1. Requirements for the Optical Design of VHRSR

Parameter	Channel				
	1	2	3	4	5
Band (μm)	0.58~0.68	0.725~1.10	0.48~0.53	0.53~0.58	10.5~12.5
Center wavelength accuracy	—	—	—	—	—
Wavelength width (μm)	0.58 \pm 0.01 0.68 \pm 0.01	0.725 \pm 0.01 $1.1^{+0.01}_{-0.005}$	0.48 \pm 0.005 0.53 \pm 0.005	0.53 \pm 0.005 0.58 \pm 0.005	10.5 \pm 0.1 $12.5^{+0.1}_{-1.0}$
MTF	>0.85	>0.85	>0.85	>0.85	>0.8
Optical efficiency	0.3	0.3	0.16	0.18	0.18
Aperture (mm)	200				
IFOV (mrad)	$1.2^{+0.1}_{-0}$				
FOV alignment	Ch_1 and $\text{Ch}_2 < 1.10$ IFOV, $\text{Ch}_{1,2}$ and $\text{Ch}_5 < 1/4$ IFOV				
Subsatellite point calibration	Deviation in flight and scan direction < 1/5 IFOV				

2.2 Scan Mirror

The rotation speed of the scan mirror, which is directly driven by a magnetic hysteresis synchronous motor, is 360 rpm. In order to have adequate torque tolerance, the scan mirror is required to have a small rotation inertia, i.e., low mass. The pupil aperture of the main optical system is 200 mm. The scan mirror is an elliptical mirror whose long axis is 290 mm and short is 205 mm. The substrate of this scan mirror is beryllium.

The key to the design of the scan mirror is to prevent distortion. It has a honeycomb structure on the back to reduce mass and increase mirror rigidity.

Advanced surface processing technique is used to meet the high flatness and high reflectance requirements. The scan mirror underwent a number of thermal and mechanical tests. Over a range of 200 mm in diameter, the flatness deviates less than 4 Newton-ring-counts.

2.3 Main Optical System

The main optical system consists of two parabolic mirrors, i.e., the main and secondary mirrors. The effective aperture of the main mirror is 200 mm. It not only is the diaphragm but also serves as the pupil of the system. Its focal length is 200 mm and its F number is 1. The secondary mirror, which is 175 mm away, has an aperture of 25 mm and an F number of 1 as well. This is a coaxial and confocal system. It is a telescope with parallel light in and parallel light out and the magnification factor is 8. The special feature of this kind of telescope structure is that the tertiary aberration coefficient is negligibly small or zero.

$$\begin{aligned}\Sigma S_1 &= \Sigma S_2 = \Sigma S_3 = 0; \\ \Sigma S_4 &= 1.3 \times 10^{-4}; \\ \Sigma S_5 &\approx 0.\end{aligned}$$

This structure can very effectively utilize the main mirror area and the rate of utilization is

$$K = 1 - (D_2/D_1)^2 = 1 - (f'_2/f'_1)^2 = 0.984; \quad (1)$$

Another advantage is that it can be conveniently coupled with the follow-up optical system. With color splitters and filters are inserted in the optical path, the focus is not affected. The focusing lens system to be coupled to it is not limited by distance. Furthermore, the layout is simple.

The parabolic equation for the main mirror is

$$y^2 + z^2 = 800 x; \quad (2)$$

The closest spherical radius is $r = 406.202$ mm and the maximum nonspherical degree is $\delta = 0.049$ mm.

The parabolic equation for the secondary mirror is

$$y^2 + z^2 = 100 x; \quad (3)$$

The closest spherical radius is $r = 50.781$ mm and the maximum nonspherical degree is $\delta = 0.006$ mm. Because the secondary mirror has a very small non-spherical degree, it was polished with the main mirror to correct for the wave aberration introduced as the main mirror was processed to ensure the image quality of the main optical system shared by all five channels.

The material for the main and secondary mirror is quartz and their cases are made of invar which has a very low thermal expansion coefficient. Hence, the

proper axial distance tolerance and radial tolerance, the image quality change due to thermal distortion over a temperature range of $-5\text{--}+45^\circ\text{C}$, can meet the design requirement. In order to effectively suppress glare, a fine texture was machined onto the inside surface and then darkened. In addition, a light shield is placed at the center of the main mirror.

A parabolic surface is ideal for parallel light imaging. Theoretically, a point image is only a diffraction spot. However, due to surface machining error, surface coating thickness error and other errors in assembly, and calibration (i.e., noncoaxial, nonconfocal), the final image is not perfect. The angular dispersion created by the system is equivalent to 1/15 IFOV.

2.4 Visible/Near-Infrared Converging Lenses

(1) Lenses

In order to meet the broad bandwidth requirements and to avoid the deterioration of bonding material in space and humidity effect during ground storage, a set of doubly separated achromatic lenses was chosen. In order to satisfy the requirements for spherical aberration, coma aberration, and location chromatic aberration, the combination uses a positive lens made of BaK₁ barium glass in front of a negative lens made of F₆ flint glass.

The IFOV of the scanner is 1.2 mrad. After passing through the main optical system, it comes out as 9.6 mrad parallel light. Since the linearity of the detector has been determined to be 1 mm, the focal length of the converging lens assembly is

$$f' = 1 \text{ mm}/9.6 \times 10^{-3} = 104.2 \text{ mm}$$

The structural parameters chosen are:

$$\begin{aligned} R_1 &= 46.13, R_2 = -83.95, R_3 = -62.52, R_4 = -539.50; \\ d_{12} &= 12.5, d_{23} = 2.8, d_{34} = 4.0 \end{aligned}$$

Let us use channel 1 as an example, its center wavelength is 0.63 μm . The aberration coefficients are shown in Table 2.

Table 2. Aberration Coefficient of Converging Lens

No of surfaces	Coefficient				
	S ₁	S ₂	S ₃	S ₄	S ₅
1	0.0562309	8.28198E-3	1.21981E-3	2.69534E-5	1.8363E-4
2	0.211179	2.48916E-2	2.93398E-3	1.48107E-5	3.47574E-4
3	-0.276452	-3.31539E-2	-3.97603E-3	-2.2033E-5	-4.79474E-4
4	0.0159667	1.50968E-3	1.42743E-4	2.5533E-6	1.3738E-5
Σ	6.92535E-3	1.52937E-3	3.205E-4	2.22844E-5	6.72952E-5

From Table 2, tertiary aberration values can be calculated as follows:

spherical aberration $L_A' = 0.2412 \text{ mm}$
meridian coma aberration $K_T = 0.01915 \text{ mm}$
astigmatism $\chi_t - \chi_s = 0.02233 \text{ mm}$
(Pitts-fan) surface $\chi_p = 5.165 \times 10^{-3} \text{ mm}$

The actual aberration values were calculated by a computer.

Spherical aberration $L_A'(H) = 0.0628 \text{ mm}$
Meridian coma aberration $K_T(H) = 0.0123 \text{ mm}$

The three-element linear array detector is aligned on the image plane. The three channels in the $0.48\text{--}0.68\text{-}\mu\text{m}$ range have their own optimal image locations. An image location is chosen so that the three channels essentially have the same image quality. In this position, the maximum dispersion spot is 6.5 percent of the sensitive area of the detector.

The near-infrared lens system in channel 2 is the same in structure as that for the three channels discussed above. However, in order to reduce the overall length of the radiometer, the focal length is not good for image quality, it is only for single channel use. The ratio of its dispersion spot at its center wavelength to its FOV diaphragm dimension is only about 3 percent. Therefore, this design is still feasible.

(2) Processing Requirements

The class of the machined spherical mold, i.e., the difference between the actual radius of the machined spherical plate and the designed value, has a direct impact on the performance and parameters of the lens assembly. All the aberration coefficients of the lens assembly are positive and the second surface has the largest contribution. The third surface is an aberration balancing surface and its coefficient is negative. After entering the parameters for the second and third surface into a computer, by comparing to standard levels, it was determined that the plate is class B. Obviously, the class of molds for the first and fourth surface is B or below.

The degree at which the curvature of the lens surface deviates from that of the mold is expressed in terms of Newton rings. The number of Newton-rings reflects rise variation caused by radius difference. Rise is defined as

$$\Delta H = \left| \frac{D^2}{8R_p} - \frac{D^2}{8R_s} \right| = \left| \frac{D^2}{8} \left(\frac{1}{R_p} - \frac{1}{R_s} \right) \right| = \frac{D^2}{8} \cdot \Delta C = \frac{D^2}{8R^2} \Delta R; \quad (4)$$

In equation (4), R_p is the radius of the lens, R_s is the radius of the mold, R is the nominal radius, D is the aperture of the lens and ΔR is the radius difference.

Newton-ring number is defined as

$$N = \Delta H/\lambda/2 \approx 500 \frac{D^2}{R^2} \Delta R, (\lambda = 0.5 \mu\text{m}); \quad (5)$$

Equation (5) shows that the Newton-ring number is dependent on the mold accuracy ΔR . It is impractical to have a requirement for N higher than that for the mold. N is also related to the surface of the lens in the optical system. The choice of N not only must take image quality but also processing time and yield of the lens into consideration.

The irregularity of the Newton rings indicates that the spherical radius is not the same everywhere. This difference causes higher aberration. This irregularity is due to uneven grinding force in the polishing step, or uneven bending, or uneven stress relief inside the lens material, or uneven hardness of the lens material.

The lens surface polishing requirement is determined by the role of the lens in the optical system and the glare requirement of the system. The eccentricity of each single lens and axial offset of the lens system are determined by the effect of dispersion spot on the overall image quality.

2.5 Far-Infrared Converging Lens System

(1) Lens System Design

The far-infrared is an important band for a meteorological satellite. It not only provides thermal pictures of the earth's surface and ground target temperature but also can operate around-the-clock to observe the earth twice a day.

The converging lens system is located inside the radiation cooler. It is optically coupled with the main optical system of the scanner in the form of parallel light. The converging system of this channel is limited by several factors, such as small detector size, low temperature environment, highest optical efficiency possible, and limited available lens materials. In particular, a flat window sealed detector must have a longer rear intercept which makes it more difficult to design.

We chose single-crystal germanium as the infrared lens material. With an anti-reflective coating, it has a high optical efficiency at $10.5\text{-}12.5 \mu\text{m}$. The lens system includes a doubly separated assembly, a negative lens in front of a positive lens, but initial convergence. The point image is then reduced by a meniscus lens on the sensitive surface of a HgCdTe detector.

Since the detector size is 0.21 mm and the incident parallel light is 9.6 mrad, the effective focal length of this converging system is

$$f'_s = 0.21/9.6 \times 10^{-3} = 173.86 \text{ mm},$$

i.e., the F number is 0.87.

The converging lens system thus designed has a dispersion spot approximately one-third the size of the detector. Hence, the far-infrared channel has a MTF > 0.96 at a spatial frequency of 417 c/rad.

After assembly, the MTF curve of the converging lens system was measured with a Traple-2000 instrument. When $f = 417$ c/rad, MTF > 0.9.

(2) Thermal Design of Infrared Lens System

To suppress glare in the infrared is an important subject for a lens system used to capture earth data. Using a cold optical system and low specific radiance case is somewhat effective.

The infrared converging lens material is germanium and its case is made of stainless steel. Stainless steel was chosen because the temperature difference from one end to the other is quite large and thermal conduction of this heat to the secondary cooling block near the meniscus lens should be avoided so as not to increase the load of the radiation cooler. In addition to selecting a suitable material, a thin-wall structure is adopted to increase thermal resistance.

The converging lens operates over a wide range of low temperatures. Therefore, compared to room temperature, the index of refraction, radius of curvature, and thickness of germanium will vary. Consequently, the focal length and near intercept of the lens system will also vary. If proper measures are not taken, defocusing caused by a change in the rear intercept will significantly lower the MTF of the system and produces a blurred image.

2.6 Determination of the Spectral Response Band

In order to determine the spectral response of the VHRSR, it is necessary to consider the effect of every element which has its own unique spectral characteristics. These elements include mirror coatings, color/beam splitters, and filters. Since the spectral characteristics of these elements affect the spectral response band of the system, and the absolute response of these elements has an impact on the signal-to-noise ratio (SNR) of the instrument, both spectral response and sensitivity therefore must be taken into account together.

Determination of spectral response of a specific band is very important for its detector. Except for band-pass filters, other elements have little effect on the relative spectral response of the system. Design requirements for technical specifications of filters, such as bandwidth, secondary peak response and transmissivity, should be set after the steepness requirements for the leading and trailing cutoff edge are known based on a thorough understanding of the wideband spectral response curves of the detectors and splitters.

In order to obtain the spectral response for channel 5, two filters, a short-wave cutoff filter, and a long-wave cutoff filter have been designed. If the long-wave limit of the HgCdTe detector is less than $12.5 \mu\text{m}$, the long-wave cutoff filter is not used. Thus, the sensitivity of the system can be improved.

Channel 2 uses a color glass to cut off short wavelengths. The long-wave cutoff limit of the silicon detector serves as a long-wave cutoff to obtain a response band at $0.725\text{--}1.1 \mu\text{m}$.

Channels 1, 3, and 4 have very strict requirements for bandwidth and center wavelength. Furthermore, the filter is in front of the three-element silicon detector. Therefore, a micro-combination filter was specially designed and developed and placed near the focal plane.

3. Testing of Primary Performance Characteristics and Results

3.1 Spectral Response and MTF

Figure 2 shows the spectral response curves for the five channels of the VHRSR.

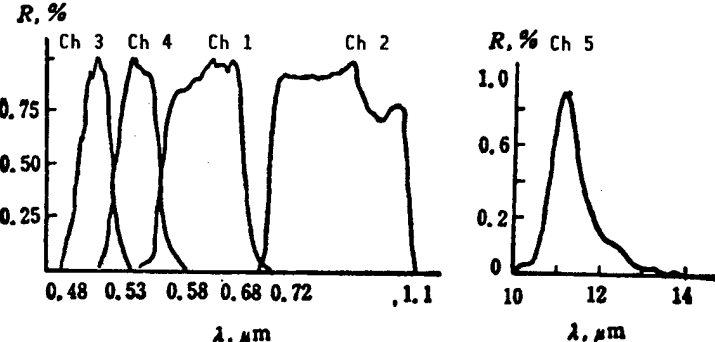


Figure 2. Relative Spectral Response Curves of VHRSR

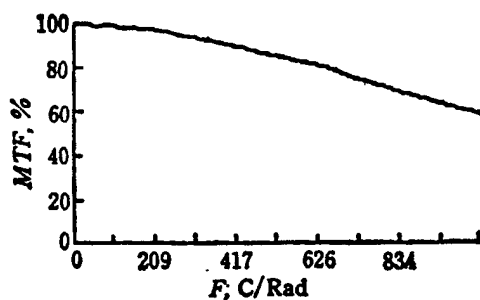


Figure 3. MTF of Converging Thermal Infrared Lens System

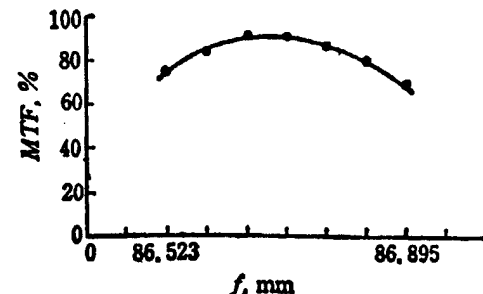


Figure 4. MTF of Off-Focus Converging Thermal Infrared Lens System

OTF [optical transfer function] and MTF tests were done individually for the visible/near-infrared converging lens system and the far-infrared converging lens system. Figures 3 and 4 are the OTF curve and off/focus MTF curve for the thermal infrared lens system, respectively.

The scanner consists of an optical system, detectors, and an electronic system. Radiation from the target is converted into an electric signal and transmitted to earth through these three independent systems. Because the overall MTF is the product of the MTF of the three systems, it is necessary to test the MTF of the entire instrument in order to determine the ground

resolution of the scanning radiometer. Test results showed that at a spatial frequency of 417 c/rad, MTF is greater than 0.3.

3.2 Effect of Main Optical Axis on FOV Alignment and Instrument Installation

When testing the MTF of the overall instrument, because of using the same spatial-frequency radiation source, electrical signals were obtained simultaneously from channels 1, 2, and 5. Based on the lead or lag of the electrical signal shown on an oscilloscope, it is possible to determine FOV alignment.

A collimated light source is used to check whether the X, Y plane (scanning direction and flight direction) of installation is parallel to the optical axis in order to obtain subsatellite-point calibration data.

Table 3 lists the primary optical performance data of the VHRSR.

Table 3. Primary Performance Optical Data of VHRSR

Parameter	Channel				
	1	2	3	4	5
Spectral band (μm)	0.5742~ 0.6872	0.7191~ 1.03	0.4355~ 0.5290	0.5287~ 0.5858	10.575~ 12.15
MTFs (417 c/rad)	>0.5	>0.5	>0.3	>0.3	>0.3
FOV alignment			CH ₁ , CH ₂ , CH ₅ < 1/8 IFOV		
Sub-satellite point standard ("")		Scanning direction 0		Flight direction 14	

3.4 Orbiting Experiment

After the launch, sharp earth pictures were received all over the world. Experts analyzed pictures of the same target from all five channels. Comparing to the target, it was found that the resolution of the scanner is 1.1 km (satellite at 900 km altitude). The quality of design, installation, and calibration work has been proven to withstand the dynamic conditions of launching and the space environment in orbit.

Acknowledgement

The successful development of this optical system is a result of cooperation of people in various departments at this institute's plant, including optical coating, optical calibration, and spectral measurement. We wish to express our gratitude for their assistance and support.

References

1. AVHRR Final Report, N81-1239.
2. The TIROS/N/NOAA A-G, Satellite series, N84-31784.
3. Characteristics of the Landsat Sensor's Spatial Responses, N84-31784.
4. Lloyd, J.M., "Thermal Imaging System," translated by the Infrared and Laser Technology Editing Group, 1978, pp 140-152.
5. Zheng Qinbo, Zhan Lishan [6124 7787 1194], and Xu Xuerong, HONGWAI YANJIU [CHINESE JOURNAL OF INFRARED RESEARCH], Vol 1 No 3, 1982, pp 179-184.
6. Zheng Qinbo, Ibid., Vol 3 No 1, 1984, pp 69-70.

Satellite-Borne High-Accuracy Scanner

90FE0171F Shanghai HONGWAI YANJIU [CHINESE JOURNAL OF INFRARED RESEARCH] in Chinese Vol 9 No 2, Apr 90 pp 108-114 (Ms received 13 Jun 89)

[Article by Zhang Baolong [1728 1405 7893] and Guo Huilin [6753 1920 2651] of Shanghai Institute of Technical Physics, Chinese Academy of Sciences, Shanghai, 200083, China: "Satellite-Borne High-Accuracy Scanner"]

[Text] Abstract

This paper describes the operating principle, design, basic structure, and space-flight results of a satellite-borne high-accuracy scanner.

Key words: Rotating speed stability, bearing lubrication, beryllium scan mirror.

1. Introduction

The scanner is an important component at a remote sensing system. The quality and reliability of the scanner can directly affect the useful life and picture quality of the remote sensing system. Thus, it is critical to the success of the remote sensing system. In order to allow the remote sensing system on the FY-1 meteorological satellite to operate normally, we developed a high-accuracy satellite borne scanner.

During the development stage, we solved problems such as long-term lubrication of bearing in an ultrahigh vacuum, fabrication of large-aperture beryllium-based scan mirrors, dynamic balance of irregularly-shaped large-aperture scan mirrors, and high-accuracy rotating speed stability control, and successfully conducted a test in orbit.

2. Operating Principle and Environment

The scanner is installed in a satellite remote sensing system. The 45° axis of rotation coincides with the direction of flight. When the scan mirror rotates, the remote sensor scans perpendicular to the direction of flight at a fixed optical IFOV (instantaneous field of view) to receive the radiation emitted or reflected from the earth or the atmosphere. While the satellite orbits around the earth, two-dimensional pictures of the atmosphere, land, and ocean are

obtained. At the same time, the scanner sends a baseline pulse of a specific amplitude through its magnetic head to the electronic part of the remote sensing system to serve as a starting pulse for the control logic and timing circuit of the electronics.

The scanner operates in cold space at approximately 4 K—this is a high vacuum and weightless environment with space particle radiation. The scanner must withstand vibration, impact, and centrifugal force during launch. The harsh environment, high reliability, high accuracy, and long operating life requirements, and low power and lightweight specifications make the development work very difficult.

3. Structural and Technical Characteristics

The main scanner structure includes a high-accuracy motor drive, a drive power supply, bearings and lubricating parts, a scan mirror and dynamic balancing mechanism, and a basic pulse generator. The external appearance of the scanner is shown in Figure g of the color picture pages in this issue [see special color insert].

The main technical parameters of the scanner are shown in Table 1.

Table 1. Main Technical Parameters of the Scanner

Parameter	Value
Voltage of power supply (V)	27 ± 10%
Input power (W)	≤ 10
Synchronous torque (g·cm)	>250
Rotating speed (rpm)	360
Rotational moment of inertia (g·cm ²)	55000-63000
Rotating speed stability	1 × 10 ⁻⁴
Basic pulse output amplitude (V)	2 ± 0.3
Operating temperature (°C)	-5 ~ +45
Life (h)	>8760

3.1 High-Accuracy Motor Drive and Its Power Supply

A satellite remote sensing system captures earth scenery and pictures and the imagery is sent to the ground stations. In order to make sure that the image is not skewed or shaky, it is necessary to rigorously control the long-term and instantaneous stability of the motor drive.

(1) Drive Motor

In a low-speed situation where the stability requirement is high, in order to improve life and reliability, simplify the drive mechanism, and solve problems associated with machining, assembling, and lubricating gears, one needs a low-speed magnetic hysteresis synchronous motor to drive the scanner directly.

The rotating speed of the motor is determined by the following equation.

$$n = \frac{60f}{P}; \quad (1)$$

In equation (1), f is the frequency and P is the number of pairs of poles.

The drive motor is a magnetic hysteresis synchronous motor with 30 pairs of poles. When passing a 180-Hz ac current with a 90° phase difference through the motor, a rotating magnetic field is generated to drive the rotor at 360 rpm. The long-term stability of the motor is determined by the power source. Since a quartz-crystal oscillation frequency-division power source is used, a stability of as high as 1×10^{-6} can be achieved. When a magnetic hysteresis motor operates in a synchronous mode, it has the same angular characteristics as other ordinary synchronous motors. The larger the number of pairs of poles P is, the higher the instantaneous stability of the rotating speed becomes. The scanner motor has 30 pairs of poles. As long as it meets rigorous assembly requirements, high instantaneous stability of the motor can also be satisfied.

The magnetic hysteresis motor can start asynchronously and then work synchronously. The starting torque is larger than that in synchronous operation which ensures that the scanner can start reliably and meets the power requirement. The characteristics of the motor are shown in Figure 1.

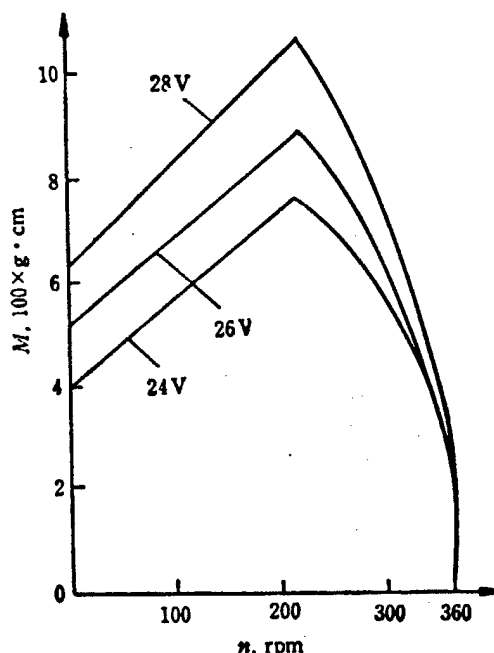


Figure 1. Typical Performance Curves for the Scanner Motor

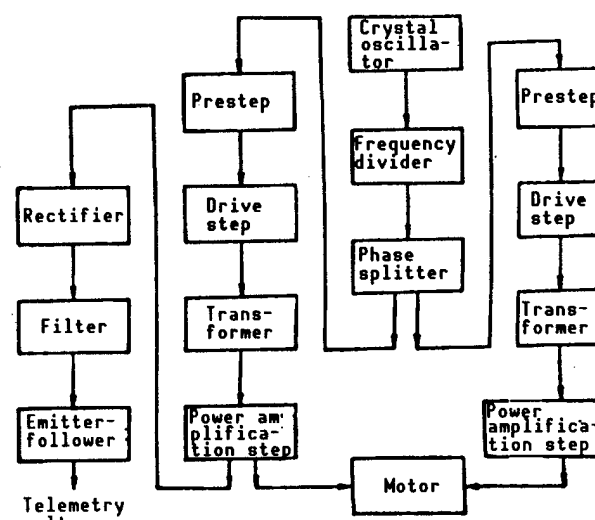


Figure 2. Block Diagram of Circuits

(2) Driving Circuit

Figure 2 shows a block diagram for the driving circuit.

The motor drive signal frequency is transmitted by a quartz oscillator. The signal goes through a frequency divider and a digital phase splitter in order to send two 180-Hz electrical signals 90° apart in phase angle to the pre-stage. They are then transmitted to the driving stage. After coupling with a transformer to supply the power-amplification stage, the motor rotates at a steady speed. Because of coupling to a transformer, not only common ground interference of the power source is avoided but also the speed of the motor is not affected by voltage fluctuation. In order to prevent voltage fluctuation in the common power supply onboard, an LC [inductor-capacitor] suppression filter circuit is added to the power supply. In order to monitor the voltage, a telemetry circuit is also incorporated in the system.

3.2 Bearings and Bearing Lubrication Under Ultrahigh Vacuum

Bearings are important parts in a drive mechanism. The motor shaft is supported by a pair of DB bearings. Based on requirements such as long life, high accuracy, and low frictional torque, high-quality ball bearings are used. Bearing parts of the same high quality were made with a specific amount of preload.

(1) Preloading the Bearings

In order to eliminate potential axial gap in a ball bearing, a preloading method was used during assembly. A predetermined amount of axial load is applied on the bearing as shown in Figure 3. Prior to preloading, there is a gap between the inner ring and the jacket. After the load is applied, the gap disappears. Applying a preload to the bearing can provide more accurate radial and axial location and can also raise the rigidity of the assembly.

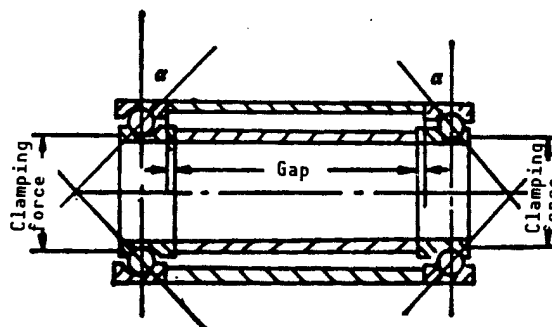


Figure 3. Preloading Bearing

The amount of load must fall within a suitable range. If it is too low, balls will slide to affect the stability of the rotating speed. A high preload will affect the life of the bearing. In order to maintain the load essentially constant within the operating temperature range to improve stability, materials for the bearing, jacket, main shaft, and base were chosen to have similar linear expansion coefficients.

(2) Bearing Lubrication in Ultrahigh Vacuum

The scanner operates in an earth orbit 900 km in space. The environment is an ultrahigh vacuum ($1.33 \times 10^{-8} \text{--} 10^{-9} \text{ Pa}$). An ultrahigh vacuum has a significant impact on lubrication and friction. Ordinary lubricating oil or grease used on earth vaporizes very rapidly in space. Because the scanner is exposed in space, cosmic radiation will degrade certain lubricants as well. Several processes have been studied and a comparison is shown below (see Table 2).

Table 2. Comparison of Different Lubricating Processes

Lubricating method	Friction moment	Life	Operating accuracy
Solid film	High and fluctuating	Short	Poor
Grease film	Somewhat high	Unstable	Medium
Oil film	Low	Long	High

We used a special low-volatility lubricating oil, which passed the radiation test, to lubricate the bearing of the scanner. The bearing holder is made of a porous material and the lubricating oil is soaked into the holder in vacuum. Moreover, an oil container is installed between the two bearings. When the oil in the bearing gradually wears thin with time, the holder and the oil container will continuously replenish it to the balls. This method can ensure the long-term stable operation of the scanner in space.

(a) Lubricating State of Bearing

The lubricating state inside a bearing is determined by the oil film which plays an important role in lengthening the useful life of the bearing.

The formation of an oil film is dependent upon factors such as oil viscosity, amount, rotating speed, temperature, surface tension, load, and cleanliness of the surface of the rolling track of the bearing. In a ball bearing, the contact between a steel ball and the ring is a point contact. Thickness of the oil film h is determined by the following equation.

$$h = 2.04\phi^{0.74}(\alpha\eta_0 u)^{0.74}R^{0.407}\left(\frac{E'}{Q}\right)^{0.074} \quad (2)$$

In equation (2), ϕ is a correction factor, α is the viscous pressure coefficient, η_0 is the viscosity, u is the mean speed, R is the equivalent radius of curvature, E' is the equivalent elastic modulus, and Q is the load on the rolling body.

Based on EHD theory, when $\lambda > 4$, the bearing is well lubricated.

$$\lambda = \frac{h}{\sqrt{\sigma_1^2 + \sigma_2^2}}; \quad (3)$$

In equation (3), h is the thickness of the oil film, and σ_1 and σ_2 are the roughnesses of the two surfaces.

Results showed that the bearing is operating in a well-lubricated state.

(b) Calculation of Escaped Lubricating Oil in Space

When the scanner operates in space, oil vapor continuously escapes into space. In order to confine the oil vapor, the outlet of the main shaft was designed like a maze to make it more difficult to escape.

An equation can be derived to estimate the amount of oil vapor escaped in space:

The conductance of a circularly-shaped round pipe u_1 is

$$u_1 = 3.81 \sqrt{\frac{T}{\mu}} \frac{(d_1 - d_2)^2 (d_1 + d_2)}{\ell} K_h, \quad (4)$$

The conductance of a rectangularly-shaped short tube u_2 is

$$u_2 = 3.628 ab \sqrt{\frac{T}{\mu}} K_3, \quad (5)$$

The total conductance in series u is

$$\frac{1}{u} = \frac{1}{u_1} + \frac{1}{u_2} + \dots + \frac{1}{u_n}, \quad (6)$$

The amount of gas passing across this specific cross section in unit time Q is

$$Q = u (P_1 - P_2) \quad (7)$$

The amount of gas passing across this cross section in the lifetime G is

$$G = Qt, \quad (8)$$

The mass of gas escaped from the main shaft during the lifetime of the bearing M is

$$M = \frac{\mu G}{RT}. \quad (9)$$

where T is the temperature, μ is the gram molecular weight of the gas, R is the gas constant, and P_1 and P_2 are the pressure differentials.

Based on the above equations, after plugging in various relevant parameters, the result is as follows:

At the outlet of the maze, a total of 0.48 mg of lubricating oil will escape into outer space in 1 year. Thus, the escape of oil vapor will not affect the life of the scanner.

(c) Technical Considerations for Bearing Lubrication

The cleanliness of the bearing assembly environment is an important subject. Scanner bearing was assembled in an ultraclean environment.

In order to achieve certain rotating speed stability, the amount of oil initially placed in a bearing must be rigorously controlled.

In order to let the scanner bearing run over a long time, it is important to wet the surface of the track. Because it is not easy to wet the surface of a new bearing with oil, it is hard to form a film. This effect goes away after certain measures are taken.

All parts of the scanner are assembled in the atmosphere on earth. In space, gases inside the scanner will escape. In order to avoid the impact of discharged gases on bearing lubrication, a hole was opened at the rear of the scanner to allow gases to escape.

3.3 Scan Mirror and Dynamic Balance Mechanism

The effective optical aperture of the remote sensing system on the FY-1 meteorological satellite is 200 mm. Its elliptical 45° scan mirror has a 205-mm short axis and a 290-mm long axis.

(1) Basic Structure of the Scan Mirror and Its Materials

It was required that the scanner drive consumes less than 10 W of power. The rotating part, consisting of a scan mirror, rotor, and dynamic balance mechanism, has a moment of inertia of 55000–63000 gcm². Thus, the mirror must be lightweight. The scan mirror is an optical component which is involved in the image-forming process; its flatness and cleanliness requirements are very high. In addition, its optical quality must remain essentially unchanged after enduring the mechanical environment during launch and over a long period of time in space.

Based on the requirements mentioned above, the front face of the scan mirror was designed as an optical surface. In order to reduce weight and maintain rigidity, the back was designed to have a honeycomb structure. The back side was gold plated for better temperature control during rotation in the cold space environment. After considering environmental, power, and optical requirements, beryllium was chosen as the substrate for the scan mirror because of its low density, high elastic modulus, high specific modulus, low thermal distortion, and good thermal dimensional stability. It is an ideal material for a scan mirror used in space.

Although beryllium has these unique characteristics, it is poisonous and difficult to machine. Beryllium has a low coefficient of elongation. Stress

from machining can very easily crack its surface. A special machining technique was used to ensure the dimensional stability of the beryllium mirror.

Figure g on the color insert page in this issue shows the appearance of this scan mirror [see special color section].

(2) Dynamic Balance of the Scan Mirror

The shape of the scan mirror is somewhat complicated. It is relatively large in size and is installed on the main shaft at a 45° tilt angle. It generates a large couple of force due to imbalance during rotation. It cannot operate without a dynamic balance mechanism. There is no way to keep the rotation speed highly stable without making a dynamic balance correction.

In order to obtain balance, it is necessary to satisfy the following conditions:

$$\begin{cases} x_0 = 0, z_c = 0; \\ \sum_{i=1}^n M_i = 0; \end{cases} \quad \begin{matrix} (10) \\ (11) \end{matrix}$$

$x_c = 0$ and $z_c = 0$ are conditions for static balance.

In the OXYZ coordinate system, the 45° scan mirror is symmetric with respect to the YOZ plane. Therefore, the coordinate of center of mass in the x direction is zero. Hence, the coordinate of center of mass in the z direction must also be zero from the static balance requirement.

$$z_c = \frac{1}{m_{tot}} \sum_{i=1}^n m_i z_i. \quad (12)$$

Since the mirror is irregularly shaped, for convenience, it was divided into 38 pieces in our computation. The mass and center of mass for each piece were calculated first before the statically balanced overall mass and center of mass were calculated for the design of the mirror.

In addition to satisfying the static balance requirement, the sum of the moment of force around a reference point A must be zero during rotation for dynamic balance.

$$\sum_{i=1}^n M_i = 0; \quad (13)$$

In equation (13), $M_i = F_i Y_i$ represents moment of force A. $F_i = m_i z_i w^2$ represents centrifugal force along the z direction, w is the angular speed, Y_i is the center of mass coordinate along Y with respect to point A.

Since it is symmetric with respect to x , the centrifugal force in the x direction cancels out.

Although the 45° scan mirror is statically balanced, it is not dynamically balanced because $Y_{up} \neq Y_{down}$. To this end, we need a counter force couple. Figure 4 shows a diagram of a dynamically balanced scan mirror.

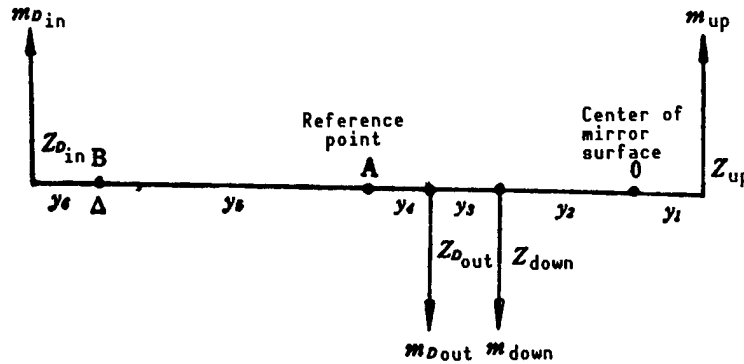


Figure 4. Schematic Diagram of Dynamically Balanced Scan Mirror

Let's assume that it is a rigid axis. With respect to point A, we have

$$\sum_{i=1}^n m_{up\ i} Z_{up\ i} Y_{up\ i} + \sum_{i=1}^n m_{dn\ i} Z_{dn\ i} Y_{dn\ i} \\ + \sum_{i=1}^n m_{D_{out}\ i} Z_{D_{out}\ i} Y_{D_{out}\ i} + \sum_{i=1}^n m_{D_{in}\ i} Z_{D_{in}\ i} Y_{D_{in}\ i} \quad (14)$$

Inner and outer dynamic balance blocks were designed based on the result of the above equation to realize the dynamic balance of the 45° scan mirror.

Due to machining error and uneven density distribution in materials, the dynamic balance of the scanner needs to be calibrated after assembly.

3.4 Baseline Pulse Generator

The baseline pulse generator provides a starting pulse for the control logic and timing circuitry of the remote sensing system. It consists of a magnetic head and a trigger. The head is installed on the base of the scanner and the trigger plate is on the rotating dynamic balance block.

When the rotating trigger plate passes the magnetic head, because the magnetic line of force is cut by the trigger plate, an electric pulse is generated. The voltage of the pulse is determined by the following equation.

$$V = -\frac{d\phi}{dt}; \quad (15)$$

In equation (15), V is the induced potential, ϕ is the magnetic flux, and t is time.

When the magnetic flux varies with time, the induced potential is proportional to the speed. At constant speed, the voltage is determined by the gap between the trigger plate and the magnetic head.

4. Experiments and Results

The scanner passed various environmental tests for astronautical products and was put to work in an ultrahigh vacuum continuously for 1 year. In addition, the scanner also passed a series of tests as a part of the entire satellite. Experimental results show that the scanner is stable and reliable. It permits the FY-1 meteorological satellite to bring us clear cloud pictures.

References

1. NASA-CR-156682.
2. Edited by Vacuum Design Handbook Group, "Vacuum Design Handbook," Vol 1, Beijing: National Defense Industry Publishing House, 1979, pp 54-72.

Three-Element Linear Silicon Detector

90FE0171G Shanghai HONGWAI YANJIU [CHINESE JOURNAL OF INFRARED RESEARCH] in Chinese Vol 9 No 2, Apr 90 pp 115-121 (Ms received 11 Jul 89)

[Article by Liang Pingzhi [2733 1627 3112], Zhang Zhongtang [1728 1813 1016], Sun Deqing [1327 1795 1987], and Tan Deming [6151 1795 2494] of Shanghai Institute of Technical Physics, Chinese Academy of Sciences, Shanghai, 200083, China: "Three-Element Linear Silicon Detector for FY-1 Meteorological Satellite"]

[Text] Abstract

Based on requirements for spectral response, dark current and junction capacitance, the parameters associated with the Si material and its processing are determined. In order to improve reliability and prevent light crosstalk, measures such as rounding off the corners of the sensing element, adding protective aluminum rings and shields, and heavy phosphorous doping are discussed. The responsivity of the developed device at 632.8 nm is 0.3 A/W [amps/watt]. At -10 V and 25°C, the dark current is 5×10^{-11} A and the junction capacitance is 29 pF [picofarads]. The device passed a rigorous aging screening and various environmental tests. Therefore, it is suitable for use in outer space.

Key words: Linear silicon detector, quantum efficiency, spectral distribution of responsivity.

1. Introduction

The three-element linear silicon detector is composed of three PN junctions on an Si substrate. The three PN junctions serve as three sensing elements. Their area is $1 \times 1 \text{ mm}^2$ each and their centers are 1.57 mm apart. The three elements receive visible signals at 0.48~0.53, 0.53~0.58, and 0.58~0.68 μm , respectively. The three bands are created by placing a micro combination band-pass optical filter in front of the sensing surface.

This paper describes the design principle of this device. It starts from its high-performance and high-reliability requirements and involves the selection of parameters of Si, determination of SiO_2 thickness and the device structure. It also describes the fabrication processes and specifications of the device.

2. Design

2.1 Selection of Si Material and Processing Parameters

As far as a photovoltaic Si detector is concerned, its spectral response curve (spectral distribution of quantum efficiency), junction capacitance, and dark current are essentially determined by the parameters associated with the Si substrate. When a detector needs to be designed based on the requirements for a scanner, parameters associated with Si, such as resistivity and life, must first be determined.

In order to maximize the quantum efficiency η in the operating band (0.43~0.68 μm), it is necessary to reduce the surface recombination rate, decrease junction depth x_j , and increase electron and hole diffusion length L_n and L_p . The effect of substrate carrier density N_d on η is not significant.¹ Therefore, the selection of substrate resistivity has a great deal of impact on raising η . Nevertheless, because $L_p = \sqrt{D_p \tau_p}$, where D_p is the hole diffusion coefficient and τ_p is hole life, a high-resistivity material often has a larger τ_p . Hence, the selection of a high-resistivity material also helps make η larger.

Next, let us consider the resistivity requirement based on dark current I_d and junction capacitance C_j . At room temperature, the dark current I_d is mainly generated by the depletion zone and its magnitude is proportional to the width of the depletion zone W .² However, the junction capacitance C_j is inversely proportional to W .

The N_d vs. I_d/A_j and N_d vs. C_j/A_j curves for a single-side step junction are shown in Figure 1, where A_j is the junction area and different I_d curves correspond to different lifetimes τ_0 . From Figure 1, the carrier concentration of the substrate, and consequently its resistivity, can be determined based on the values of C_j and I_d required by the scanner.

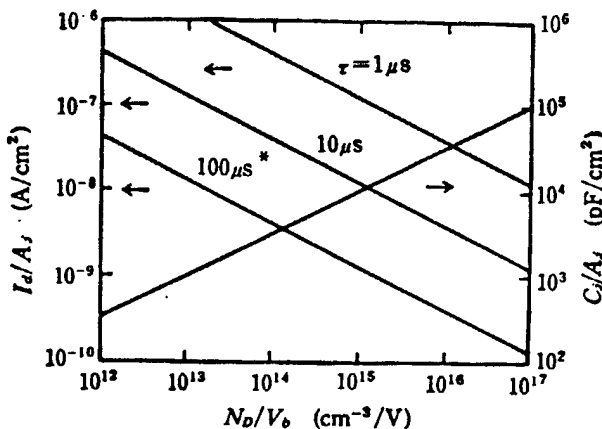


Figure 1. Dark Current and Junction Capacitance Vs. Substrate Impurity Concentration and Bias Voltage

In addition to resistivity, we must determine parameters associated with the life of the material. We are looking for the longest life possible. Therefore, this material should always be the highest grade attainable by the manufacturing plant.

We also determined certain principles associated with the selection of processing parameters. For example, in order to raise the quantum efficiency in the visible region, the junction should be as shallow as possible. The impurity concentration in the P⁺ zone should not be too high. Otherwise, N_A goes up and L_n goes down. Care must be taken to lower the energy of the interface between SiO₂ and P⁺ to reduce the surface recombination rate. Based on these principles, a process was developed to fabricate devices of high quantum efficiency.

2.2 Determination of SiO₂ Layer Thickness

For passivation, a layer of SiO₂ is thermally formed on the sensing surface. Due to interference, the thickness of this layer will significantly affect the quantum efficiency of the device.¹ Figure 2 shows the curve for SiO₂ thickness d_{ox} versus transmissivity T_λ. The thickness of SiO₂ was chosen to maximize T_λ at the given wavelength. The total quantum efficiency η_{total} is a product of internal quantum efficiency and T_λ. Therefore, η_{total} is also enhanced.

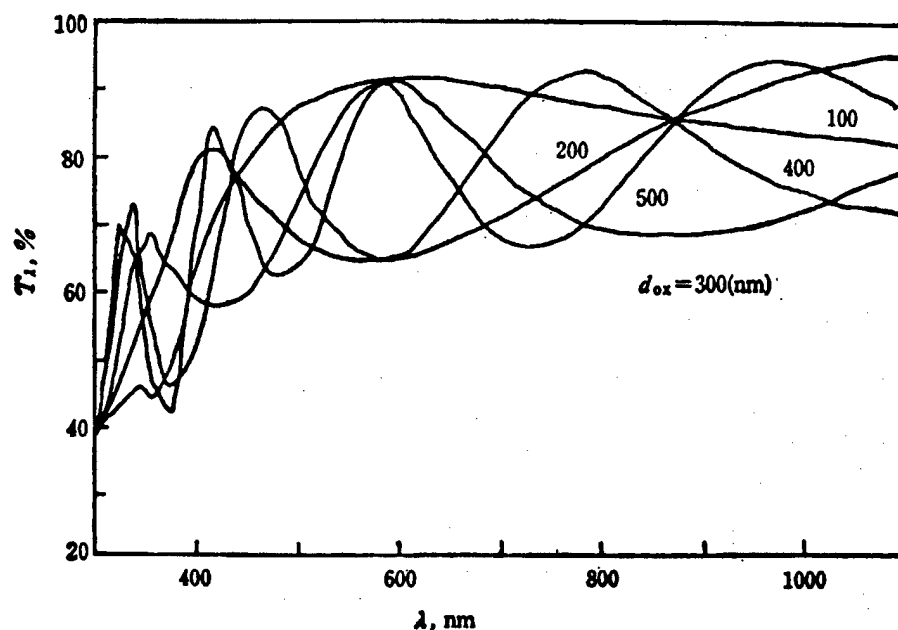


Figure 2. Transmissivity of SiO₂ Layer on Si Substrate Vs. Wavelength

2.3 Structure

The structural layout of the device is shown in Figure 3.

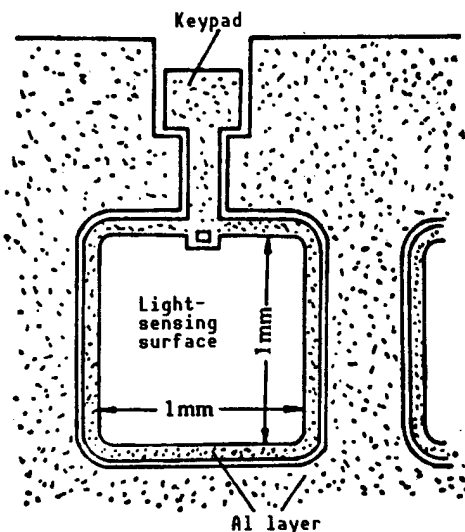


Figure 3. Layout of Sensing Element

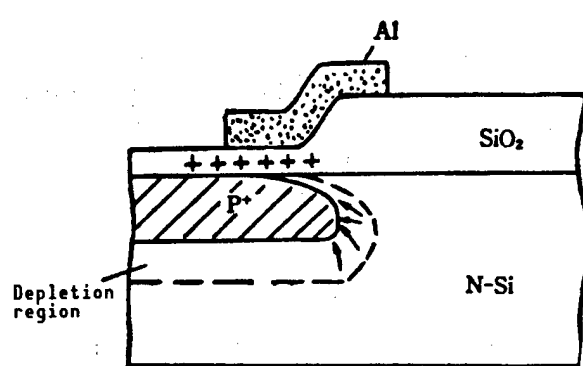


Figure 4. Influence of Cations in SiO_2 on Leakage Current in a P^+N Junction

There are several special features:

(1) Rounding Off Corners of Sensing Element

The corners of the boron diffusion window of the sensing element are rounded off in order to avoid the formation of spherical junctions at sharp corners due to charge accumulation. Hence, the breakdown voltage of the junction is increased.

(2) Adding Protective Aluminum Ring

Experimentally, it was found that mobile cations (primarily Na^+) exist in the SiO_2 layer during processing. During electrical burn-in, because a negative bias is applied to the P zone, cations will accumulate at the interface between the SiO_2 layer and P zone.

At the boundary of the P^+N junction near SiO_2 , because the impurity concentration is lower in the P^+ zone, a type reversal may occur due to these cations. Thus, the boundary of zone P^+ is bent (as shown in Figure 4). As a result, the electric field of the depletion region is locally concentrated. This effect would cause the P^+N junction leakage current to go up and its breakdown voltage to go down.³ In order to avoid this effect, an aluminum guard ring is added to the boundary of the P^+N junction and this ring is connected to the pad coming out of the P^+ zone. Thus, when a negative bias is impressed onto zone P^+ , the aluminum ring is also negatively biased. The P^+N junction boundary no longer has an electric field that attracts cations in SiO_2 and the above phenomenon is no longer a problem.

However, the overall capacitance of the device is increased with the addition of the aluminum guard ring.

(3) Preventing Sensing Element Enlargement and Optical Crosstalk

In N-type Si substrate with $\rho = 20\text{--}40 \Omega\text{cm}$, the minority carrier diffusion length is $160\text{--}200 \mu\text{m}$. Therefore, carriers generated by light in the substrate can contribute to the photocurrent if they are generated within a diffusion length away from the boundary of the depletion region of the PN junction. This enlarges the sensing surface. An aluminum film is used to shield the area surrounding each sensing element. However, there are still two factors which cause optical crosstalk. One is that the aluminum shield and the aluminum guard ring must be insulated. Therefore, there is a gap between them and light-induced carriers will be generated in this gap. These carriers will diffuse away. When they enter the depletion region of a neighboring sensing element, there is optical crosstalk. In order to prevent the diffusion of these light-induced carriers, heavy phosphorous doping, up to 10^{20}cm^{-3} , is used around each sensing element. Since the diffusion length of light-included carriers in an area heavily doped with phosphorus is reduced to approximately $25 \mu\text{m}$, optical crosstalk is effectively prevented.

3. Device Fabrication Process

Figure 5 shows the device fabrication process.

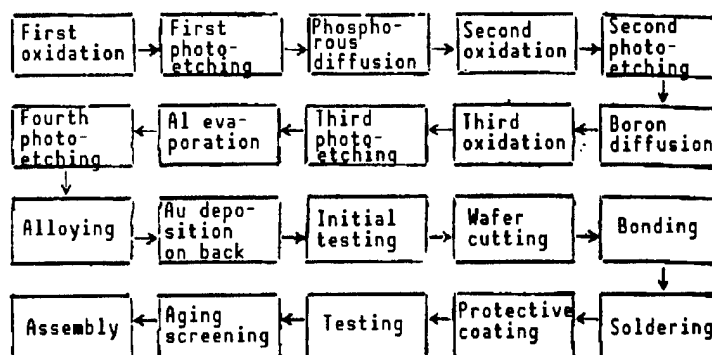


Figure 5. Device Fabrication Process

4. Device Characteristics

4.1 Responsivity

There are two ways to test the resistivity of the device. One is to use a standard 285.6 K (room-temperature) lamp as the light source to measure the integrated resistivity and the other is to use a 632.8 nm He-Ne laser, or a white lamp with a narrow-band filter, as the light source to measure the monochromatic resistivity of the device. Typically, with a 100 lx light source, the integrated resistivity is $1.2 \times 10^{-6}\text{A}$. At 632.8 nm, the monochromatic resistivity is 0.3 A/W.

4.2 Dark Current

An HP [Hewlett-Packard] 4140 BPA was used to measure the dependence of dark current upon temperature. At 25°C and -10 V bias, the typical dark current is $1\text{--}5 \times 10^{-11}\text{A}$. Figure 6 shows the dark current versus temperature curve. It reveals that dark current is primarily due to generated current at below 100°C. The contribution of diffusion current becomes larger at above 100°C.

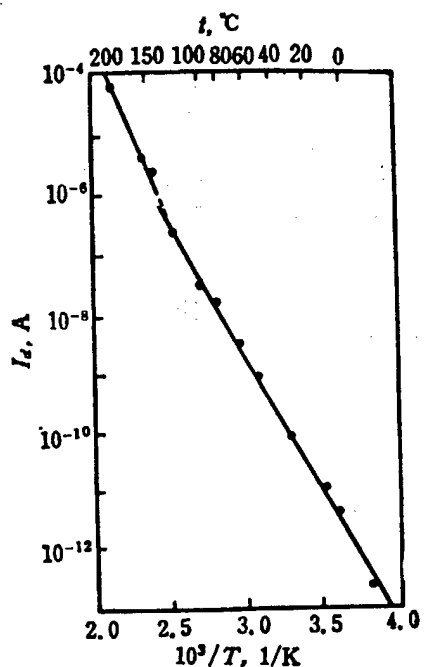


Figure 6. Dark Current Vs. Temperature

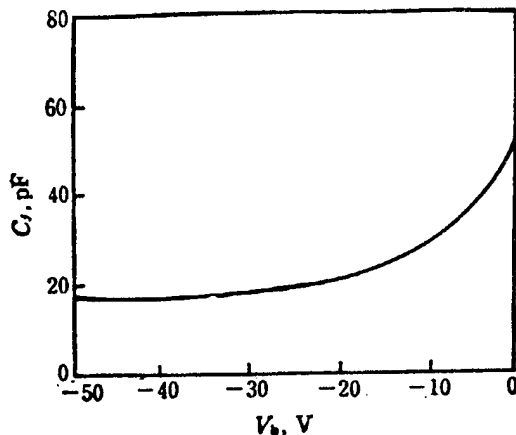


Figure 7. Device Capacitance Vs. Bias

4.3 Capacitance

Capacitance was measured with a Model CTG high-frequency C-V [capacitance-voltage] characteristics device. The test frequency is 1 MHz. Figure 7 shows a typical C-V curve. At -10 V, the capacitance is approximately 30 pF.

4.4 Spectral Distribution of Responsivity

An automatic spectrometer was used to determine the distribution of resistivity of the device and the typical result is shown in Figure 8. It shows that the resistivity of the device shifts toward shorter wavelength.

4.5 Optical Crosstalk

A small light spot (approximately 30 μm in diameter), with wavelength at 632.8 nm, was used to scan across the device. The output signals from two neighboring sensing elements A and B were simultaneously recorded. A typical result is shown in Figure 9. It shows that when light is shining at the gap between the aluminum screen and aluminum guard ring, there is a signal. It also shows that

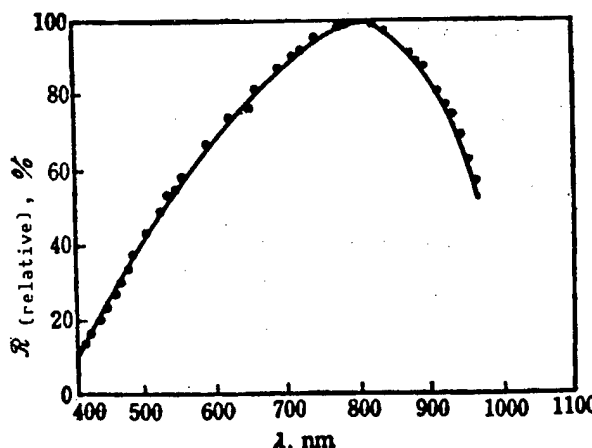


Figure 8. Spectral Distribution of Responsivity of the Device

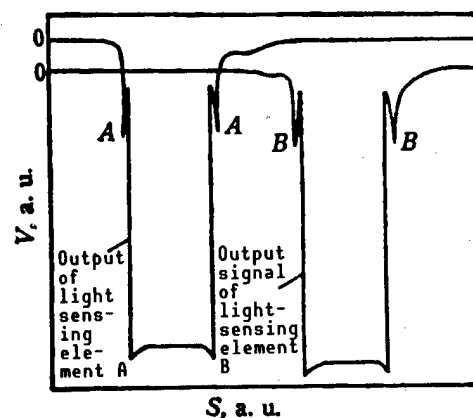


Figure 9. Crosstalk Between Two Adjacent Sensing Elements

when the light shines on sensing element A, sensing element B has no signal output within its sensitivity range and vice versa. Therefore, it can be concluded that the optical crosstalk is below 1 percent.

4.6 Noise Current Spectrum

An HP3585 frequency analyzer was used to measure the noise-current spectrum of the device. Figure 10 shows the typical result. Below 30 Hz, it is $1/f$ noise. From 30 Hz to 1 kHz, it is shot noise. At higher frequencies, there is dielectric noise.

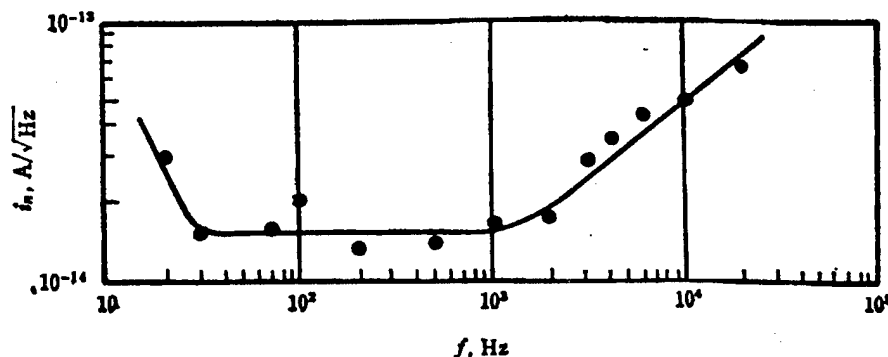


Figure 10. Noise Spectrum of the Device

All the characteristics measured above can meet design specifications (see Table 1).

In order to meet requirements for space applications, the device must be rigorously screened by aging and environmental tests, including vibration, impact, centrifugal force, vacuum temperature cycling, humidity and high-energy particle irradiation. Our experience shows that any device that passes the aging screening test can satisfy all environmental tests.

Table 1. Comparison of Design Requirements and Measured Values

Parameter	System design requirements	Measured values
Responsivity (A/W)	0.15(0.48~0.53 μm) 0.25(0.53~0.58 μm) 0.30(0.58~0.68 μm)	0.15 0.25 0.30
Dark current A (-10 V, 25°C)	2.5×10^{-8}	$1\sim 5 \times 10^{-11}$
Junction capacitance (pF) (-10 V, 25°C)	<35	29
Reverse Breakdown voltage (V)	> 40	60~100

5. Conclusion

(1) A method has been established to choose the parameters regarding the silicon material and the process based on requirements such as spectral distribution of resistivity, dark current, and junction capacitance. The three-element linear silicon sensor developed by this approach has satisfied the requirements for the scanner well.

(2) Structurally, measures such as rounding off the corners of the sensing elements and adding aluminum guard rings have significantly improved the reliability of the device.

(3) The aluminum screen and heavy phosphorous doping have effectively stopped the enlargement of the sensing area and lowered optical crosstalk to below 1 percent.

(4) Typical values of the device are as follows: resistivity is 0.3 A/W at 632.8 nm; at 25°C and -10 V, dark current is 5×10^{-11} A, junction capacitance is 29 pF and reverse breakdown voltage is greater than 60 V. These parameters have exceeded scanner specifications. The device has passed a very rigorous aging screening process and various environmental tests. Therefore, it is suitable for use in space.

Acknowledgement

The authors wish to thank Dong Jianmin [5516 0256 3046], et al., of the Silicon Processing Group and Dong Liangchu [5516 0081 0427], et al., of the Testing Group in the 6th Laboratory of the CAS's Shanghai Institute of Technical Physics for their involvement in the development of this device.

References

1. Jespers, P.G., et al., "Solid State Imaging," Noordhoff International Publishing, No 47, 1976, p 29.
2. Sze, S.M., "Physics of Semiconductor Devices," A Wiley-Interscience Publication, 1981, p84.
3. Fitzgerald, D.J. and Grove, A.S., "Physics of Failure in Electronics," Vol 4, Rome Air Development Center, 1966, p 315.

Onboard Long-Wave HgCdTe Detector

90FE0171H Shanghai HONGWAI YANJIU [CHINESE JOURNAL OF INFRARED RESEARCH] in Chinese Vol 9 No 2, Apr 90 pp 123-128 (Ms received 20 Jul 89)

[Article by Fang Jiaxiong [2455 1367 3574], Xu Guosen [1776 0948 2773], and Zhang Linfa [1728 2651 3127] of Shanghai Institute of Technical Physics, Chinese Academy of Sciences, Shanghai, 2000083, China: "Onboard Long-Wave HgCdTe Detector"]

[Text] Abstract

This paper reports the performance of a long-wave HgCdTe detector for satellite use. The concept of band detectivity $D_{\Delta\lambda}^*$ is used to represent the performance of the detector at 105 K and at an operating band of 10.5~12.5 μm . The value of $D_{\Delta\lambda}^*$ is in the range of $1\sim3 \times 10^{10}\text{cmHz}^{1/2}\text{W}^{-1}$. Reliability test results show that the failure rate of the detector is less than 2.5×10^{-5} .

Key words: HgCdTe, infrared detector, satellite.

1. Introduction

The infrared scanner on the FY-1 meteorological satellite employs a scheme involving a HgCdTe detector and a radiation cooler. It is associated with a series of stringent requirements for the HgCdTe detector. We studied the effect on the performance of the device with rising temperature up to 105 K and its ability to operate in space. Because the energy gap of HgCdTe increases with temperature, its intrinsic carrier concentration, carrier mobility and life, and surface recombination rate also vary with temperature. Consequently, the performance of the detector also varies with the operating temperature. We investigated the temperature dependence of these parameters. In addition, we are introducing a new optimal parameter, i.e., using band detectivity to express the performance of a HgCdTe detector at 105 K for a given band of 10.5~12.5 μm . Results of a large number of passivation and reliability tests indicate that the HgCdTe developed for space use has excellent behavior and high stability and reliability.

2. Theoretical Analysis of Detector Behavior

Let us discuss the mechanism for a HgCdTe detector operating at 77 K based on intrinsic excitation of carriers. For N-type HgCdTe, detector responsivity, detectability, and noise can be expressed as follows:

$$R_{\lambda P} = \frac{\Delta V_s}{P_s} = \frac{\eta \lambda V_0 \tau}{h c n_0 L w d}; \quad (1)$$

$$D_{\Delta \lambda}^* = \frac{\eta \lambda}{2 h c} \sqrt{\frac{\tau}{P_0 d}} = \frac{\eta \lambda}{2 h c} \sqrt{\frac{2 \tau_{Ai}}{dn_0}}; \quad (2)$$

$$V_{g-r} = \frac{2 V_0}{(L w d)^{1/2}} \left[\frac{P_0 \tau \Delta f}{n_0^2} \right]^{1/2}; \quad (3)$$

In equations (1)-(3), incident power $P_s = \phi_s h \nu L w$; where L and w are the length and width of the detector, respectively, and d is its thickness; V_0 is the detector bias; η is its quantum efficiency; n_0 is the carrier concentration; τ is its effective lifetime; τ_{Ai} is the Auger lifetime; h is Planck's constant; c is the speed of light; and λ is the wavelength of the response. In order to have high resistivity and detectivity, carrier concentration must be as low as possible and carrier lifetime must be as long as possible. In addition, the detector should be as thin as possible and quantum efficiency should be as high as possible.

Despite the fact that the 8-14 μm HgCdTe detector operating at 77 K has a very high detectivity, it is still very difficult to reach 77 K in space applications. Therefore, it is very important to develop a high-detectivity infrared detector which operates at approximately 105 K in a band between 8-12 μm . The detectivity of an 8-12 μm HgCdTe detector at 105 K, whose parameters are selected based on existing experimental data and information, is calculated in the following.

2.1 Selection of Composition χ

Because of the high temperature dependence of the energy gap of HgCdTe, the material composition χ must be determined after the spectral band and operating temperature are known. The HgCdTe detector is designed to work at approximately 105 K. Based on the energy gap E_g , composition χ and temperature T , the following relation between cutoff wavelength λ_c and temperature is obtained¹:

$$E_g(\chi, T) (\text{eV}) = -0.25 + 1.59\chi + 5.233 \times 10^{-4}(1-2.08\chi)T + 0.32T\chi^3; \quad (4)$$

Equation (4) is applicable over the range $0.17 \leq \chi \leq 0.6$, and $20 \text{ K} \leq T \leq 300 \text{ K}$. Equation (4) can be used to calculate the relation between energy gap and temperature for various materials with $\chi = 0.19-0.205$. After this, taking $\lambda_c = 1.24/E_g$ (eV), one can derive the relation between λ_c is approximately 12.5 μm , the composition of the material is chosen to be $\chi = 0.195-0.198$.

2.2 Carrier Concentration

Empirically, intrinsic carrier concentration can be expressed as follows¹:

$$n_i = (1.093 - 0.296\chi + 4.42 \times 10^{-4}T) \times 4.293 \times 10 E_g^{3/4} \cdot T^{3/2} \exp\left(-\frac{E_g}{2KT}\right); \quad (5)$$

From equation (5), the intrinsic carrier concentration n_i can be calculated as a function of temperature and composition χ . In reality, the n_0 of the HgCdTe material is one order of magnitude higher than that of n_i at 77 K.

2.3 Carrier Lifetime

It is more difficult to estimate carrier lifetime. Lifetime measurements made using materials with $\chi = 0.205$ and 0.195 indicate that it is essentially limited to collision recombination in better materials. Therefore, lifetime can be expressed as a function of temperature and energy gap:

$$\tau_{Ai} = A \frac{1}{KT} \left(\frac{E_g}{KT}\right)^{1/2} \exp\left(\frac{E_g}{KT}\right); \quad (6)$$

where $A = 3.46 \times 10^{-13}$ is a constant independent of the composition and temperature.

2.4 Computation of Detectivity and Responsivity

With n_i and τ_{Ai} , we can estimate the peak detectivity and resistivity. Let us assume that the carrier concentration at 77 K is $n_0 = 7.0 \times 10^{14} \text{ cm}^{-3}$ and the applied bias is $V_0 = 0.25$ V. Let us also assume that surface recombination rate is independent of temperature. Based on equations (1) and (2), it is possible to derive the curves for D_{Ap}^* vs. temperature and R_{Ap} vs. temperature (see Figures 1 and 2).

From Figures 1 and 2, the detectivity and resistivity at 105 K are 30~50 percent lower than the detectivity and resistivity at 77 K. An 8~12- μm HgCdTe photoconductivity sensor can achieve a high detectivity at 105 K.

3. Experimental

Single-crystal HgCdTe was grown from melt. The crystal was thermally treated at a low temperature and then carefully trimmed using a special technique to minimize damage to yield thin light-sensing elements. In addition, the crystal's effective response time was measured by a photoconductivity decay method. It was found that the normal surface recombination rate S is less than 1000 cm/s and might be as low as 100 cm/s.²

The resistivity, noise, detectivity, and spectral distribution were determined using conventional techniques. The black-body source used is the FY-100 standard black body developed in-house. Its effective emissivity is 0.99 and the temperature-control accuracy is 500 ± 0.1 K.

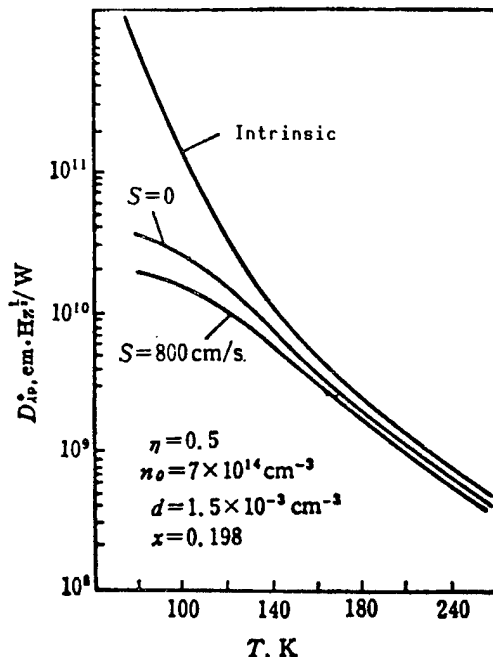


Figure 1. Theoretical Spectral Detectivity Vs. Temperature Curve

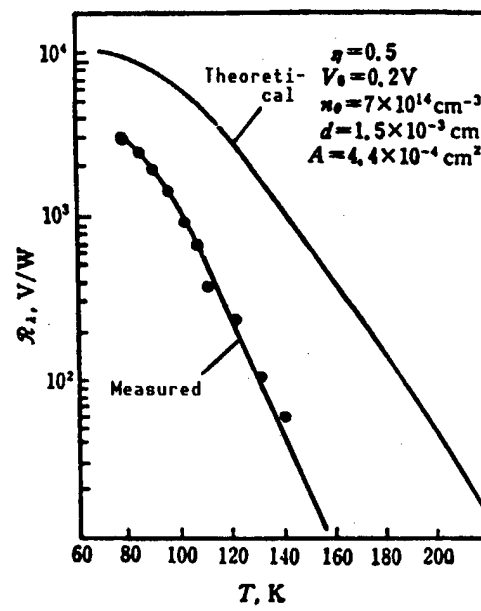


Figure 2. Theoretical Responsivity Vs. Temperature Curve

4. Detector Characteristics

4.1 Band Detectivity

As far as the FY-1 meteorological satellite is concerned, the mean detectivity in a specific band ($10.5\text{--}12.5\text{ }\mu\text{m}$) is a direct parameter which represents its optimal performance. Monochromatic detectivity does reflect the capability of the detector. To this end, $D_{\Delta\lambda}^*$ is defined as an integral optimal factor within the band $\Delta\lambda = 10.5\text{--}12.5\text{ }\mu\text{m}$. $D_{\Delta\lambda}^*$ is also known as spectral band detectivity,³ and is given by:

$$D_{\Delta\lambda}^* = \int_{10.5}^{12.5} P_b(\lambda) D_{\lambda}^* d\lambda / \int_{10.5}^{12.5} P_b(\lambda) d\lambda;$$

where $P_b(\lambda)$ is the monochromatic radiation intensity of the 500 K black body.

From black-body detectivity D_{bb}^* and the spectrum one, can obtain the spectral detectivity D_{λ}^* and then calculate band detectivity $D_{\Delta\lambda}^*$.

Table 1 shows the characteristics of some typical devices at 105 K. Table 2 is the band detectivity $D_{\Delta\lambda}^*$ at 105 K. From Tables 1 and 2, we can see that peak detectivity $D_{\Delta p}^*$ within the band of interest cannot reflect the performance of a detector. Instead, spectral band detectivity $D_{\Delta\lambda}^*$ can truly represent the performance of a detector.

Table 1. Characteristics of HgCdTe Detector at 105 K (FOV 60°)

Device No	I (mA)	D_{AP}^* (cmHz $^{1/2}$ /W)	R (V/W)	λ_c (μm)	τ (Ω)	A (cm^2)	P _D (mW)
E018	2.5	1.5×10^{10}	3.5×10^3	12.8	42	4.4×10^4	0.3
E020	5.0	1.4×10^{10}	5.2×10^3	13.2	51	4.4×10^4	1.3
8285	9	5.0×10^{10}	3.8×10^4	11.7	46	13×10^4	3.7
8628	12	4.0×10^{10}	1.4×10^4	12.3	20	4.4×10^4	2.9
8617	8	1.6×10^{10}	1.1×10^4	11.9	46	4.4×10^4	2.9
8621	5	2.4×10^{10}	1.7×10^4	13.6	38	4.4×10^4	1.0
8638	10	4.1×10^{10}	1.8×10^4	13.9	23	4.4×10^4	2.3
8629	12	3.8×10^{10}	1.6×10^4	11.8	23	4.4×10^4	3.3

Table 2. Spectral Band Detectivity D_{AP}^* of Detectors at 105 K

Device No	8285	8628	8617	8621	8638	8629
Bias current (mA)	9	12	8	5	10	12
D_{AP}^* (cmHz $^{1/2}$ /W)	2.9×10^{10}	2.9×10^{10}	1.1×10^{10}	1.9×10^{10}	2.8×10^{10}	2.2×10^{10}

4.2 Detector Signal Vs. Bias Current

From equation (1), in order to have a high resistivity we have to increase the bias V_0 . However, when minority carrier life is long, it is limited by the sweep-out effect. When minority carrier life is short ($\tau < 5 \times 10^{-7}\text{s}$), it is limited by Joule heat V_0^2/τ .

Figure 3 shows the bias characteristics of the detector. The optimal bias current is near 3 mA. It is related to the material and structure of the sensing chip. The bonding between the sensing chip and its substrate was studied to ensure that the signal is not affected by Joule heat.

4.3 Frequency Spectra of Noise

At above 300 Hz, the noise spectrum of an N-type HgCdTe photoconductivity device primarily contains generated-recombination noise:

$$V_{gr} = 2V_0(P_0 I \Delta f / wd)^{1/2} / n$$

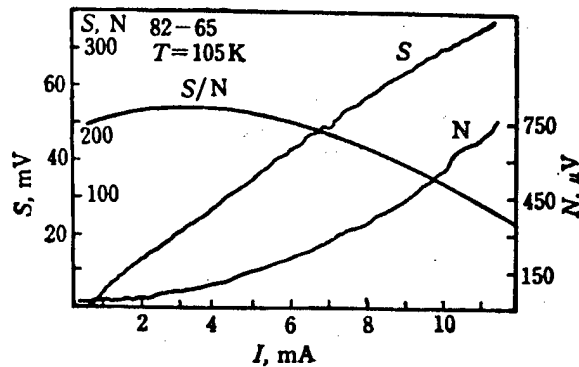


Figure 3. Signal-to-Noise Ratio Vs. Bias Current

From the equation above, the noise at 77 K is less than that at 105 K. Figure 4 shows the noise spectrum of the device. As we can see from the figure, the experimental data is very close to theoretical values. In the low-frequency region, it is $1/f$ noise. Its magnitude is related to the bias current and fabrication process.

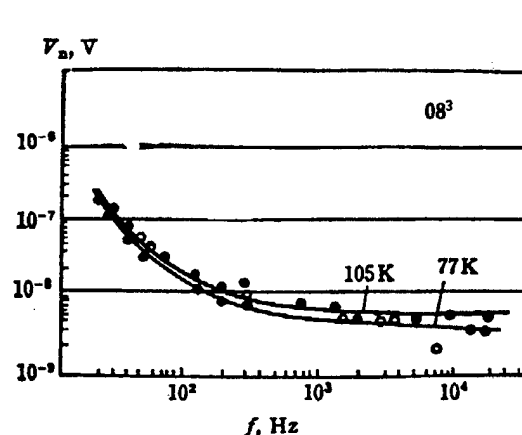


Figure 4. Frequency Spectra of Detector Noise at 77 K and 105 K

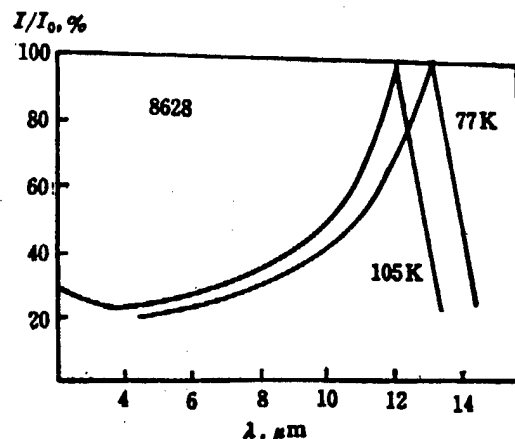


Figure 5. Relative Spectral Responsivity at 77 K and 105 K

4.4 Spectral and Temperature Characteristics

The long-wave limit of the HgCdTe detector shifts toward shorter wavelength with rising operating temperature. For example, the long-wave limit of a detector with $\chi = 0.198$ is $1.1 \mu\text{m}$ shorter by increasing the operating temperature from 77 K to 105 K. Furthermore, measured and calculated values are in excellent agreement (see Figure 5). Figures 1 and 2 show the theoretical curves of detectivity and resistivity versus temperature. In reality, temperature characteristics of a device vary a lot. Figure 6 shows measured curves of detectivity, resistivity, and noise as a function of temperature. During the development process, we measured the temperature characteristics of every device in order to ensure the device is qualified to operate at 105 K.

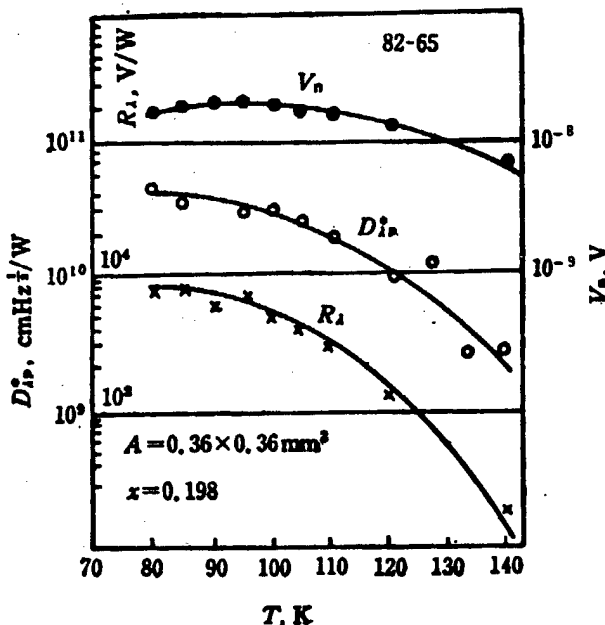


Figure 6. Detectivity, Responsivity, and Noise Vs. Temperature in the Range From 80 to 140 K

5. Reliability Test Results

Routine mechanical and temperature tests were carried out. Samples were pulled to withstand high-energy particle irradiation.

Thermal Impact Test Between 77~330 K: All materials in the detector are required to withstand a 77 K temperature. However, every material has a different thermal expansion coefficient. To this end, a fast 77~330 K recycling method was used to essentially eliminate any hidden problems associated with improper choice of materials or processes.

Vacuum Bake Test. Because Hg has a high dissociation pressure in HgCdTe, this material may undergo changes from heat. We heated the detector in an ultrahigh vacuum and measured the performance of the device at the same time. Our results showed that at approximately 1×10^{-4} Pa, the device could withstand 80°C.

Devices that passed routine tests underwent electrical aging (burn-in) and life tests in order to determine the average life of the device. We employed a fixed time cutoff and no-substitution scheme and accumulated 2.16×10^4 hours without one failure. Assuming the HgCdTe photodetector is an exponential-life type of device, based on Bayes reliability theory, its failure rate is 2.49×10^{-5} .

Based on our investigation and analysis of the performance of the HgCdTe detector at 105 K, as well as on the data gathered for routine and life tests under space conditions, the optimal parameter $D_{A\lambda}^*$ of the detector could reach

$1\sim 3 \times 10^{10} \text{cm}^{-2}\text{Hz}^{1/2}\text{W}^{-1}$ and its failure rate is less than 2.5×10^{-5} . It was found to behave very well as a part of the entire satellite operating in space with good stability and excellent reliability.

Acknowledgement

The authors wish to thank researchers Tang Dingyuan [3282 1353 0337] and Kuang Dingbo [0562 1353 3134] for their guidance in this work, Gong Huixing [7895 1920 5281] and others for their support, and those who contributed a great deal of effort.

References

1. Tang Dingyuan [3282 1353 0337], HONGWAI WULI YU JISHU [INFRARED PHYSICS AND TECHNOLOGY], Vol 4-5, 1976, p 68.
2. Xu Guosen, Ibid., Vol 2, 1980, p 4.
3. Fang Jiaxiong, Ibid., p 36.
4. Xu Guosen, Ibid., p 12.

Applications in Meteorological, Agricultural Remote Sensing

90FE0171I Shanghai HONGWAI YANJIU [CHINESE JOURNAL OF INFRARED RESEARCH] in Chinese Vol 9 No 2, Apr 90 pp 156-161 (Ms received 13 Jul 89)

[Article by Fang Zongyi [2455 1350 5030] and Jiang Jixi [3068 0679 0823] of the Satellite Meteorology Center, State Meteorological Administration, Beijing 100081, China: "Applications of FY-1 Meteorological Satellite in Meteorology and Agricultural Remote Sensing"]

[Text] Abstract

This paper presents a brief analysis of the data acquired by the FY-1 meteorological satellite in order to illustrate the usefulness of this satellite in applications such as weather system analysis, natural disaster monitoring, climate study, flood monitoring, crop estimation, etc.

Key words: Meteorological satellite, weather analysis, natural disaster monitoring.

1. Introduction

Since the United States launched the first dedicated meteorological satellite on 1 April 1960, as satellite detection technology advances and ground reception capability becomes more and more sophisticated, satellite data has been successfully used in areas such as weather forecasting, climate study, weather monitoring, and natural disaster monitoring. It has become an integral part of the worldwide weather (WWW) monitoring network. In the future, as we get more involved in world weather planning and global change study, a polar orbit space-to-earth observation system plays such an important role that it cannot possibly be replaced by other means.

On 7 September 1988, China launched its first meteorological satellite, i.e., FY-1. It provided a powerful monitoring tool to acquire data related to weather, hydrology, and the ocean. The main remote-sensing instrument on FY-1 is a very-high-resolution scanning radiometer (VHRSR). Table 1 lists the channel numbers, spectral width, spatial resolution, detection element, and primary applications of the advanced very-high-resolution radiometer (AVHRR) on the American NOAA satellite as well as those of the VHRSR.

Table 1. Comparison of Major Characteristics Between VHRSR of FY-1 and AVHRR of NOAA Meteorological Satellites

	FY-1				
	Ch 1	Ch 2	Ch 3	Ch 4	Ch 5
Spectral range (μm)	0.58 -0.68	0.725 -1.10	0.48 -0.53	0.53 -0.58	10.5 -12.5
Detector	Si	Si	Si	Si	HgCdTe
IFOV (μrad)	1.2	1.2	1.2	1.2	1.2
Subsatellite point spatial resolution (km)	1.1	1.1	1.1	1.1	1.1
Primary applications	Daytime cloud pictures, ice, and snow images	Distinguish land and water, vegetation coverage; crop estimation	Coastal water color	Coastal water color	Day and night clouds, ocean-surface temperature, cloud-top temperature

	NOAA				
	Ch 1	Ch 2	Ch 3	Ch 4	Ch 5
Spectral range (μm)	0.58 -0.68	0.725 -1.10	3.55 -3.93	10.3 -11.3	11.5 -12.5
Detector	Si	Si	HgCdTe	HgCdTe	HgCdTe
IFOV (μrad)	1.2	1.2	1.2	1.2	1.2
Subsatellite point spatial resolution (km)	1.1	1.1	1.1	1.1	1.1
Primary applications	Daytime cloud pictures, ice and snow images	Distinguish land and water, vegetation coverage; crop estimation	Nighttime clouds, ocean-surface temperature, hot-spot detection	Day and night clouds, ocean surface temperature, volcano ash cover	Soil humidity

Based on Table 1 and the actual applications of the data gathered by FY-1, all the results¹⁻³ concerning weather system analysis and forecast, and monitoring of earth resources and environment with the data collected by the AVHRR of the NOAA satellites are applicable to the FY-1 satellite.

2. Monitoring and Analysis of Weather Systems

Channels 1 and 5 of FY-1 can detect visible and infrared pictures and can be used to analyze large-scale weather systems such as fronts, cyclones, and shear lines. Especially, multi-orbit pictures of central Asia and the Indian Ocean can be used to analyze clouds over the Arabian Sea and Bay of Bengal and the weather systems over the Qing-Zang (Qinghai-Tibetan) Plateau. Time-lapse cloud pictures (APT [automatic picture transmission] data) can be used to analyze the weather system in any part of the world. This is significant to the weather forecast in China.

Figure 1 [photograph not reproduced] shows an occluded extratropical cyclone that developed over the Northeast. The cloud pattern looks like a comma. the head of the comma is located at the upper left. The cloud zone is dense and bright. Inside, there are two clear counterclockwise vortices corresponding to the occlusion front of the cyclone. On the right, there is a broken cloud band, running in quasi-north-to-south direction, connected to the head. It is the tail of the extratropical cyclone which corresponds to a cold front weakened by the cyclone. The rainfall associated with the cyclone is at the head. The tail is often accompanied with showers and gale-force winds.

Caption: Figure 1. The Visible Color Picture of the Cloud System of an Extratropical Cyclone at 06 GMT on 9 September 1988.

Figure 2 [photograph not reproduced] shows the cloud system of a cold front. A broad quasi-east-west cold front runs from the southernmost areas of the lower reaches of the Changjiang River to the northern parts of southern China. The system has several cloudless gaps. In the eastern portion, there are many short longitudinal bands, indicating weaker intensity in the cold-front cloud system. Nevertheless, the western portion of the cold front mainly consists of two clusters of dense clouds. In its warm front, there are several relatively isolated cloud clusters of very bright color. Therefore, there is moderate-to-heavy rain associated with the western part of this cold front. There might be local torrential rain before the front. In addition, over the middle and lower reaches of the Changjiang River, there are several uneven cloud lines running from west to east. They are cumulus cloud lines in the clear sky behind the front.

Caption: Figure 2. Visible Color Picture of the Cold-Front Cloud System at 08 GMT 10 September 1988.

Figure j in the color insert of this issue [see special color section], shows the cloud picture of a short wave-slot cloud system covering the northern Yellow Sea to northern Korea. The cloud thickness is quite uneven. It is relatively thick in the middle and in the southwest corner, representing main rainfall areas. In addition, there are two cumulus lines running across clear

sky over the eastern part of the central and southern Korea Peninsula from southwest to northeast. Under certain conditions, small convection entities shown as white spots on the cumulus lines may develop into larger clusters of rain cloud.

Figure 3 [photograph not reproduced] shows a time-lapse picture of the clouds over the Indian Ocean in the southern hemisphere. There are three clockwise tropical cyclones. From the direction of cloud bands and cloud lines, it is possible to analyze the direction of air flow, i.e., the direction of wind on the ocean. Furthermore, based on the smoothness of the boundary between the recombination center and a cloud band or cloud line, it is possible to roughly estimate the location of rainfall and gusts.

Caption: Figure 3. Visible Time-Lapse Color Picture Taken at 09 GMT on 26 September 1988.

From the cloud pictures sent back from FY-1, based on specific cloud patterns associated with torrential rain, thunderstorms, strong-convection clouds, and typhoons, not only their presence and location but also their development stage can be identified. Therefore, the FY-1 satellite can be used to monitor natural disasters such as torrential rains, thunderstorms, and typhoons.

Figure 4 [photograph not reproduced] shows a southwest vortex cloud system in northeast Sichuan. It is located in the middle lower part of the picture and appears as a strong convection cloud cluster. It is dense and bright and has many ups and downs, indicating its convection nature. The bulging part represents very strong convection activity. From this picture, it is possible to analyze the rainfall region and heavy rainfall area.

Caption: Figure 4. Visible Color Picture of a Southwest Vortex Taken at 08 GMT on 7 September 1988.

The cloud picture of China typhoon No 20 (Aelson) in 1988 is shown in Figure 1 in the color insert of this issue [see special color section]. The eye of the typhoon (shown as a small black quasi-circle of clear sky) is on the ocean northeast of Luzon. A thick wall of dense white clouds encircles this center, where there are heavy rains, gale-force winds, and giant waves. It is the most destructive area of the typhoon. There is a white counterclockwise spiral of convection clouds running into the wall of the typhoon cloud. This is also associated with heavy rainfall. This picture tells us the location of the typhoon center, its intensity, and the distribution of rain, winds, and waves on the ocean. Based on several cloud pictures like this one, we can forecast the movement and intensity change of the typhoon and provide a short-range weather forecast in the area for shipping and fishing authorities.

3. Climate Study and Monitoring

The long-wavelength radiation emitted by the atmosphere, ocean-surface temperature, ice coverage, geomorphology, and cloud distribution in the atmosphere are closely related to the complex energy-exchange scheme among the earth, ocean, and atmosphere. Atmospheric movement is one form of this energy

exchange and is also a result of this exchange. A meteorological satellite offers the only tool to measure these parameters on a global basis for studying and monitoring climate changes.

The raw data collected and processed by FY-1 already includes the parameters mentioned above. Other than ocean-surface temperatures, the accuracy of other parameters is comparable to that produced by a foreign satellite. Of course, climate study and monitoring requires gathering global data over a long period of time. Although FY-1 can process certain data suitable for climate research, as an experimental satellite, it is still not quite effective in areas such as satellite life and capability as a commercial system.

Figure 5 [photograph not reproduced] shows an enlarged picture of the Northwest. The black spot in the lower middle part of the picture is Qinghai Lake. The white clouds are convection clouds developed in the morning on the high plains. The green and light-green part is vegetation on the plateau. The upper left shows Qilian Mountain and its valley and the Badain Jaran desert. The sand dunes in the desert are clearly visible. This type of geomorphologic characteristics and cloud parameters is very useful in the study of regional, and even large scale, climate.

Caption: Figure 5. Composite Picture of Sand Dunes From Channels 1 and 2 at 08 GMT on 10 September 1988.

4. Flood Monitoring, Crop Estimation, and Coastal Silt Monitoring

Figure 6 shows the variation of reflectivity with wavelength for different surfaces. In the visible band ($0.5\text{--}0.7 \mu\text{m}$), the reflectivity of lakes and wet ground covered with vegetation is very weak. The reflectivity of lakes is slightly higher than that of the latter. However, the reflectivity of the latter in the near infrared ($0.7\text{--}1.0 \mu\text{m}$) increases quite a lot. The reflectivity of lake surface, however, drops significantly. Therefore, their difference is considerable. From Table 1 we can also see that due to the difference in reflectivity between land and water pictures obtained from channel 2 ($0.725\text{--}1.10 \mu\text{m}$), FY-1 can clearly show the boundary of bodies of water very well. This can be used to monitor the changes of lake size and river width in order to precisely determine flooding areas in a timely manner. It may be an important piece of information in flood prevention.

Figure 7 [photograph not reproduced] shows a picture of the Nen Jiang [River] and Songhua Jiang [River] in Northeast China during flood season. The right half is white cloud cells and clusters. The black branches in the left half and the middle are the Nen Jiang and Songhua Jiang and their tributaries. The blue piece is wetland connected to the tributaries. The width of the river can be measured from the picture. Compared to the width measured before the flood, one can quickly estimate the extent of the flood.

Caption: Figure 7. Composite Picture of the Nen Jiang and Songhua Jiang From Channels 1 and 2 for Flood Monitoring; Taken at 06 GMT on 9 September 1988.

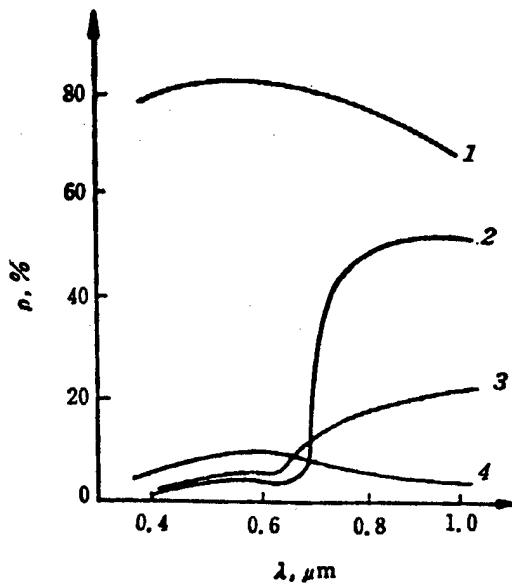


Figure 6. Variation of Reflectivity With Wavelength for Different Surfaces

Channels 1 and 2 of FY-1 are visible and infrared channels, respectively. The difference in their reflective radiance ($\text{CH}_2 - \text{CH}_1$) is the so-called vegetation coverage index which represents the growth of vegetation. Crop yield is a function of vegetation coverage in the early stage. If a statistical relation between early-stage vegetation coverage index and crop yield can be established, it is possible to use the index measured by FY-1 to predict crop yield in the future.

In terms of spectral response region, sensitivity and spatial resolution, channels 1 and 2 of FY-1 are comparable to those of the NOAA satellite. Based on vegetation coverage indices derived and pictures gathered by FY-1, its capability is identical to that of NOAA.

Figure 8 [photograph not reproduced] shows a composite picture from FY-1 satellite pictures from channels 1 and 2. The light green part represents vegetation coverage in Eastern China. A different tint reflects a different vegetation coverage index, i.e., a different stage of growth.

Caption: Figure 8. CH_1 and CH_2 Composite Picture of the Vegetation Coverage in Eastern China and Silt Content Near the Mouth of the Chang Jiang River Taken at 06 GMT on 7 September 1988.

Furthermore, it reveals the geographic characteristics near the mouth of the Changjiang River very well. Different color inside the mouth of the river and along the river bank indicates different silt content. Light blue indicates a high silt content. The blue color outward indicates lesser silt. The deep blue color far outside reflects very little or no silt. The picture also shows how silt is flowing out in the ocean. This piece of information is very important to the design, construction, and maintenance of harbors.

Composite pictures from channels 1 and 2 can also reveal the distribution of chlorophyll content over the ocean surface. This picture, together with a picture of ocean temperature distribution, can be used to forecast fishing grounds to increase the catch.

Acknowledgement

The pictures used in this paper came form the 7350 computer and the MCIDAS processing terminal in the Satellite Weather Center's data processing system. We wish to express our gratitude to the people involved in preparing those pictures.

References

1. Tao Shiyan [7118 6108 6056], et al., DAQI KEXUE [ATMOSPHERIC SCIENCE], Vol 3 No3, 1979, pp 239-246.
2. Xiao Ganguang [5135 0051 1639], et al., HUANJING YAOGAN [REMOTE SENSING OF ENVIRONMENT], Vol 1 No 4, 1986, pp 260-269.
3. Fang Zongyi, et al., "Some Uses of Meteorological Data," Proceedings of Development and Applications of Remote Sensing for Planning, Management, 1985, pp 277-288.
4. Fan Tianxi, QIXIANG [METEOROLOGY], Vol 14 No 10, 1988, pp 6-9.
5. Lauritson, L., Nelson, G.J., and Porto, F.W., "Data Extraction and Calibration of TIROS-N/NOAA Radiometer," NOAA Technical Memorandum NESS 107, November 1979.



Fig. a

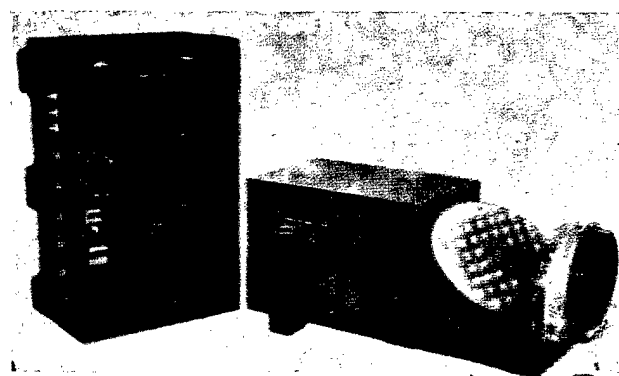


Fig. b



Fig. c

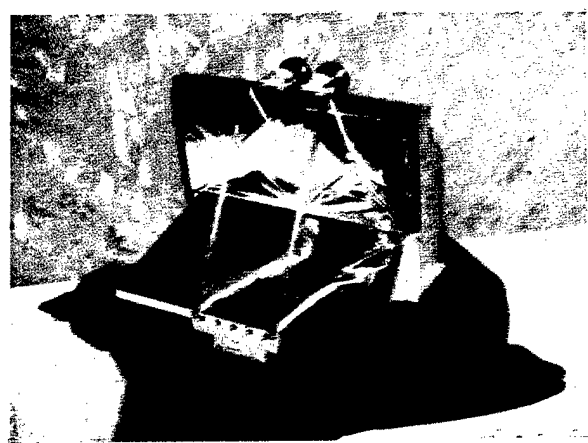


Fig. d



Fig. e

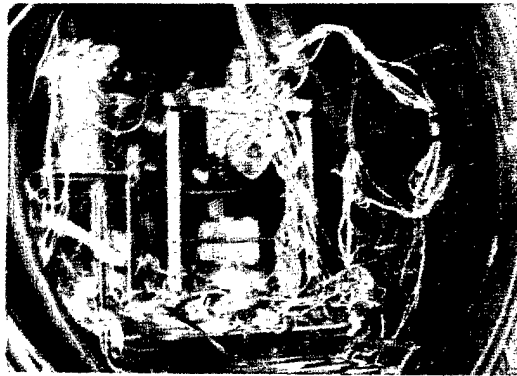


Fig. f

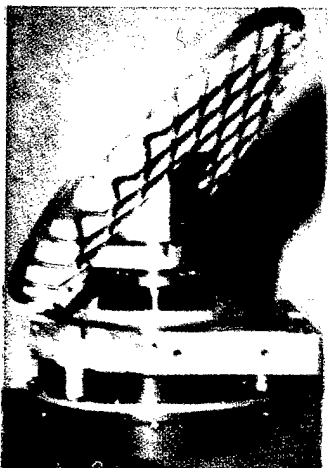


Fig. g



Fig. h

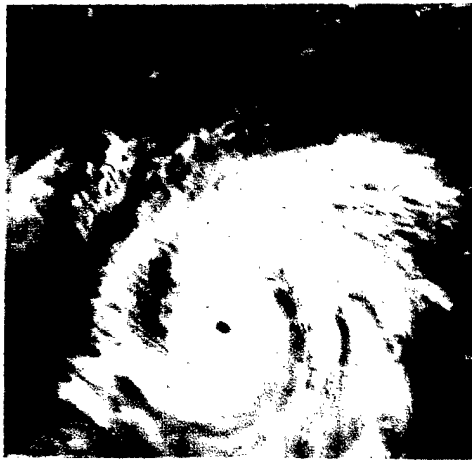


Fig. i

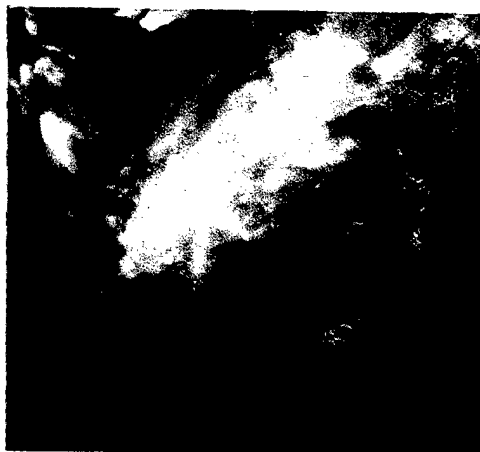


Fig. j



Fig. k

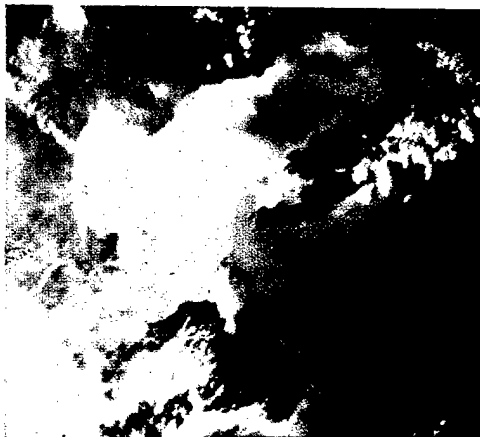


Fig. l

- END -

22161

35

NTIS
ATTN: PROCESS 103
5285 PORT ROYAL RD
SPRINGFIELD, VA

22161

This is a U.S. Government publication. Its contents in no way represent the policies, views, or attitudes of the U.S. Government. Users of this publication may cite FBIS or JPRS provided they do so in a manner clearly identifying them as the secondary source.

Foreign Broadcast Information Service (FBIS) and Joint Publications Research Service (JPRS) publications contain political, military, economic, environmental, and sociological news, commentary, and other information, as well as scientific and technical data and reports. All information has been obtained from foreign radio and television broadcasts, news agency transmissions, newspapers, books, and periodicals. Items generally are processed from the first or best available sources. It should not be inferred that they have been disseminated only in the medium, in the language, or to the area indicated. Items from foreign language sources are translated; those from English-language sources are transcribed. Except for excluding certain diacritics, FBIS renders personal and place-names in accordance with the romanization systems approved for U.S. Government publications by the U.S. Board of Geographic Names.

Headlines, editorial reports, and material enclosed in brackets [] are supplied by FBIS/JPRS. Processing indicators such as [Text] or [Excerpts] in the first line of each item indicate how the information was processed from the original. Unfamiliar names rendered phonetically are enclosed in parentheses. Words or names preceded by a question mark and enclosed in parentheses were not clear from the original source but have been supplied as appropriate to the context. Other unattributed parenthetical notes within the body of an item originate with the source. Times within items are as given by the source. Passages in boldface or italics are as published.

SUBSCRIPTION/PROCUREMENT INFORMATION

The FBIS DAILY REPORT contains current news and information and is published Monday through Friday in eight volumes: China, East Europe, Soviet Union, East Asia, Near East & South Asia, Sub-Saharan Africa, Latin America, and West Europe. Supplements to the DAILY REPORTS may also be available periodically and will be distributed to regular DAILY REPORT subscribers. JPRS publications, which include approximately 50 regional, worldwide, and topical reports, generally contain less time-sensitive information and are published periodically.

Current DAILY REPORTS and JPRS publications are listed in *Government Reports Announcements* issued semimonthly by the National Technical Information Service (NTIS), 5285 Port Royal Road, Springfield, Virginia 22161 and the *Monthly Catalog of U.S. Government Publications* issued by the Superintendent of Documents, U.S. Government Printing Office, Washington, D.C. 20402.

The public may subscribe to either hardcover or microfiche versions of the DAILY REPORTS and JPRS publications through NTIS at the above address or by calling (703) 487-4630. Subscription rates will be

provided by NTIS upon request. Subscriptions are available outside the United States from NTIS or appointed foreign dealers. New subscribers should expect a 30-day delay in receipt of the first issue.

U.S. Government offices may obtain subscriptions to the DAILY REPORTS or JPRS publications (hardcover or microfiche) at no charge through their sponsoring organizations. For additional information or assistance, call FBIS, (202) 338-6735, or write to P.O. Box 2604, Washington, D.C. 20013. Department of Defense consumers are required to submit requests through appropriate command validation channels to DIA, RTS-2C, Washington, D.C. 20301. (Telephone: (202) 373-3771, Autovon: 243-3771.)

Back issues or single copies of the DAILY REPORTS and JPRS publications are not available. Both the DAILY REPORTS and the JPRS publications are on file for public reference at the Library of Congress and at many Federal Depository Libraries. Reference copies may also be seen at many public and university libraries throughout the United States.